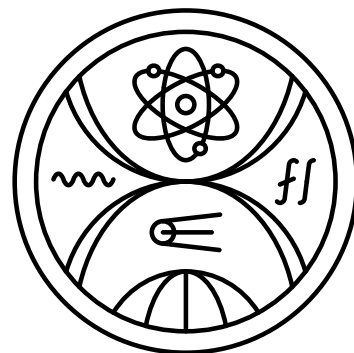


FACULTY OF MATHEMATICS, PHYSICS AND
INFORMATICS
COMENIUS UNIVERSITY, BRATISLAVA



DECAY SPECTROSCOPY OF ^{186}Bi AND
PRODUCTION OF RADON AND RADIUM
ISOTOPES

DISSERTATION THESIS

2024

Mgr. Adam Sitarčík

COMENIUS UNIVERSITY, BRATISLAVA
FACULTY OF MATHEMATICS, PHYSICS AND
INFORMATICS

DECAY SPECTROSCOPY OF ^{186}Bi AND
PRODUCTION OF RADON AND RADIUM
ISOTOPES

DISSERTATION THESIS

Study program: Nuclear and subnuclear physics

Department: Department of Nuclear Physics and Biophysics

Supervisor: doc. Mgr. Stanislav Antalic, PhD.

Consultant: Mgr. Boris Andel, PhD.

Bratislava, 2024

Mgr. Adam Sitarčík

Declaration of authorship

I hereby declare, that I personally carried out this dissertation project with help of my supervisor, consultant and with use of the listed literature and sources.

..... Bratislava, 2024

Adam Sitarčík

Acknowledgments

I would like to thank my supervisor, doc. Mgr. Stanislav Antalic, PhD. for his priceless advice, comments, support and a lot of patience. Also, I would like to thank my colleagues for many interesting discussions, help and great working environment.

Abstract:

Key words: alpha decay, decay spectroscopy, fusion-evaporation reactions, cross section

Abstrakt:

Kľúčové slová: alfa premena, rozpadová spektroskopia, fúzno-výparné reakcie, účinný prierez, štatistický kód

List of Abbreviations and Symbols

Z Atomic number (number of protons)

CE Conversion electron

CERN Conseil européen pour la recherche nucléaire - European organization for nuclear research

CN Compound nucleus

ER Evaporation residue

FER Fusion-evaporation reaction

FF Fission fragment

FWHM Full width at half maximum

g.s. Ground state

GSI Gesellschaft für Schwerionenforschung - Center for heavy ion research

HF Hindrance factor

IC Internal conversion

ICC Internal conversion coefficient

PSSD Position-sensitive silicon detector

QF Quasi-fission

SCC Scale Coulomb counter

SHIP Separator for heavy ion reaction products

TAC Time-to-amplitude converter

TOF Time of flight

UNILAC Universal linear accelerator

Contents

Introduction	1
1 Objectives of the dissertation thesis	5
1.1 Production of isotopes from radon region	5
1.1.1 Previous studies of the cross section systematics in the lead region	6
1.2 Decay spectroscopy of ^{186}Bi	7
1.2.1 Previous studies of ^{186}Bi	7
2 Physical background	9
2.1 Fusion-evaporation reactions	9
2.1.1 Quasi fission	13
2.1.2 Cross section of the fusion-evaporation reaction	13
2.2 Other types of reactions	18
2.3 Nuclear decays	18
2.3.1 Alpha decay	19
2.3.2 Internal transitions	22
2.4 Nuclear isomerism	28
3 Experimental Background	33
3.1 Experimental production of nuclei	33
3.2 Nuclei separation - SHIP	34
3.3 Detector system	36
3.3.1 Calibrations	40
3.4 Methods for nuclear structure studies	40
3.4.1 Decay spectroscopy	40
3.4.2 Other methods	40
3.5 Data analysis	40

3.5.1	Electronics and signal processing	40
3.5.2	Time-position correlation technique	42
3.5.3	Statistical analysis in case of poor statistics	44
4	Results and discussion	49
4.1	Production of isotopes from radon region	50
4.1.1	Reactions leading to radon compound nuclei	50
4.1.2	Reactions leading to astatine compound nuclei	57
4.1.3	Barrier-scaling systematics	59
4.2	Decay spectroscopy of ^{186}Bi	61
4.2.1	Experimental details	61
4.2.2	Results and discussion	64
5	Summary	73
Appendices		75
A	Excitation functions for radon compound nuclei	77
B	Excitation functions for astatine compound nuclei	85
5.1	TO DO	106
5.2	Decay spectroscopy of ^{186}Bi	107
5.2.1	Experimental details	107
5.2.2	Results and discussion	107

Introduction

Even after more than 100 years since the discovery of the atomic nucleus by E. Rutherford in 1911 [Rut11], the nuclear structure still draws many questions and presents itself in various, often unexpected ways. The vicinity of the closed proton nuclear shell at $Z=82$ is especially rich in these manifestations of the nuclear structure, for example, nuclear isomerism (first observed by Otto Hahn in ^{234}Pa [Hah21]), double and triple shape coexistence, first observed in ^{16}O [Mor56] and in ^{186}Pb [And00], respectively, or the exotic decay modes such as β -delayed fission [Kuz67a; Kuz67b].

For the production of exotic nuclei, two methods are widely used. The isotope separation online (ISOL) method uses the bombardment of a thick target by high-energy particles, resulting in spallation, fission, or fragmentation of the target nuclei. One of the most successful facilities employing this method is ISOLDE [Kug00] in CERN, Geneva. The second method of fusion-evaporation reactions uses the bombardment of thin a target with low-energy projectiles. Reaction products leaving the target are separated by gas-filled or vacuum-mode separators, such as the velocity filter SHIP [Mün79], in GSI, Darmstadt.

The first part of the dissertation thesis is the investigation of the ^{186}Bi isotope and its α -decay daughter product ^{182}Tl with the use of $\alpha - \gamma$ decay spectroscopy. The studies of thallium and bismuth isotopes in the neutron-deficient side of the nuclide table revealed a multitude of phenomena linked to the near vicinity of the proton closed shell $Z = 82$. A systematic appearance of low-lying intruder states is ranked among the most interesting ones [Hey83; Hey87; Hey88; Woo92]. The $1/2^+$ ground state in the odd-mass thallium nuclei is caused by the valence $3s_{1/2}^{-1}$ proton $\pi(0\text{p-1h})$ configuration, while the the low-lying intruder $9/2^-$ state with $\pi(1\text{p-2h})$ configuration is caused by the excitation of a proton across the $Z = 82$ gap to the $1h_{9/2}$ orbital. The situation in the even-mass thallium and bismuth nuclei is much more complex, due to the additional coupling of an unpaired neutron resulting in

the multiplets of states. The multiplets can be both normal or intruder and can become isomeric states as well. A relatively small energy difference between the multiplets and/or the collective bands built on top of them can further complicate the studies.

Previous analysis of the $^{95}\text{Mo}(^{93}\text{Nb}, 2n)^{186}\text{Bi}$ [And03a] and $^{97}\text{Mo}(^{92}\text{Mo}, p2n)^{186}\text{Bi}$ [Bat97] reactions revealed two isomeric states in ^{182}Tl populated after an α decay of ^{186}Bi with very similar half-lives. Only three γ transitions were identified in the former study and assigned to these isomers based on the energy balance of the observed transitions. Several other γ transitions remained unresolved and were not assigned to either of the isomers.

Data from the reaction $^{46}\text{Ti}(^{144}\text{Sm}, p3n)^{186}\text{Bi}$ measured at the velocity filter SHIP, Darmstadt, are available. A merger of the datasets from this and the aforementioned $^{95}\text{Mo}(^{93}\text{Nb}, 2n)^{186}\text{Bi}$ reactions increased the statistics of the collected data from the decay of ^{186}Bi about three times. The increased statistics allow us to extend the decay scheme and assign almost the entire spectrum of the γ transitions following the α decay of ^{186}Bi with the use of prompt α - γ coincidences.

The effects of unpaired nucleons can be seen in the spectra of ^{186}Bi α -decay energies populating certain levels in ^{182}Tl . De-excitation transitions can be heavily converted and the α -decay energies may be summed up with the energies of the conversion electrons. The α -decay energy distributions corresponding to such γ transitions may be difficult to disentangle and interpret. The analysis of such distributions and an alternative interpretation of the excited states within ^{182}Tl will be described and employed.

The second aim of the project is the investigation of the cross section systematics in the fusion-evaporation reactions leading to neutron-deficient compound nuclei from the radon region. Investigation of rare and exotic demonstrations of the nuclear structure requires large amounts of collected data, often in millions of registered decays. However, the production of the neutron-deficient nuclei far away from the line of β -stability reaches its limits, thus reliable theoretical models predicting the yields of the measured reactions are crucial.

Nowadays, one of the most widely used models to estimate the cross sections of the fusion-evaporation reactions is the statistical code HIVAP [Rei81; Rei92]. As has been shown in recent years, one of the parameters entering the calculation, the fission barrier, is heavily reduced in the reactions leading to the neutron-deficient compound nuclei in the vicinity of the closed proton shell $Z = 82$ [And05]. The

0. INTRODUCTION

decrease of the barrier by around 30% causes the cross section to drop by several orders of magnitude. The dependence of the fission barrier scaling factor and mass of the compound nucleus is known from the bismuth and polonium neutron-deficient isotopes.

A smaller but still very significant decrease of the fission barrier is expected in radon and radium compound nuclei (around 27% for $^{199}\text{Rn}^*$, according to the mentioned systematics). However, up to this day, no analysis focused on the evaluation of the cross sections in this region has been performed. Currently, data from the reactions leading to the neutron-deficient radon and radium isotopes are available. The reactions were measured at several projectile energies, which allows the establishment of the corresponding excitation functions. Through the variation of the parameters entering the theoretical calculation, the predictions will be varied to fit the experimental results and the optimal set of the parameters will be extracted. One of these parameters, the aforementioned fission barrier scaling factor, will help to extend the systematics known from the polonium and bismuth isotopes.

The first chapter is dedicated to the theory behind the fusion-evaporation reactions and decays analyzed in the project - alpha decay, gamma decay, and internal conversion. The details about the experimental setup - velocity filter SHIP and the detector system - are listed in the second chapter. The electronics and signal processing are presented therein, together with the description of the time-position correlation technique and the statistical analysis in case of poor statistics. The third chapter lists the goals and summary of previous studies concerning the main aims of the project. In the fourth chapter, preliminary results from the $\alpha - \gamma$ analysis of the decay data of ^{186}Bi are presented. The sixth chapter contains a summary of the results and outlook.

Chapter 1

Objectives of the dissertation thesis

In this chapter main aims of the dissertation thesis will be presented. The thesis is divided into two parts:

- Study of production systematics in the reactions leading to compound nuclei from the neutron-deficient region around $Z=86$
- Decay spectroscopy of ^{186}Bi and its α -decay product ^{182}Tl

For each part, the previous studies on the topic are summarized.

1.1 Production of isotopes from radon region

Data from the $^{52}\text{Cr} + ^{147,149,150}\text{Sm} \rightarrow ^{199,201,202}\text{Rn}^*$ and $^{56}\text{Fe} + ^{147,149,154}\text{Sm} \rightarrow ^{203,205,210}\text{Ra}^*$ reactions measured at the SHIP are available.

I'll add also astatine CNs

The main aim is to obtain experimental cross sections of the reaction products for different reactions and compare them with the theoretical calculations according to the statistical code HIVAP (section 2.1.2). By optimizing the theoretical predictions to reproduce the experimental values, an optimal fission barrier scaling parameter will be extracted.

More specifically, the completion of the following goals is expected:

- Calibration of the detector setup for each reaction: calibration of PSSD with use of known α peaks; calibration of the γ detector with a use of ^{152}Eu ; determination of the efficiency curve of the γ detector.

- Identification of the produced isotopes based on known α energies and half-lives. The isotopes with similar α decay energies will be differentiated based on the α - γ coincidence analysis. Alternatively, the use of the correlation technique can be employed, however, relatively long half-lives of the expected reaction products could be a limiting factor.
- Evaluation of the experimental cross sections and of the corresponding statistical uncertainties.
- Theoretical calculations of the excitation functions via the code HIVAP - the variation of the fission barrier scaling parameter will allow to fit the experimental values. The decrease of the parameter in the compound nucleus ^{202}Rn by around 27% is expected (according to the systematics from [And05]). Additionally, the theoretical cross sections can be evaluated by alternative approaches and models, such as Nuclear Reaction Video (NRV) calculation [Kar17] or the evaluation by the software LISE++ [Tar08], and compared with the HIVAP.
- Extraction of the optimal scaling parameter value for each analyzed reaction will allow the extension of the known systematics by astatine, radon, and radium compound nuclei.

1.1.1 Previous studies of the cross section systematics in the lead region

The production of the neutron-deficient polonium and bismuth isotopes was studied by using FERs measured at the SHIP, GSI. The cross sections of the xn and pxn evaporation channels in the reactions $^{46}\text{Ti}+^{144}\text{Sm}\rightarrow^{190}\text{Po}^*$, $^{98}\text{Mo}+^{92}\text{Mo}\rightarrow^{190}\text{Po}^*$, $^{50,52}\text{Cr}+^{142}\text{Nd}\rightarrow^{192,194}\text{Po}^*$ and $^{94,95}\text{Mo}+^{93}\text{Nb}\rightarrow^{187,188}\text{Bi}^*$ were evaluated. The experimental results together with known cross section data for the other heavier polonium and bismuth isotopes were compared with the theoretical calculations obtained from the statistical model HIVAP (section 2.1.2) [And05].

The parameters entering the theoretical calculations had fixed values corresponding to the studied reaction. The only free parameter of the calculation was the scaling factor of the liquid-drop model fission barrier. To reproduce the experimental data with the theoretical calculations, the decrease of the fission barrier by a factor of up to 35% was required. The difference between the theoretical cross sections

calculated with such a scaled barrier and unscaled one can reach up to three orders of magnitude.

1.2 Decay spectroscopy of ^{186}Bi

The main aim is to analyze the structure of ^{182}Tl , produced as an α decay product of ^{186}Bi , via $\alpha - \gamma$ coincidence analysis. Currently, data from the reactions $^{46}\text{Ti} + ^{144}\text{Sm}$ and $^{95}\text{Mo} + ^{93}\text{Nb}$ (already analyzed in [And03a]) measured at the SHIP are available, the merger of the datasets increased the total number of ^{186}Bi collected almost three times in comparison with the analysis in the reference. The statistics increase allows to assign the majority of γ signals in coincidences with α decays originating from either isomer in ^{186}Bi .

More specifically, the completion of the following goals is expected:

- Calibration of the detector setup: calibration of PSSD with a use of known α peaks; calibration of the γ detector with a use of ^{152}Eu ; determination of the efficiency curve of the γ detector.
- Identification of the produced nuclei.
- Determination of the half-lives of both ^{186}Bi isomers, to verify the previously determined value from [Bat97; And03a].
- Analysis of the $\alpha - \gamma$ coincident spectra, with an emphasis on the γ lines coincident with the α decay of ^{186}Bi . The $Q(\alpha) + E_\gamma$ value for each $\alpha - \gamma$ group will be determined, along with the corresponding half-lives extracted from the $ER - (\alpha - \gamma)$ correlation search.
- In case of the complex α distributions of $\alpha - \gamma$ groups, which will indicate $\alpha + \text{CE}$ summing effects, the tentative determination of the converted transitions - their energy and multipolarity - will be performed.
- The decay scheme of ^{186}Bi and of the states in ^{182}Tl will be constructed.

1.2.1 Previous studies of ^{186}Bi

Alpha decay activity of ^{186}Bi was first observed by J. R. H. Schneider [Sch84b]. He reported one $7191(25)$ keV α activity with a half-life of $10(4)$ ms.

Further study conducted by J. C. Batchelder [Bat97] examined ^{186}Bi produced in a $^{97}\text{Mo}(^{92}\text{Mo}, p2n)$ reaction. Two α activities correlated with α particles from the α decay of ^{182}Hg (produced by β^+/EC of ^{186}Bi α -decay daughter product, ^{182}Tl) were observed - 7158(20) keV with $T_{1/2} = 15.0(17)$ ms a 7261(20) keV with $T_{1/2} = 9.8(13)$ ms. Higher energy (shorter-lived) activity was assigned to (10^-) and lower energy (longer-lived) activity was assigned to (3^+) isomeric state in ^{186}Bi , based on the systematics from [Van91] aimed on the investigation of heavier odd-odd bismuth isotopes ($^{190-196}\text{Bi}$) and due to higher intensity of 7261 keV α line (since higher spin states are expected to be populated preferentially).

The later study [And03a] investigated ^{186}Bi produced in the $^{95}\text{Mo}(^{93}\text{Nb}, 2n)^{186}\text{Bi}$ complete fusion reaction measured at the SHIP, GSI at 419 and 438 MeV beam energies in front of the target. The collected statistics was around 50 times greater than in the previous studies, which allowed the measurement of coincident γ rays after α decay of ^{186}Bi and provided more detailed information about the nuclide. The study reported two α activities (similarly to [Bat97]), with 7261(20) keV and 7152(15) keV energies and 9.8(4) ms and 14.8(8) ms half-lives, denoted as $^{186m1}\text{Bi}$ and $^{186m2}\text{Bi}$, respectively¹. Based on the $\alpha - \gamma$ coincidence analysis and $Q(\alpha) + E_\gamma$ summing, 7080-520 and 7152-444 keV $\alpha - \gamma$ groups were assigned to the $^{186m2}\text{Bi}$ isomer and 7263-108.5 keV was assigned to the $^{186m1}\text{Bi}$. The most intense, 108.5 keV γ transition was assigned $E1$ multipolarity based on the GEANT4 Monte Carlo simulations. Other $\alpha - \gamma$ groups were not assigned due to low statistics, $\alpha - e^-$ summing effects emerging from the internal conversion and similar half-lives of both isomers. Direct, full energy crossovers of either isomer were not observed or could not be resolved.

¹This notation will be used throughout the work.

Chapter 2

Physical background

2.1 Fusion-evaporation reactions

To this date, fusion-evaporation reactions (FER), which are also referred to as reactions of complete fusion or compound nucleus reactions, continue to be the sole method for producing nuclei that are much heavier than the ones involved in the reaction. The concept of the compound nucleus model was initially presented by N. Bohr in 1936 [Boh36] and subsequently enhanced by V. F. Weisskopf and D. H. Ewing in 1940 [Wei40].

During fusion-evaporation reactions, a projectile a with a kinetic energy¹ T_p , surpasses the fusion (Coulomb) barrier to merge with a target nucleus A . Once inside the target nucleus, the projectile's energy is distributed among all nucleons through two-body interactions until equilibrium is achieved. The result of this process is the formation of a compound nucleus (CN) characterized by high excitation energy (ranging from 20 to 60 MeV) and significant angular momentum ($60 - 80 \hbar$). The compound nucleus is typically created in a time frame of around 10^{-22} s [Lov06]. If the excitation energy of the $a + A$ system significantly exceeds the fission barrier, quasi-fission (QF) can occur. Write more about QF, explain du Rietz's paper about quasi-fission, explain the equations for fissilities which were used in it and show the fig. with systematics in respect to fissilities, maybe mention the extent to which the systematics hold true.

The excessive excitation energy of the compound nucleus is radiated in the form of nucleons and/or α particles within a timespan of approximately $10^{-19} - 10^{-16}$ s. The deexcitation process of the excited compound nucleus is analogous to the evaporation

¹All kinetic energies are in the laboratory frame throughout the work, unless stated otherwise

of molecules from a hot liquid. The number of evaporated particles depends on the excitation energy, and the emission of each particle cools down the compound nucleus by roughly 10 MeV. Neutron evaporation channels (xn , where x denotes the number of evaporated neutrons) are usually predominant. In the neutron-deficient region, proton (pxn channel, involving one proton and x neutrons) and/or α (αxn channel, comprising one α particle and x neutrons) emission becomes favored due to the increase in neutron binding energies and a simultaneous decrease in proton binding energies.

The evaporation of a nucleon results in a relatively small reduction in angular momentum. If further nucleon evaporation would lead to states below the state of the nucleus with the minimal possible angular momentum for the given excitation energy (yrast line), further de-excitation occurs through discrete γ transitions. This process forms a yrast cascade, as illustrated in Fig. 2.1 and typically occurs over the interval of about $10^{-17} - 10^{-10}$ s. The final de-excited product in the ground or isomeric state is referred to as an evaporation residue (ER).

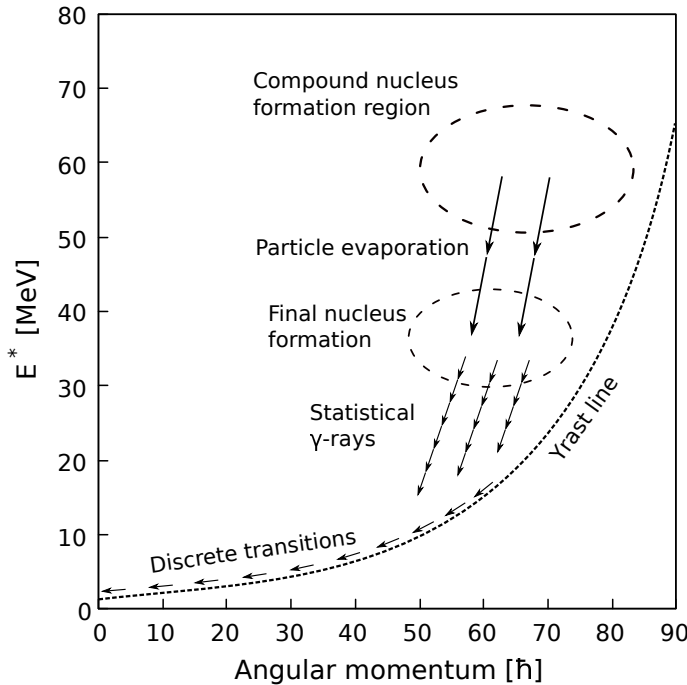


Figure 2.1: Process of particle and γ evaporation from the excited compound nucleus.

The process of the fusion-evaporation reactions can be schematically written as:



where B represents evaporation residue and evaporated particles are stated as b . Simplified notation of the reaction is $A(a, b)B$. A visual representation of the process is in Fig. 2.2.

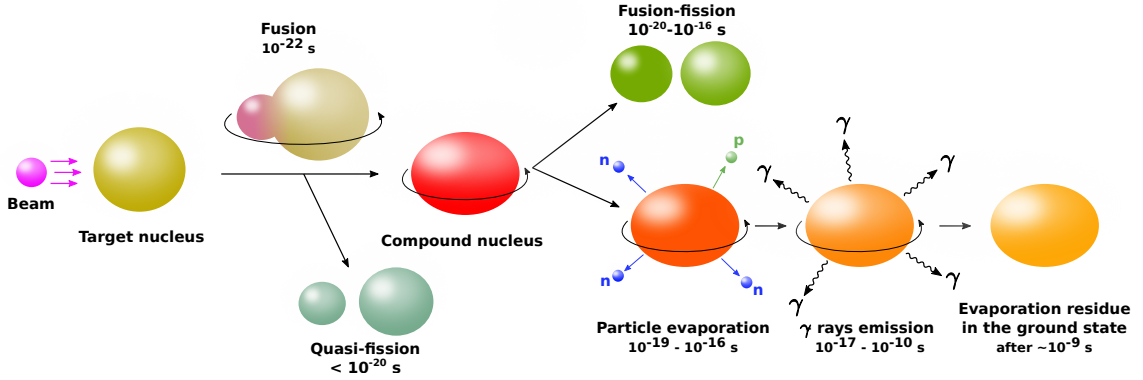


Figure 2.2: Visualisation of the process of fusion-evaporation reactions.

The energy balance of the reaction can be expressed via the masses of a projectile m_p , a target m_T , and an excited compound nucleus m_{CN}^* and kinetic energies of the projectile T_p , and the CN T_{CN} :

$$(m_p + m_T)c^2 + T_p = m_{CN}^*c^2 + T_{CN} \quad (2.1)$$

Since the momentum of the projectile $|\vec{p}_p|$ is equal to the momentum of the CN $|\vec{p}_{CN}|$ (conservation of momentum), the kinetic energy of the CN can be expressed as

$$T_{CN} = \frac{p_{CN}^2}{2m_{CN}^*} = \frac{m_p}{m_p} \frac{p_{CN}^2}{2m_{CN}^*} = \frac{m_p}{m_{CN}^*} \frac{p_p^2}{2m_p} = \frac{m_p}{m_{CN}^*} T_p \quad (2.2)$$

Combining equations 2.1 and 2.2, the expression for the mass of the excited CN is

$$m_{CN}^*c^2 = (m_p + m_T)c^2 + T_p \left(1 - \frac{m_p}{m_{CN}^*} \right) \quad (2.3)$$

An approximation $m_{CN}^* = m_p + m_T$ can be done for $m_{CN}^* \gg m_p$. Then

$$m_{CN}^*c^2 = (m_p + m_T)c^2 + T_p \left(1 - \frac{m_p}{m_p + m_T} \right) = (m_p + m_T)c^2 + T_p \left(\frac{m_T}{m_p + m_T} \right) \quad (2.4)$$

and the excitation energy of the CN is

$$E_{CN}^* = (m_{CN}^* - m_{CN})c^2 = (m_p + m_T - m_{CN})c^2 + T_p \left(\frac{m_T}{m_p + m_T} \right) \quad (2.5)$$

The term $(m_p + m_T - m_{CN})c^2$ represents the Q value of the reaction and comes from the difference of binding energies. The kinetic energy of the projectile is represented by the $T_p m_T / (m_p + m_T)$ term.

During fusion, the projectile and target nuclei have to overcome a threshold—a repulsive interaction barrier. According to R. Bass [Bas74], this barrier energy (in the center-of-mass frame) is given by

$$B_{int} = \frac{1.44 Z_p Z_T}{R_{p-T} + 2.7 \text{ fm}} - 2.9 \text{ MeV} \frac{A_p^{1/3} A_T^{1/3}}{A_p^{1/3} + A_T^{1/3}} \quad (2.6)$$

where $R_{p-t} = r_0(A_p^{1/3} + A_t^{1/3})$ with $r_0 = 1.07 \text{ fm}$. Theoretically, the B_{int} energy is the bombarding energy, for which the closest approach in a head-on collision becomes equal (or less) than $R_{p-t} + d_{int}$, where the interaction distance $d_{int} = 2.7 \text{ fm}$ is assumed equal for all fragment pairs and is adjusted to fit the experimental interaction barriers. The projectile energy in the laboratory frame is then given as

$$E_{p,int} = B_{int} \frac{A_p + A_T}{A_T} = B_{int} \frac{A_{CN}}{A_T} \quad (2.7)$$

The energy spectrum of the evaporated neutrons shown in Fig. 2.3 can be expressed as

$$N(\varepsilon) d\varepsilon = \frac{\varepsilon}{T^2} \exp\left(\frac{-\varepsilon}{T}\right) d\varepsilon \quad (2.8)$$

where the nuclear temperature T is given by

$$E^* = aT^2 - T \quad (2.9)$$

The excitation energy of the nucleus is E^* and a is the level density parameter $A/12 - A/8$ from the Fermi gas model [Lov06].

The most probable energy of the neutrons is denoted as T , while the average energy is twice that value, $2T$. Unlike the evaporation of neutrons, the evaporation of a charged particle (such as a proton or an alpha particle) requires a non-zero kinetic energy, denoted as ε_s . This kinetic energy determines the minimum energy threshold for the particle. In essence, this threshold energy is approximately equal to the Coulomb barrier. The energy spectrum of the evaporated charged particles can then be described by the equation:

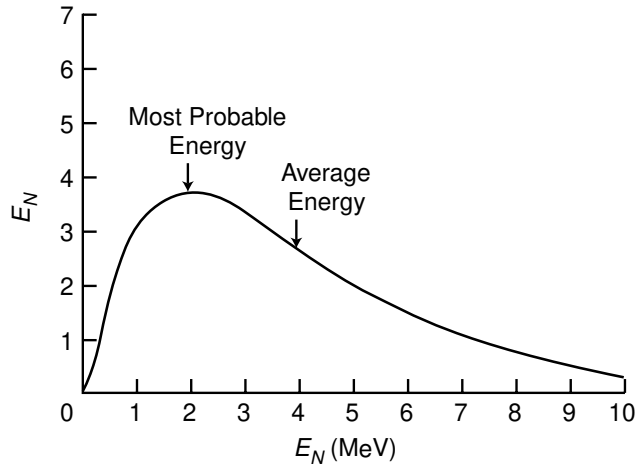


Figure 2.3: The energy spectrum of the neutrons emitted from the excited compound nucleus [Lov06].

$$N(\varepsilon) d\varepsilon = \frac{\varepsilon - \varepsilon_s}{T^2} \exp\left(\frac{-\varepsilon - \varepsilon_s}{T}\right) d\varepsilon \quad (2.10)$$

2.1.1 Quasi fission

2.1.2 Cross section of the fusion-evaporation reaction

A significant characteristic of these reactions is that the probability of producing a specific evaporation residue (cross section of the reaction) is independent of how the compound nucleus was formed. This hypothesis, also known as the Bohr independence hypothesis or the amnesia assumption, was experimentally confirmed by S. N. Ghoshal [Gho50]. In the experiment, the compound nucleus $^{64}\text{Zn}^*$ was produced in two reactions, $^{63}\text{Cu} + p$ and $^{60}\text{Ni} + \alpha$. The ratios between the cross sections $\sigma(\alpha, n) : \sigma(\alpha, 2n) : \sigma(\alpha, pn)$ for the ^{60}Ni target were found to be consistent with those of $\sigma(p, n) : \sigma(p, 2n) : \sigma(p, pn)$ for the ^{63}Cu target. The excitation functions, which illustrate the dependence of the reaction cross section on the excitation energy of the compound nucleus or the energy of the incident projectile, are depicted in Figure 2.4.

The independence of the entrance and exit channels of the FERs allows us to express the cross section of $a + A \rightarrow CN^* \rightarrow b + B$ reaction as

$$\sigma(a, b) = \sigma_{CN}(a, A) P_b(E) \quad (2.11)$$

where $\sigma_{CN}(a, A)$ represents the cross section (probability) of the creation of the

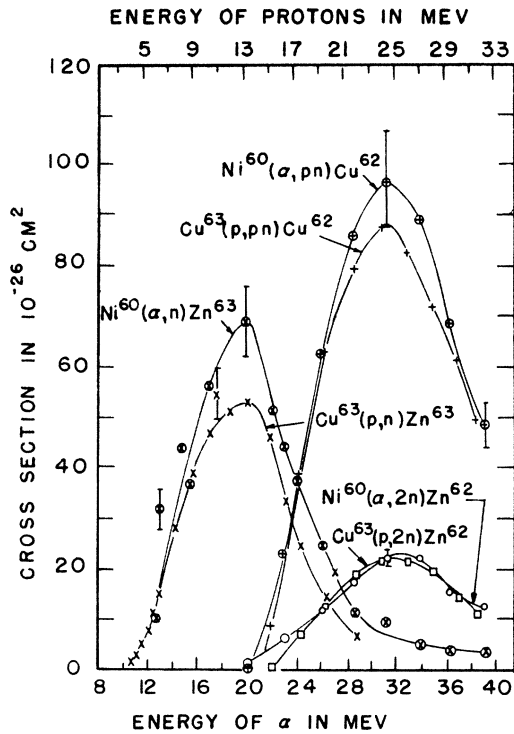


Figure 2.4: Experimental excitation functions of $^{63}\text{Cu} + p \rightarrow ^{64}\text{Zn}^*$ and $^{60}\text{Ni} + \alpha \rightarrow ^{64}\text{Zn}^*$ reactions from [Gho50]

compound nucleus and $P_b(E)$ is the probability that CN with excitation energy E decays by evaporation of particle(s) b .

Experimental cross section

The total number of ERs produced in the reaction (N_{Re}) is proportional to the cross section of the reaction (σ), the number of the projectiles (N_p), and the area density of the nuclei in the target per area unit (η):

$$N_{ER} = \sigma N_p \eta \quad (2.12)$$

where area density is expressed as

$$\eta = f \frac{N_T}{S} \quad (2.13)$$

The parameter f is the ratio of desired target nuclei to the total number of nuclei in the target (known as the isotopic purity) and N_T is the number of target nuclei with an area S . Further, $N_T = \frac{m}{M_m} N_A$ where m is the mass of the target, M_m is the molar mass of the target nuclei and N_A is the Avogadro constant.

The number of observed decays N_i originating from the ERs is lower than the total number of ERs produced in the reaction. Detector efficiency ε_i for the detected particles (see section 3.3), transmission of the SHIP separator ε (see section 3.2 and Fig. 3.3) and branching ratio of the corresponding decay must be considered as well. Relation between N_{ER} and N_i is

$$N_i = b_i \varepsilon_i \varepsilon N_{ER} \quad (2.14)$$

The total number of ERs produced in the reaction is then

$$N_{ER} = \sigma N_p f \frac{N_T}{S} = \sigma N_p f \frac{m}{S} \frac{N_A}{M_m} = \sigma N_p f d \frac{N_A}{M_m} = \frac{N_i}{b_i \varepsilon_i \varepsilon} \quad (2.15)$$

where $d = m/S$ is the width of the target in g/cm² and M_m/N_a represents an atomic mass of the target nucleus.

The total number of projectiles is derived from the charge collected by a Faraday cup Q divided by the charge state of the projectiles q and elementary charge e . The total collected charge can be expressed in terms of the total charge collection time t and an average beam current \bar{I} or a beam current during the pulse I and the duty factor D , reflecting pulse-regime of the accelerator (as a ratio between a pulse time and a total macropulse duration):

$$N_p = \frac{Q}{qe} = \frac{\bar{I}t}{qe} = \frac{IDt}{qe} \quad (2.16)$$

In the experiments performed at the SHIP, the beam intensity is measured in Scale Coulomb Counter units (SCC). The value of beam current changes throughout the experiment, therefore SCC unit and the SCC counting rate R is used. Charge collection time t is then given as

$$t = \frac{SCC}{R} \quad (2.17)$$

and the total number of projectiles can be expressed as

$$N_p = SCC \frac{ID}{Rqe} \quad (2.18)$$

Finally, from the combination of equations 2.15 and 2.18, the experimental cross section of the reaction is

$$\sigma = \frac{1}{fd} \frac{M_m}{N_A} \frac{N_i}{b_i \varepsilon_i \varepsilon} \frac{R}{SCC} \frac{qe}{ID} \quad (2.19)$$

Statistical code Hivap

Firstly introduced by W. Reisdorf [Rei81; Rei92] as a modification of the GROGI code [Gro67]—fission channel was incorporated into the de-excitation phase of the FER. The fusion cross section is calculated via the summation of the partial waves as follows

$$\sigma_{fus}(E) = \pi \lambda^2 \sum_{l=0}^{L_{crit}} (2l+1) T_l(E) \quad (2.20)$$

where λ is the reduced wavelength of the entrance channel and $T_l(E)$ are the transmission coefficients of the penetrating waves. The critical value L_{crit} of the angular momentum quantum number l emerges from the rapid decrease of the survival probability of the CN with increasing angular momentum. The typical values are $L_{crit} \sim 20$ for mercury ($Z = 80$) and up to $L_{crit} \sim 30$ for radium isotopes ($Z = 88$) [Qui93].

In the presented study, two different models are utilized to determine the values of $T_l(E)$. The first model, referred to as the inverted-parabola approach, approximates the Coulomb plus nuclear force near its maximum using a parabola with a curvature of $\hbar\omega_l$ and a height of B_l [Vaz81]. The transmission coefficients can then be obtained from the Hill-Wheeler formula [Hil53]:

$$T_l(E) = \frac{1}{1 + \exp[(2\pi/\hbar\omega)(B_l - E)]} \quad (2.21)$$

The IP approach has been found to be effective above the semi-empirical Bass barrier [Bas77; Bas80], calculated by Eq. 2.6, while fusion below the barrier is significantly suppressed. To account for the sub-barrier fusion, an alternative approach known as barrier-fluctuations is employed. In this approach, the fusion barrier is considered to fluctuate with a Gaussian distribution characterized by a height of B_0 and a standard deviation of $\sigma(B_0)$. The values of the barrier fluctuation are discussed in [Qui93] (see Fig. 12 and the accompanying description), where values of 2.5 and up to 3.5 are used for spherical and deformed compound nuclei, respectively. Both the barrier-fluctuations and inverted-parabola approaches have been shown to accurately reproduce cross section values above the fusion barrier as well [And05].

The de-excitation part of the calculation employs the evaporation theory and considers the competition between fission, γ ray, α -particle, and nucleon emission. The ratio of nuclear level densities (a_f/a_n) is calculated as described in [Rei92]. The damping constant is used to represent the fading of the shell effects on the level

Table 2.1: Values of HIVAP parameters used throughout this work, majority according to [Rei90]. Parameters used with values equal to zero are not listed.

Parameter	Description	Value
LEVELPAR	Scale parameter for the level density	1.16
a_f/a_n	Level density ratio	1
BARFAC	Fission barrier scaling	variable
EDAMP	Shell effect damping constant [MeV]	18.5
V0	Strength parameter of nuclear potential [MeV]	59
R0	Radius parameter [fm]	eq. 15 in [Rei85]
D	Diffuseness parameter [fm]	0.75
Q2	Quadrupole moment of target nucleus [fm ²]	β_2 from [Möll16]
CRED	Barrier thickness parameter	1
SIGR0	Barrier fluctuation $\sigma(B_0)$ [% of R0]	~ 2.5 for spherical nuclei $\lesssim 3.5$ for deformed nuclei

density [Ign75]. Another crucial parameter, the fission barrier, is calculated using the following equation:

$$B_f = BF \times B_f^{RLD} - \Delta W_{gs} \quad (2.22)$$

where BF is a free scaling parameter and B_f^{RLD} is the fission barrier according to the rotating liquid drop model [Coh74]. The ground state correction $\Delta W_{gs} = M_{exp} - M_{LD}$ represents the difference between the experimental and theoretical masses from the liquid-drop model. The values of the HIVAP parameters used in the calculations are summarized in Table 2.1. ADD FEW SENTENCES ABOUT THE 'FREEDOM' OF BF PARAMETER - HOW IT IS ESSENTIALLY THE ONLY FREE PARAMETER, HOW IT INFLUENCES THE RESULTS (OTHER PARAMETERS SUCH AS SIGR0 AFFECT ONLY THE SUBBARRIER PART, AND EVEN THEN, NOT DRAMATICALLY ETC.), WHY WE THINK IT IS 'PHYSICALLY' VALID THING TO SCALE THE BARRIER (RESULTS FROM OTHER METHODS WHICH SUGGEST THE SAME REDUCTION - VESEL-SKY'S 210RN, MAYBE FIND SOMETHING ELSE), HOW IT CAN POINT TO QUASI-FISSION, ALBEIT INDIRECTLY.

2.2 Other types of reactions

transfer, spallation,

2.3 Nuclear decays

The stability of atomic nuclei is characterized by an equilibrium between the number of protons and neutrons. To date, out of approximately 3300 known nuclides only 252 have never been observed to decay and are therefore considered stable. The unstable nuclei can decay either by β decay—a proton is transformed into a neutron or vice versa, or directly emitting protons, neutrons, α particles or by fission. Less common decays are, for example, double β /electron capture decays, β -delayed fission, cluster emission, and others. Studying the decay modes and their characteristic properties gives valuable information about the nuclear structure and the forces acting within the nuclei. In this section, we will provide a detailed explanation of the decays relevant to this work.

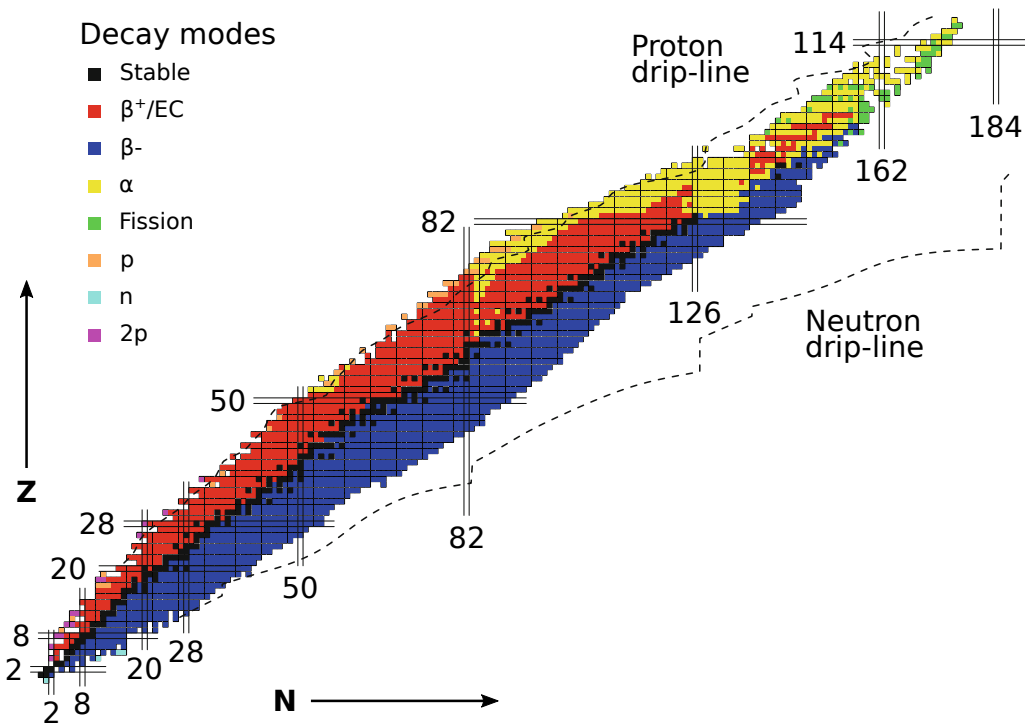
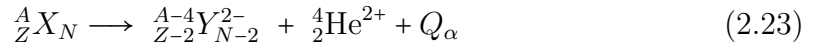


Figure 2.5: Nuclear chart showing experimentally observed nuclei. Figure adapted and modified from Ref. [Tan23].

2.3.1 Alpha decay

Alpha decay occurs when the Coulomb force, which increases with the squared atomic number of a nucleus ($\sim Z^2$), overcomes the attractive nuclear force, which increases with the mass of a nucleus ($\sim A$). Such unbalance leads to the emission of an α particle (helium nucleus), consisting of two protons and two neutrons strongly bound together. In heavy nuclei, α decay becomes energetically possible and it is the preferred mode of decay. The process of an α decay in a nucleus with mass number A , atomic number Z , and neutron number N can be represented schematically as



where Q_α represents the energetic balance of the reaction and can be expressed in terms of binding energies B as

$$Q_\alpha = [B({}_{Z-2}^{A-4}Y) + B(\alpha)] - B({}_{Z}^{A}X) \quad (2.24)$$

The Q_α value is positive (exothermic) for spontaneous α decay and typically ranges from around 4 up to 12 MeV. The energy released in a decay is transformed into the kinetic energies of the daughter nucleus (E_D , also referred to as the recoil energy) and the escaping α particle (E_α). The nuclear mass of a nucleus is $M({}_{Z}^{A}X) = Zm_p + Nm_n - B({}_{Z}^{A}X)$, therefore the Q value of an α decay can be expressed in terms of nuclear masses (or mass deficits instead) as well:

$$Q_\alpha = [m({}_{Z}^{A}X_N) - m({}_{Z-2}^{A-4}Y_{N-2}) - m(\alpha)]c^2 = E_D + E_\alpha \quad (2.25)$$

Applying the laws of energy and momentum conservation on the equation 2.25, the Q value can be calculated as

$$Q_\alpha = E_\alpha \frac{m({}_{Z-2}^{A-4}Y_{N-2}) + m(\alpha)}{m({}_{Z}^{A}X_N)} \approx E_\alpha \frac{A}{A-4} \quad (2.26)$$

and similarly, the kinetic energy of the daughter nucleus is

$$E_D = Q_\alpha - E_\alpha \approx E_\alpha \frac{A}{A-4} - E_\alpha = E_\alpha \frac{4}{A-4} \quad (2.27)$$

For a nucleus with $Z \approx 200$, an α particle carries around 98% of the released energy and only around 2% is transformed into the recoil kinetic energy of the daughter nucleus.

The initial theory of α decay proposed that an α particle is formed within the

nucleus prior to the decay [Gam28; Gur28]. This pre-formed α particle encounters a potential barrier that prevents its spontaneous emission from the nucleus. The height of this barrier can be determined using Coulomb's law, which is approximately 28 MeV for ^{238}U , while the energy of the emitted α particles is around 4.2 MeV. According to classical mechanics, the emission of such α particles would be impossible. However, quantum mechanics allows for the possibility of an α particle to tunnel through the barrier with a certain probability. The emission of an α particle is the most favorable and efficient method of energy release due to its relatively high binding energy of ~ 28.3 MeV.

Because of the α -particle tunneling through the potential barrier, the half-life of the α decay is heavily dependent on the Q_α value. H. Geiger and J. M. Nuttall found a linear dependence between the logarithm of the decay constant and the range (and thus energy) of α particles [Gei11]. Later, this dependence became known as the Geiger-Nuttall law:

$$\log T_{1/2} = a(Z) + \frac{b(Z)}{\sqrt{Q_\alpha}} \quad (2.28)$$

The variables $a(Z)$ and $b(Z)$ vary for each isotopic series. There are several available theoretical approaches for partial α decay half-life determination, such as the model presented in [Poe80] with the set of updated parameters from [Poe06] or, alternatively, an approach described in [Qi09], which can be used also for the cluster emission half-life.

Another factor influencing the half-life of the α decay is the angular momentum change between the initial (I_i) and final (I_f) nucleus. The total spin of an α particle is zero, due to the arrangement of four constituent nucleons. The angular momentum carried away by the α particle after the decay is therefore purely of orbital character. Possible angular momentum values can be $|I_i - I_f| \leq L_\alpha \leq |I_i + I_f|$. The parity change is given by the selection rule given by the parity conservation: $\pi_i = (-1)^{L_\alpha} \pi_f$. Therefore, if the parity of the initial and final state are the same, L_α must be even and if the parities are opposite, L_α must be odd.

The α transitions between the same states (regarding angular momenta and parities) are strongly preferred. The more the states differ, the more the transitions between them are retarded. The hindrance factor (HF) evaluates the extent to which the experimentally measured transition is slower compared to an unhindered, theoretical prediction:

$$\text{HF} = \frac{T_{1/2, \text{exp}}}{T_{1/2, \text{theor}}} \quad (2.29)$$

Another method to calculate the hindrance factor of an α decay is to compare reduced α decay widths of a certain transition δ^2 with unhindered (usually ground state (g.s.) \rightarrow ground state) transitions in neighbouring even-even nuclei δ_{e-e}^2 :

$$\text{HF} = \frac{\delta_{e-e}^2}{\delta^2} \quad (2.30)$$

The reduced width of an α decay represents the decay stripped of the strong dependence on the decay energy. Reduced width is directly linked to the α decay probability as

$$\lambda_\alpha = \frac{\delta^2 P}{\hbar} \quad (2.31)$$

where P is the barrier penetration factor and defines the probability of an α particle penetrating the potential barrier. The penetration probability of an α particle carrying angular momentum L after an α decay with a Q value was derived by J. O. Rasmussen [Ras59]. The natural logarithm of the factor P is twice the Wentzel-Kramers-Brillouin integral

$$\ln P = -2 \frac{\sqrt{2m}}{\hbar} \int_{R_i}^{R_o} \left[V(r) + \frac{2Ze^2}{r} + \frac{\hbar L(L+1)}{2mr^2} - Q \right]^{\frac{1}{2}} dr \quad (2.32)$$

where factor m is the reduced mass of an α particle and a daughter nucleus with atomic number Z , R_i and R_o are the inner and outer classical turning points. Simplified, R_i is the nuclear radius and R_o is the distance at which an α particle leaves the nucleus. The potential $V(r)$ is defined as

$$V(r) = -1100 \exp\left(-\frac{r - 1.17A^{1/3}}{0.574}\right) \text{MeV} \quad (2.33)$$

Based on the HF values, α transitions can be summarized as follows (according to [Lov06]):

- HF=1–4: favored transition. The populated states within mother and daughter nuclei are the same ($I_i^{\pi_i} = I_f^{\pi_f}$). Within odd A nuclei, favored transitions often lead to the excited daughter product, since the α particle is formed from a pair of nucleons from a lower-lying level.
- HF=4–10: transition between mixed or overlapping states.

- HF=10–100: transition with parallel initial and final spin projections, however, the wave function overlap is not favorable.
- HF=100–1000: transition between the states with parallel spin projections but with opposite parities.
- HF>1000: transition between the states with antiparallel spin projections and opposite parities.

2.3.2 Internal transitions

Nuclear decays and nuclear reactions often populate states energetically above the ground state in the final nucleus. These excited states are usually promptly de-excited to the ground or other excited states by internal transitions, that is either γ ray emission or internal conversion.

Emission of γ rays

The excited states of nuclei tend to promptly emit one or more photons to reach a more energetically favorable configuration. The energy range of the emitted photons can be from a few keV up to several MeV. In general, the energy balance of the emission of a photon with energy E_γ is

$$\Delta E = E_\gamma + T_N \quad (2.34)$$

where $\Delta E = E_i - E_f$ is the energy difference between the initial and the final state of the nucleus. The recoil energy of the nucleus T_N emerges from the conservation of linear momentum—the sum of the momenta of the nucleus and the emitted photon is zero ($\vec{p}_N + \vec{p}_\gamma = 0$). The recoiling nucleus (with mass M) is non-relativistic, therefore the kinetic recoil energy can be expressed as

$$T_N = \frac{p_N^2}{2M} = \frac{p_N^2 c^2}{2Mc^2} = \frac{p_\gamma^2 c^2}{2Mc^2} = \frac{E_\gamma^2}{2Mc^2} \quad (2.35)$$

For example, the recoil energy for 1 MeV photon emitted from the nucleus with $A=200$ is only ~ 3 eV, therefore in the cases of nuclear decay spectroscopy it is completely negligible since typical experimental resolutions of the detectors are in order of keV.

Discrete nuclear levels are described by their spin, parity, and excitation energy. The γ -ray emission is controlled by the conservation of energy and angular

momentum and provides a large amount of information on the structure of nuclei. The angular momentum carried away by the γ ray with a quantum number L is determined by the momentum conservation as

$$|I_i - I_f| \leq L \leq |I_i + I_f| \quad (2.36)$$

where I_i and I_f are spin and quantum numbers of the initial and final levels, respectively. The multipole order of the transition is defined by the L quantum number: dipole for $L=1$, quadrupole for $L=2$, octupole for $L=3$, etc. Additionally, the parity of the γ ray depends on the angular momentum and the electric (E) or magnetic (M) character of the transition and is given as

$$\begin{aligned} \Delta\pi(EL) &= (-1)^L \\ \Delta\pi(ML) &= (-1)^{L+1} \end{aligned} \quad (2.37)$$

Consequently, the states with the same parity can be connected either by the even- L electric or odd- L magnetic transition, while the deexcitation between opposite parity states can proceed by even- L magnetic or odd- L electric γ -ray emission. In general, EL and ML are called the multipolarity of the γ radiation and of the transition.

The lowest possible multipolarity of the transitions between $I_i=I_f$ states is a dipole transition with $L=1$. There are no monopole ($L=0$) transitions in which a single photon is emitted (classically, the monopole moment is the electric charge, which is static over time). For $I_i=I_f=0$ states the selection rules only allow a transition with $L=0$. In this case, the excited states decay through internal conversion, described in the following Sec. 2.3.2.

The rate (or the probability) of the transition heavily depends on its energy, character, and multipolarity and can be calculated using the following Wiesskopf single-particle estimates [Wei51]:

$$\begin{aligned} \lambda_E(L) &\cong \frac{4.4(L+1)}{L[(2L+1)!!]^2} \left(\frac{3}{L+3}\right)^2 \left(\frac{E_\gamma}{197 \text{ MeV}}\right)^{2L+1} R^{2L} \times 10^{21} \text{ s}^{-1} \\ \lambda_M(L) &\cong \frac{1.9(L+1)}{L[(2L+1)!!]^2} \left(\frac{3}{L+3}\right)^2 \left(\frac{E_\gamma}{197 \text{ MeV}}\right)^{2L+1} R^{2L-2} \times 10^{21} \text{ s}^{-1} \end{aligned} \quad (2.38)$$

where the nuclear radius $R = 1.25A^{\frac{1}{3}}$ is in 10^{-15} m and E_γ is in MeV. These transition rates are shown graphically in Fig. 2.6 for $A=186$. In general, the magnetic transition is slower than its electric counterpart with the same multipolarity and

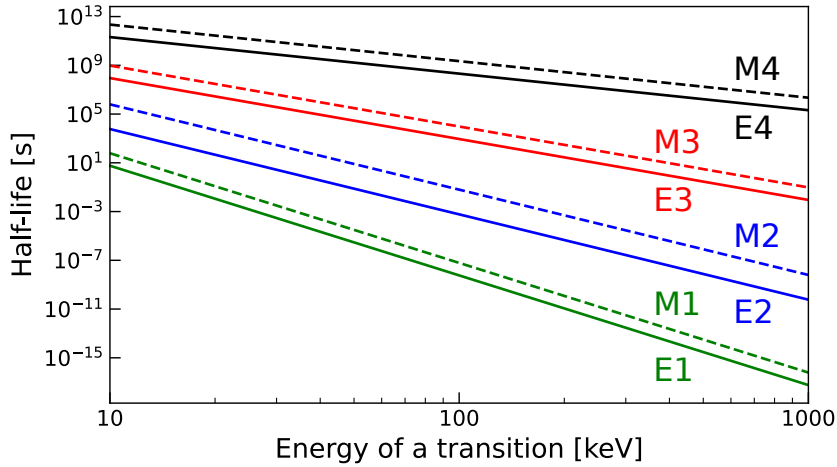


Figure 2.6: Wesskopf single-particle half-life estimates for $A=186$ calculated by Eq. 2.38 as a function of γ -ray energy.

this ratio between electric and magnetic transition decay constants is

$$\frac{\lambda_E}{\lambda_M} \approx 2.32R^2 \approx 2.9A^{\frac{2}{3}} \quad (2.39)$$

Generally, the experimental half-life of a state $T_{1/2}^\gamma$ differs from the partial half-life $T_{1/2}^W$ calculated by Eq. 2.38. For a mono-energetic decay, a correction for internal conversion is in the following form:

$$T_{1/2}^W = T_{1/2}^\gamma \times (1 + \alpha_{tot}) \quad (2.40)$$

where α_{tot} is the total conversion coefficient for all atomic shells, for more details see the next section. Similarly, other additional decay branches influence the partial half-life, increasing it correspondingly. Conventionally, the ratio between the experimentally measured and the calculated half-life represents the Weisskopf hindrance factor:

$$F_W = \frac{T_{1/2}^\gamma}{T_{1/2}^W} \quad (2.41)$$

Albeit more complex nuclear models are necessary for a quantitative understanding of the physical changes inhibiting the isomeric transitions, the Weisskopf half-life estimates are accepted as useful benchmarks for comparison with experimental values. In general, the properties of the transition probabilities via γ -ray emission can be summarized as follows:

- The probability heavily depends on the energy of the transition. An increase of the energy by one order increases the probability by three orders and vice versa.
- Transitions with lower multipolarities are dominant. The probability of 100 keV transition of $E1$ is around five orders of magnitude higher than for $E2$ transition (for nuclei with $A \approx 200$).
- For a given energy and multipolarity, the electric transition probability is around two orders of magnitude higher than that of magnetic transition. Therefore, in the $M2$ transition, a small admixture of $E1$ can be present.

Internal conversion

Along the de-excitation via the γ ray emission, an excited nucleus can undergo a process called internal conversion (IC). The interaction between the electromagnetic multipole fields of the nucleus and the atomic electron orbitals via the Coulomb force and the transferred energy can cause one of the electrons to be emitted. The energy of the emitted electron depends on the binding energy B_e needed to release the electron from the atomic orbital and the energy of the transition ΔE :

$$E_e = \Delta E - B_e \quad (2.42)$$

The binding energy of the electron in a particular shell therefore represents the threshold energy of the IC process. The conversion electrons (CE) are labeled according to the shell they were emitted from (K, L, M, \dots), corresponding to the principal atomic quantum numbers $n = 1, 2, 3, \dots$

After the emission of a conversion electron, the vacant place on the orbital is filled rapidly with an electron from the outer orbitals. The relocation of the electron from one shell to another causes the emission of X-rays which are characteristic for each element. The energy of the characteristic X-rays is given as the difference between the energies of the initial and final electron shells. Individual electron orbitals within the shell have slightly different binding energies. For example, the L shell ($n = 2$) consists of $2s_{1/2}$, $2p_{1/2}$, and $2p_{3/2}$ orbitals and the conversion electrons originating from these orbitals are referred to as L_1 , L_2 , and L_3 conversion electrons, respectively. Characteristic X-rays are therefore different for the electron relocations between $K - L_1$, $K - L_2$, and $K - L_3$ orbitals and are noted as K_{α_3} , K_{α_2} and K_{α_1}

X-rays, respectively. A summary of the notations of the characteristic X-rays is in table 2.2 together with thallium X-ray energies and intensities as an example.

Table 2.2: Notation for the characteristic X-ray transitions. Classical (Siegbahn) notation was first introduced in Ref. [Sie16]. Reference energies of X-ray transitions in thallium are from Ref. [Fir96]. The intensities are given per 100 K -shell vacancies.

Classical notation	Final – initial shell	X-ray energies in Tl [keV] (Intensity [%])
K_{α_1}	$K - L_3$	72.87 (46.2)
K_{α_2}	$K - L_2$	70.83 (27.6)
K_{α_3}	$K - L_1$	70.18 (0.0395)
K_{β_1}	$K - M_3$	82.57 (10.7)
K_{β_2}	$K - N_2N_3$	84.87 (3.9)
\vdots	\vdots	\vdots
L_{α_1}	$L_3 - M_5$	10.27 (12.4)
L_{α_2}	$L_3 - M_4$	10.17 (1.39)
\vdots	\vdots	\vdots

In the lead region, the X-ray intensities (and ratios between them) tend to not change significantly between the elements, therefore they are very similar to those of thallium from table 2.2. For 100 K -shell vacancies, K_{α_1} X-rays are the most intense with $\sim 46\%$ intensity, followed by K_{α_2} with $\sim 27\text{--}28\%$, L_{α_1} with $\sim 12\text{--}14\%$, K_{β_1} with $\sim 11\%$ etc.

The intensity of the emitted conversion electrons heavily depends on the multipolarity of the radiation. In some cases, the de-excitation of the excited states proceeds nearly exclusively via internal conversion, in others it is almost negligible compared with γ ray emission. In the transition probability calculations, both pro-

cesses have to be considered. Therefore, the total decay probability of the excited state is

$$\lambda = \lambda_\gamma + \lambda_{IC} \quad (2.43)$$

where λ_γ and λ_{IC} are the decay probabilities of γ ray emission and internal conversion, respectively. By defining the internal conversion coefficient (ICC)

$$\alpha = \frac{\lambda_{IC}}{\lambda_\gamma} \quad (2.44)$$

The total decay probability can be further expressed as

$$\lambda = \lambda_\gamma(1 + \alpha) \quad (2.45)$$

The decay probability of the IC is the sum of partial probabilities of the conversion on each shell $\lambda_{IC} = \lambda_{IC,K} + \lambda_{IC,L} + \lambda_{IC,M} + \dots$ and the total decay probability is then

$$\lambda = \lambda_\gamma + \lambda_{IC,K} + \lambda_{IC,L} + \lambda_{IC,M} + \dots = \lambda_\gamma(1 + \alpha_K + \alpha_L + \alpha_M + \dots) \quad (2.46)$$

The following equations from [Kra88] give the estimate for the conversion coefficients of electric (E) and magnetic (M) multipole transitions in a nucleus with an atomic number Z :

$$\begin{aligned} \alpha(EL) &\cong \frac{Z^3}{n^3} \left(\frac{L}{L+1} \right) \left(\frac{e^2}{4\pi\varepsilon_0\hbar c} \right)^4 \left(\frac{2m_e c^2}{E} \right)^{L+5/2} \\ \alpha(ML) &\cong \frac{Z^3}{n^3} \left(\frac{e^2}{4\pi\varepsilon_0\hbar c} \right)^4 \left(\frac{2m_e c^2}{E} \right)^{L+3/2} \end{aligned} \quad (2.47)$$

where n is the principal quantum number of the bound electron wave function and the term $e^2/(4\pi\varepsilon_0\hbar c)$ is the fine structure constant with a value of about 1/137. Theoretical values of conversion coefficients can be evaluated using a tool BRICC [Kib08].

The ICC of the transition can be determined from the number of experimentally measured γ rays N_γ and conversion electrons N_{CE} (corrected by the detection efficiency of the corresponding detector):

$$\alpha = \frac{N_{CE}}{N_\gamma} \quad (2.48)$$

The general properties of the internal conversion coefficients can be summarized as follows:

- The IC is significantly more probable in heavy nuclei than in the lighter ones due to Z^3 dependence.
- The probability of the IC decreases with the increasing energy of the transition.
- The ICCs increase rapidly with the increasing transition multipolarity.
- For a given transition, the ratio between K and L conversion electron intensities is around 8, since the conversion on higher atomic shells decreases like $1/n^3$.

2.4 Nuclear isomerism

In addition to the lowest energy state—the ground state—a nucleus may also exist in a metastable excited state known as an isomer. The term isomer was adapted from chemical isomers whose constituents are the same but with different physical configurations. Analogically, nuclear isomers consist of the same particles arranged in different orbital configurations. Although there is no consensus on the definition of "metastable", it is typically considered an experimentally measurable time, with a lower limit of about a nanosecond (10^{-9} s). The half-life of isomers may reach up to 10^{16} years, as in the case of ^{180m}Ta [Hul09], making ^{180m}Ta the only naturally-occurring isomer.

A concept of nuclides having more than one configuration was proposed by Soddy in 1917 [Sod17]. The first experimental evidence of isomers was found in ^{234}Pa , where two β -decaying states were observed [Hah21]. Despite Soddy's proposal and Hahn's discovery, the concept of isomers faced considerable resistance. Only after Carl Friedrich von Weizsäcker provided a theoretical explanation in 1936 did the idea gain wider acceptance [Wei36].

The general concept of isomers is based on the existence of a secondary minimum in nuclear potential energy with respect to a variable parameter, such as spin, shape, or the projection of spin into the symmetry axis, as is shown in Fig. 2.7. In this situation, a transition to the energetically more favorable level requires a relatively large change of the parameter, hence hindering the transition significantly.

The occurrence of isomers is far from random, as can be seen from Fig. 2.8. The isomers cluster near the proton/neutron closed shells, especially at $Z \approx 50$, $N \approx 82$

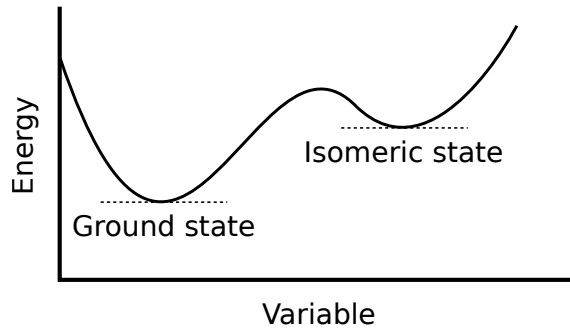


Figure 2.7: A schematic representation of an isomer as a secondary energy minimum of a function of a variable determining the type of isomer.

and $Z \approx 82$, $N \approx 126$ where spherical nuclei are typical. Besides that, well-deformed nuclei in between the closed shells give rise to K isomers.

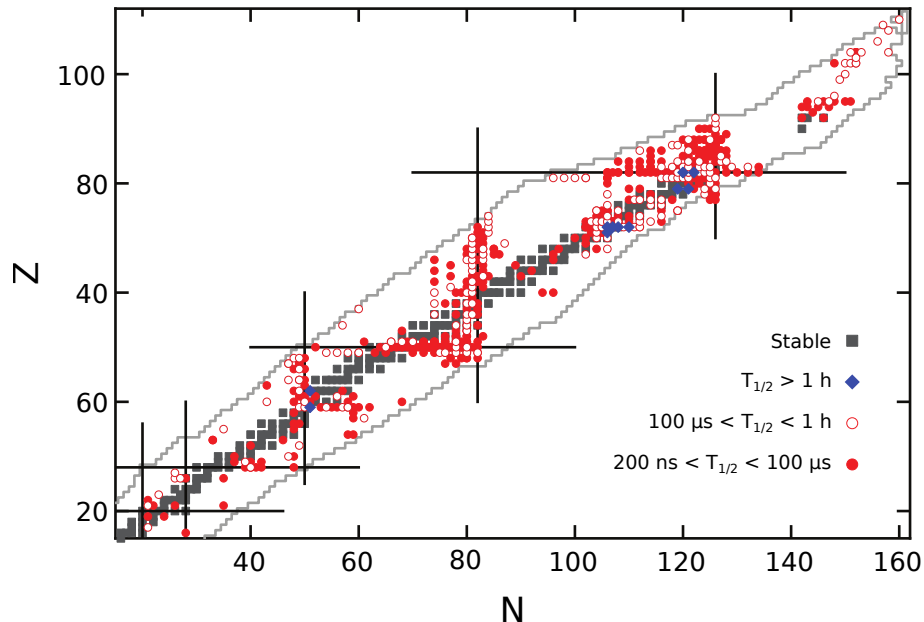


Figure 2.8: Nuclear chart showing the occurrence of isomers with excitation energies over 600 keV. Figure adapted and modified from Ref. [Dra16].

Spin isomers

Spin isomers were the first to be experimentally observed in ^{234}Pa [Hah21] and theoretically described [Wei36]. Spin isomers occur when a nucleus is trapped in an excited state with spin significantly different than lower-lying states, see 2.7. A deexcitation to these lower-lying states would require a large change of angular momentum, resulting in a high-multipolarity γ -ray emission. As was explained in

Section 2.3.2, high-multipolarity transitions are highly hindered, therefore long-lived spin isomers are created. An extreme example of spin isomers is ^{180m}Ta , where a large multipolarity of $\lambda=7, 8$ and low excitation energy results in its half-life of over 10^{16} years [Hul09].

A special type of spin isomers is seniority isomers. A quantum number seniority, ν , was introduced to explain atomic spectra [Rac43]. In nuclear physics, seniority denotes the number of nucleons that are not paired to an angular momentum of zero. Seniority is zero in the g.s. of even-even nuclei, where the lowest-energy excited states with $\nu=2$ are created by breaking a nucleon pair. A typical examples of seniority isomers are found in semi-magic nuclei, for example, in the $N=50$ isotones ^{92}Mo , ^{94}Ru , ^{96}Pd , ^{98}Cd [Wal20]. Here, the two unpaired protons occupy the $g_{9/2}$ orbital and the resulting $\nu=2$ states have spins of $I=2, 4, 6, 8$. The 8^+ states become isomeric, due to a low-energy $E2$ transition between $8^+ \rightarrow 6^+$ states.

K isomers

The existence of non-spherical nuclei led to their description in terms of deformed shapes and axis symmetry. Weizsäcker's explanation of isomerism revolved around the magnitude of angular momentum, whereas the nuclear symmetry axis implied that also the direction of angular momentum could be important. This realization led to the specification of the projection of the total angular momentum into the symmetry axis as a quantum number K and, consequently, K -forbidden transitions [Ala55]. Interestingly, the first cases of these so-called K isomers were observed prior to the theoretical description in ^{190}Os [Chu50] and ^{180}Hf [Bur51].

A transition of angular momentum λ is said to be K -forbidden, if the change ΔK of the K value is $\Delta K > \lambda$, with a degree of forbiddenness of $\Delta K - \lambda$ [Tan23]. K -forbidden transitions can be strongly hindered, even though they are not completely forbidden, due to K -mixing. An example is ^{178}Hf , where the 4-second $K=8$ isomer decays internally by an $E1$ transition with the Weisskopf hindrance of about 10^{13} [ENS24].

A typical locus of K isomers within the chart of nuclides is in-between the closed shells, at $Z \approx 75$, $N \approx 115$ ($A \approx 190$). Besides that, the region of superheavy elements at $Z \approx 100$, $N \approx 150$ ($A \approx 250$) is also known to contain K -isomers, such as $K=8$ isomers in ^{250}Fm and ^{254}No [Ghi73].

Shape isomers

The third type, known as shape isomers, is a consequence of a secondary minimum at large elongation of the nucleus. first discovered in ^{242}Am [Pol62].

The decay of an isomer can proceed by the same means as of the ground states, i.e., by the α , β decay, fission, etc. In contrast to the ground state, the isomers can also decay internally, by either the γ -ray emission or the internal conversion, thus reaching lower excited states or the ground state.

Chapter 3

Experimental Background

In this chapter, a description of the Separator for Heavy Ion reaction Products (SHIP) and detection system will be presented. Electronic systems, signal processing, and correlation techniques will be explained as well.

3.1 Experimental production of nuclei

A beam of projectiles is provided by UNIversal Linear ACcelerator (UNILAC), which can accelerate elements up to uranium ($Z = 92$) to energies up to 20 AMeV (MeV per nucleon). Accuracy of the beam energy is ± 0.01 AMeV and beam intensities can reach 3 p μ A for $^{40}\text{Ar}^{8+}$, 1.2 p μ A for $^{58}\text{Fe}^{8+}$ and 0.4 p μ A for $^{82}\text{Se}^{12+}$ (1 p μ A (particle micro Ampere) = 6.24×10^{12} particles/s) [Hof00]. UNILAC operates in a pulse mode with 50 Hz frequency - one 20 ms macro-pulse consists of ~ 5 ms irradiation period (beam-on) and ~ 15 ms pause period (beam-off).

Accelerated beam is focused onto a target to the spot with a diameter of 5–10 mm [Fol95; Lom02]. The target consists of eight banana-shaped segments, each with dimensions of 110×23 mm, arranged into a circle with a diameter of 310 mm, see Fig. 3.1. The target material is evaporated onto a carbon foil about $35 \mu\text{g}/\text{cm}^2$ thin and covered with another $10 \mu\text{g}/\text{cm}^2$ carbon layer, to decrease sputtering and increase target emissivity. The targets are $(0.1\text{--}1)$ mg/cm 2 thick, for lead and bismuth targets it is usually $\approx 500 \mu\text{g}/\text{cm}^2$. A thicker target leads to wider excitation functions (due to a larger distribution of energy losses of the projectiles in the target) which subsequently leads to the mixing of different evaporation channels and thus a higher background.

Projectiles can pass through inhomogeneities and pinholes in the target and

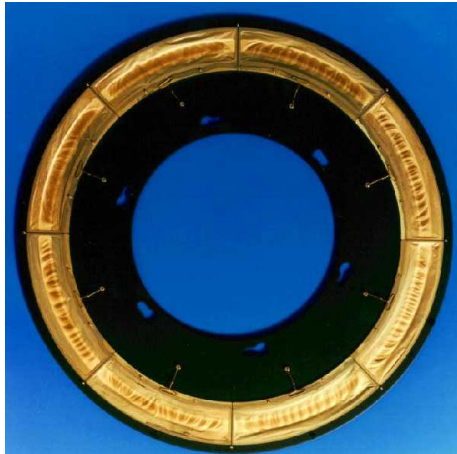


Figure 3.1: Eight-segment target wheel used at the experiments on SHIP.

increase background in the detector system. Therefore, a movable ($30 - 60 \mu\text{g}/\text{cm}^2$) carbon foil (also called charge-equilibration foil) is placed $\sim 20 \text{ cm}$ behind the target. The foil equilibrates the charge state of the reaction products and projectiles since the separator is optimized for particles with a particular charge state, while other states are suppressed.

The target wheel rotates synchronously with the beam macro-pulse structure to increase the irradiation area and thus avoid radiation damage and melting of the target [Mar79]. The rotation frequency is 18.75 Hz. Consequently, combined with the 50 Hz frequency of the beam-pulsing, the same target segment is exposed to radiation following a 160-millisecond cooling interval, equivalent to three complete rotations of the wheel. Furthermore, the low melting points of the commonly used materials, such as bismuth (271.4°C) or lead (327.5°C), can be compensated by using the compound targets with increased melting points—for example, PbS with 1130°C and BiF_3 or Bi_2O_3 with 720 and 820°C , respectively [Kin03; Kin06].

3.2 Nuclei separation - SHIP

Separator for Heavy Ion reaction Products (SHIP) located at GSI Darmstadt (Germany), is an electromagnetic separator, which uses kinematic properties of evaporation residues (ER) to separate them from other reaction products and projectiles based on their velocity [Mün79; Hof00]. Configuration of SHIP (Fig. 3.2) can be written as $3Q, E, 2M, 2M, E, 3Q, M$, where Q is a magnetic quadrupole, E is an electric deflector and M is a dipole magnet. In principle, SHIP consists of two velocity filters ($E, 2M$) facing each other. In contrast to the classical Wien filter,

SHIP has separated electric and magnetic fields, which improves its efficiency and background suppression.

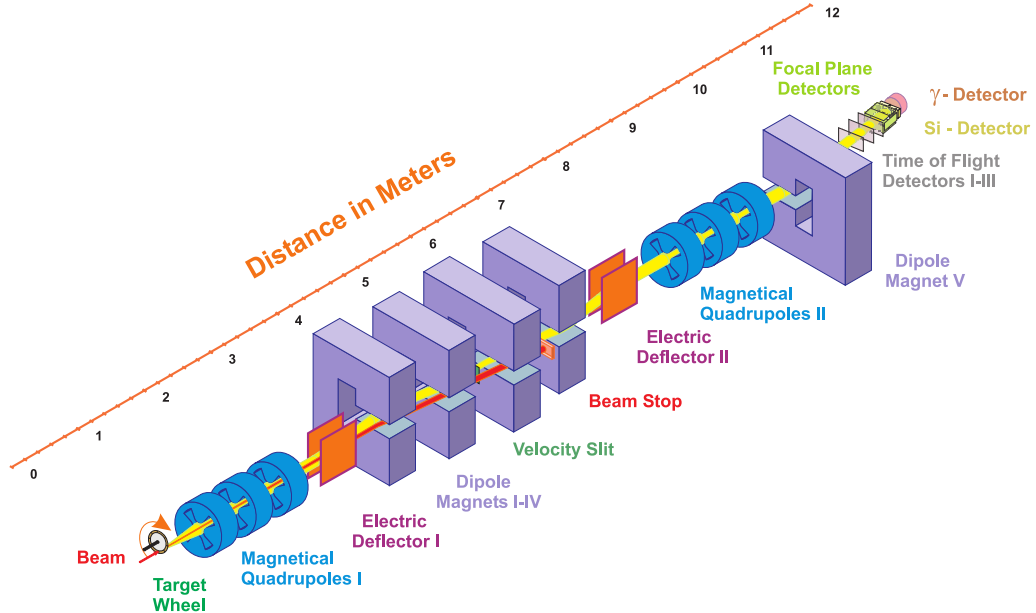


Figure 3.2: Velocity filter SHIP at GSI Darmstadt.

After the irradiation of the target, reaction products leave the target scattered at different angles. The focusation behind the target is done by the electro-magnetic lenses arranged as quadrupole triplet. Each magnet is turned by 120° , to ensure a uniform focusation. Afterwards, particles enter the ion-optical separator, where electric and magnetic fields perpendicular to each other interact on the charged particles by the Lorentz force:

$$F = qE + qvB$$

To pass the filter without deflection, Lorentz force has to be 0, therefore $qE = qvB \rightarrow E/B = v$. This allows for charged particles with a certain velocity to pass the filter independently on their charge. Since the target nuclei are at rest and therefore have zero momentum, the momentum of an ER is the same as that of a projectile. Due to higher mass, the velocity of ERs is lower than the velocity of projectiles, which allows setting a specific E/B ratio allowing only ERs to pass through the separator.

Another quadrupole triplet is placed behind the second electric deflector, to focus separated reaction products. One dipole magnet is further downstream to provide an additional 7.5° deflection to separate reaction products from high-energy

background passing through the separator.

SHIP accepts ions with a relative velocity width of $\pm 5\%$ and a charge state width of $\pm 10\%$. Flight time of the ERs through SHIP is around $2\mu\text{s}$. Total background suppression can reach the factor of 10^7 – 10^{11} . The total transmission coefficient (ratio between the number of ERs entering the filter and the number of ERs leaving the filter) of the reaction products is heavily dependent on the mass (a)symmetry of the projectile and target nuclei. More symmetric reactions (e.g. $^{136}\text{Xe}+^{136}\text{Xe}$) can reach up to 100% transmission, while very asymmetric reactions like $^{12}\text{C}+^{194}\text{Pt}$ reach only around 2%, see Fig. 3.3 and Ref. [Maz08]. After the separation, reaction products are implanted into the focal plane of the detector system.

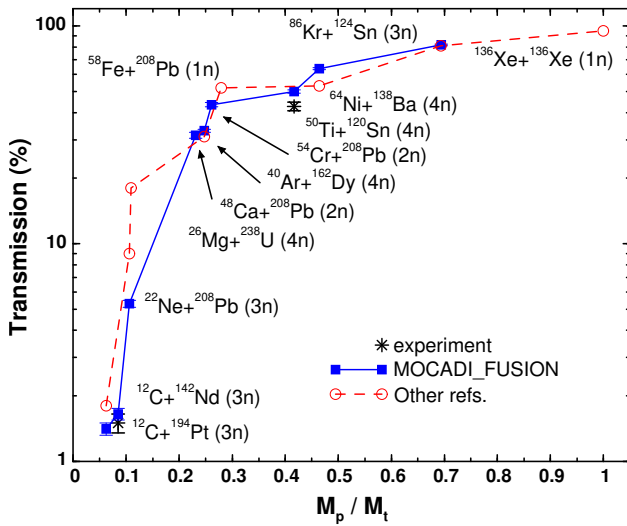


Figure 3.3: SHIP transmission - comparison of the experimental (black asterisks) and theoretical values calculated by the code MOCADI_FUSION (blue line). The red line represents values from [Pop97; Pop99]. Figure taken from [Maz08].

3.3 Detector system

After the separation, reaction products fly through the time-of-flight (TOF) system and are implanted into the detector system at the focal plane of the beam (Fig. 3.4).

The detector system consists of two or three TOF detectors, seven position-sensitive silicon strip detectors (PSSD) - one implantation PSSD (STOP) and six PSSDs in the backward direction (BOX), veto detector, and a germanium clover array.

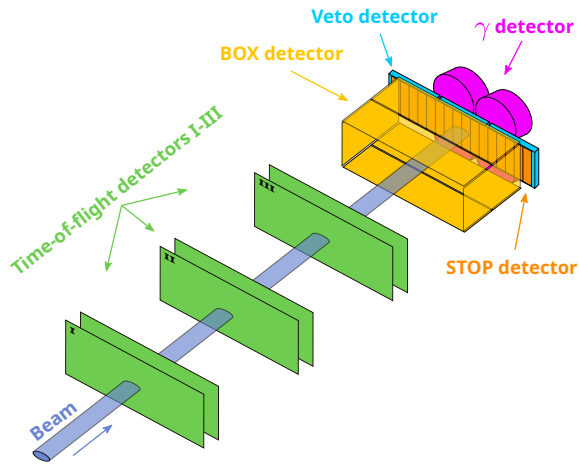


Figure 3.4: Detector setup behind SHIP (not to scale).

TOF system

Depending on the experiment, the TOF system consists of two or three TOF detectors 15 mm apart [Šár96]. Each TOF detector is made up of two self-supporting $30\text{ }\mu\text{g}/\text{cm}^2$ thick carbon foils, with 55 mm^2 active area. After a reaction product passes a foil, electrons are emitted. An electric potential of 4 kV is applied between the foils to accelerate emitted electrons, while a perpendicular magnetic field bends electrons onto microchannel plates for amplification and signal reading. The transparency of the TOF system is 100% and the time resolution is 700 ps. The efficiency is around 99.8% for two and close to 100% for three TOF detectors. Anticoincidence between the TOF system and the STOP detector allows us to distinguish between signals induced by particles/nuclei coming from the separator and the signals induced by the decays of already implanted nuclei. From the time resolution of the TOF system and energy detected in the STOP detector, rough mass determination with an accuracy of $\pm 10\%$ is achievable [Hof00].

PSSD - STOP and BOX detectors

A PSSD consists of 16 silicon strips with a total active area of $35 \times 80\text{ mm}^2$. Each strip is 35 mm long, 5 mm wide and $300\text{ }\mu\text{m}$. Vertical position resolution is $\sim 150\text{ }\mu\text{m}^1$ for an α decay. Due to the position sensitivity, one PSSD is equivalent to 3700 single detectors, each with $0.15 \times 5\text{ mm}^2$ active area. A typical energy resolution is 14 keV for ^{241}Am as an external source [Hof00]. All PSSDs are cooled down to 263 K.

¹All resolutions are noted as FWHM

In reality, a sum of an α -particle energy and the kinetic energy of the recoiling nucleus after an α decay is detected. Due to the pulse height defect affecting the detection of the recoiling nucleus, position resolution is worse - around 0.5 mm. The energy resolution is also affected by the pulse height defect, summing of the spectra from individual strips and non-ideal calibration and is around 20 keV,

One PSSD is placed in the focal plane of the beam coming from the separator. Here, ERs are implanted and stopped, hence the name STOP detector. Due to the range of α particles d_α (and fission fragments (FF)) in silicon being significantly larger than the range of ERs d_{ER} , α particles/FFs can escape the STOP detector in the backward direction without depositing full energy. This situation is displayed in Fig. 3.5.

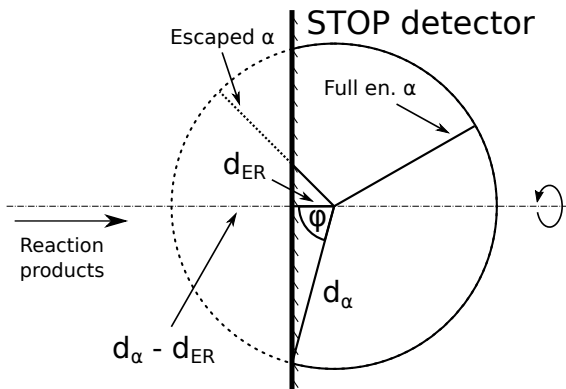


Figure 3.5: Geometric efficiency for detecting full-energy α particles after implantation into the STOP detector.

The ratio of α particles fully registered in the detector is calculated as the ratio between the areas of a sphere with the radius d_α and of a spherical cap of this sphere defined by the detector plane at a distance d_{ER} from the center of the sphere (solid curved line in Fig. 3.5). With the area of a spherical cap being $A_{cap} = 2\pi d_\alpha(d_\alpha + d_{ER})$, the geometric efficiency of the detector to fully register a particle is:

$$\varepsilon_{geom} = \frac{A_{cap}}{A_{sphere}} = \frac{2\pi d_\alpha(d_\alpha + d_{ER})}{4\pi d_\alpha^2} = \frac{1}{2} + \frac{d_{ER}}{2d_\alpha} \quad (3.1)$$

For example, in the $^{46}\text{Ti} + ^{144}\text{Sm}$ reaction at 239.2-MeV beam energy, evaporation residue ^{186}Bi is implanted into the STOP detector with an energy of ~ 20 MeV (after energy lost in the target, TOF system, mylar degraders etc.) and decays via α decay with $E_\alpha = 7.2$ MeV. The corresponding implantation depths are $d_{Re} \approx 3.6$ μm and $d_\alpha \approx 41$ μm . From Eq. 3.1, the geometric efficiency of detecting full energy α particles is around 54.4%. Energy losses and implantation depths were calculated

with LISE++ software [Tar08].

To increase the geometric efficiency of the STOP detector, another six PSSDs are placed upstream of the beam in a box-like shape (hence the name BOX or BACK detectors). Neighboring strips of BOX detectors are connected galvanically, creating 28 segments. The geometric efficiency of the BOX detectors reaches 80% of 2π half-space in front of the STOP detector and the energy resolution of the STOP+BOX system is around 70 keV. This decrease in resolution (compared to ~ 20 keV of STOP detector) is because particles/FFs have to pass through dead layers of both STOP and BOX detectors, which is around $10 \mu\text{g}/\text{cm}^2$ thick. Coincidences between STOP and BOX detectors allow us to reconstruct the full energy of the α particles/FFs.

In front of the silicon detector array, degrader foils, usually from Mylar, can be installed. The thickness of foils can be adjusted in increments of $0.5 \mu\text{m}$ up to several μm . Degrader foils are used to absorb low-energy projectiles passing through SHIP and to reduce the implantation depth of ERs (to eliminate low-energy "tails" from escaped particles). The ability to adjust implantation depth is crucial especially for the total kinetic energy determination of FFs, since the effect of the pulse-height defect varies with the implantation depth of ERs [Mos20].

Veto detector

A veto silicon detector is placed behind the STOP detector. Its purpose is to detect particles - usually high-energy protons - that pass through the STOP detector and are not registered by the TOF system. These signals are then rejected based on the coincidences between STOP-Veto detectors. Similarly to PSSDs, the Veto detector is cooled down to 263 K.

Germanium clover detector

Closely behind the array of silicon detectors, a germanium detector for the detection of X-rays and γ quanta is placed. In the past experiments, only one single germanium crystal was used, which did not allow measurement of the $\gamma - \gamma$ coincidences. Nowadays, a system of four identical germanium crystals arranged in a clover-like shape is used, hence the name clover detector. Two clovers with different volumes are usually used:

- VEGA type clover detector [Kas98]: four crystals with a diameter of 70 mm each and shaped and formed into a block with dimensions $(124 \times 124 \times 140)$ mm³.

- The SHIP clover detector [Heß10]: four crystals with a diameter of (50–55) mm each and shaped and formed into a block with dimensions (102 × 102 × 70) mm³.

VEGA clover provides better efficiency for detecting high-energy quanta, compared to the SHIP clover. The energy resolution of the germanium detectors is around (1.4-2.1) keV. Due to relatively low detection efficiency of around (10-12)% for 130 keV γ quanta, γ - γ coincident measurements require relatively high statistics.

3.3.1 Calibrations

Ballistic, energetic (PSSD and Ge), position, efficiency, problems with the shift in R206 etc.

3.4 Methods for nuclear structure studies

3.4.1 Decay spectroscopy

alpha decay spectro, gamma spectro, beta decay spectro etc, problems, advantages, challenges

3.4.2 Other methods

Laser spectroscopy

e.g. ISOL methods, ISOLDE, short mention and description, nothing long, examples of facilities

In-beam spectroscopy?

same as in laser spectro, short description, examples of facilities

3.5 Data analysis

3.5.1 Electronics and signal processing

In an experiment, signals from different sources (particles, projectiles, transfer products, ERs, FFs, γ quanta, ...) with a wide variety of energies from a few keV to hundreds of MeV are registered, and processed.

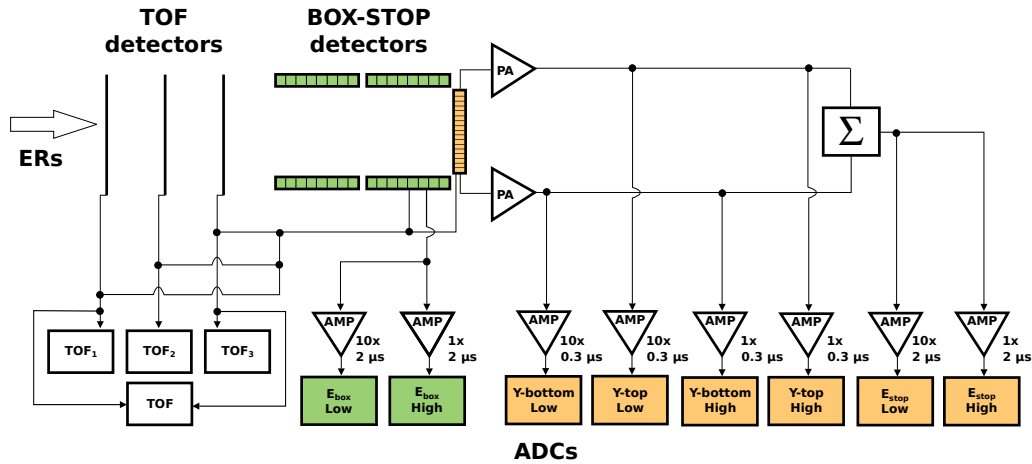


Figure 3.6: Schematic representation of the electronic system of STOP, BOX, and TOF detectors. Figure adapted from [Štr06].

The electronic system (Fig. 3.6) is divided into two branches, separate for low- and high-energy signals:

- Low-energy branch: processes signals up to ~ 16 MeV from the STOP and BOX detectors and up to ~ 1500 keV from germanium detectors with an amplification factor of 10.
- High-energy branch: processes signals from $\sim 4 - 300$ MeV from the STOP and BOX detectors and up to ~ 8 MeV from germanium detectors without an amplification.

Signals from the detector are processed with fast analog-to-digital converters with $3.5\text{-}\mu\text{s}$ conversion time and 128-word first-in-first-out buffers in each channel [Hof00]. The signal width is determined by the shaping time constants— $0.3\ \mu\text{s}$ is used for the position, and $2\ \mu\text{s}$ for the energy signals.

Time differences $\Delta t(\text{particle} - \gamma)$ between particle- γ signals are handled based on the time intervals [Ant11]:

- Time differences $\Delta t(\text{particle} - \gamma) < 5\ \mu\text{s}$ are determined by the coincidence time of the data acquisition system and are measured with time-to-amplitude converters (TAC) with a resolution of 200 ns.
- Time differences $\Delta t(\text{particle} - \gamma) > 25\ \mu\text{s}$ are measured by a continuously running clock with a resolution of $1\ \mu\text{s}$.

Time interval $\Delta t(\text{particle} - \gamma) = (5-25)\ \mu\text{s}$ is inaccessible due to the dead time of the data acquisition system.

In [Ant11], the time of the prompt coincidences was delayed by $\approx 0.8 \mu\text{s}$ and in the analysis $\text{TAC}_{\text{prompt}}=0 \mu\text{s}$ was set. Therefore, coincidences of γ quanta emitted *before* the particles were measured as well (with $\text{TAC} < 0 \mu\text{s}$). Coincidences with $\text{TAC} > 0 \mu\text{s}$ were due to γ quanta emitted *after* the particles within $\approx 2.6 \mu\text{s}$.

To determine the vertical position along the strip in the STOP detector, a signal is taken from the top and the bottom of the strip separately. The total energy is then the sum of the top and bottom signals. Position determination along the strip is done by comparing the energy signal from the top and bottom of the strip to the total energy. The BOX detector is not position-sensitive, due to the galvanic connections between the strips.

The analysis of experimental data is performed with the use of Object Oriented On-line Off-line system (Go4) [Ada08]. Go4 is based on the object-oriented analysis system ROOT [Bru97], with implemented extensions required for medium- and low-energy nuclear and atomic physics experiments.

3.5.2 Time-position correlation technique

This powerful technique was first introduced in 1979 and used in the α decay studies of the neutron deficient isotopes [Hof79]. It relies on the principle that the implantation and any subsequent α /SF decays of an ER and its daughter products have the same vertical position. The principle is shown in Fig. 3.7.

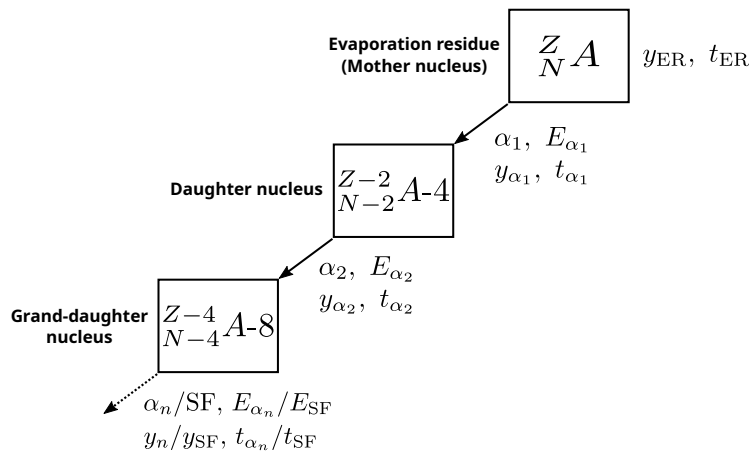


Figure 3.7: Correlation technique principle.

By adjusting correlation conditions, the technique enables us to study nuclei one by one and provides a significant background suppression, see the comparison in Fig. 3.8. Time window of around 3–5 times of the half-life of the corresponding nucleus

and position window of ~ 0.8 mm for α - α and ER- α were used throughout this work. The position window size was deduced from the correlation search of the short-lived isotopes (to reduce random correlations) and the corresponding position-difference distributions. The correlation technique enables the half-life determination of the studied nuclei and separation of the overlapping α -decay energies based on their different half-lives. New isotopes can be identified by reconstructing the decay chain from the decay of a known daughter nucleus back to the unknown mother nucleus. A special case is the correlation search of conversion electrons when the energy loss of electrons is not high enough to produce a position signal in the strip detector—therefore, in such cases, no position condition is used.

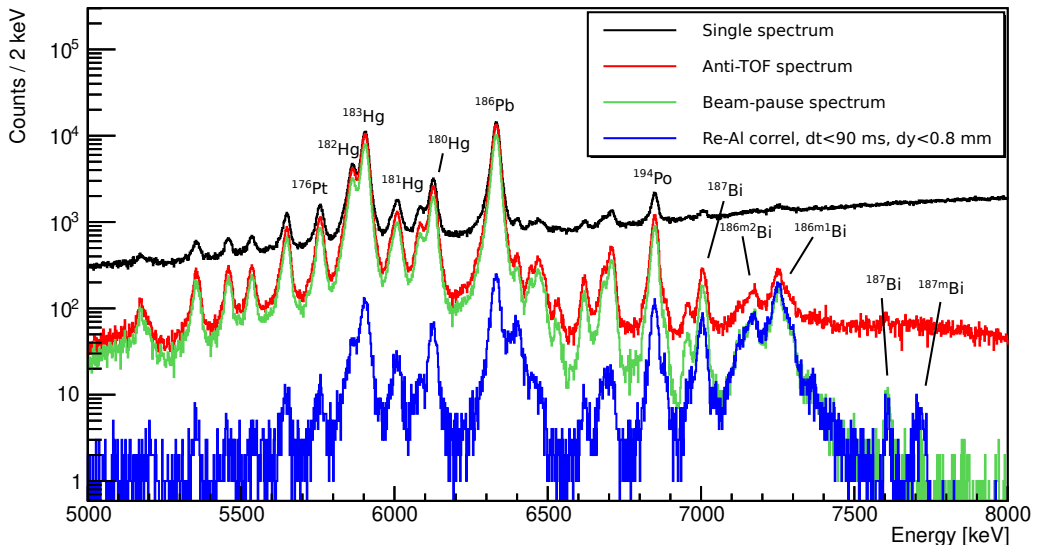


Figure 3.8: Effects of different methods for the background suppression. The black line represents all events in the STOP detector, the red line represents events in anti-coincidence with the TOF system, the green line shows events from the beam-pause and the blue line denotes events from the ER- α correlation search within 90 ms time window and 0.8 mm position window.

Fig. 3.8 demonstrates the effect of the correlation method. Nuclides $^{186,187}\text{Bi}$ have rather short half-lives with 10–15 ms of $^{186m1,m2}\text{Bi}$, 0.37 ms of ^{187m}Bi and 37 ms of ^{187g}Bi . The correlation search with the time window of 90 ms does not reduce the number of decays of these isotopes in comparison to the beam-pause spectrum. On the other hand, the statistics of the longer-living isotopes with half-lives of 4.82 s (^{186}Pb), 0.392 s (^{194}Po) and 9.4 s ^{183}Hg are heavily reduced, by roughly two orders of magnitude, but are still present mainly as the random correlations.

3.5.3 Statistical analysis in case of poor statistics

The amount of the studied events is often not sufficient to use the statistical analysis. K.-H. Schmidt in [Sch84a] presented several relations to calculate the significance of correlated chains and estimate uncertainties of a number of events and half-lives, even in the case of singular events.

Random correlations evaluation

In case of high half-lives of the correlated nuclei, large time window conditions must be used and random correlations start to appear. The amount of random correlations n_r can be estimated as in [Sch84a]:

$$n_r = T \lambda_1 \dots \lambda_i \Delta t_{1,2} \dots \Delta t_{i,i+1} \quad (3.2)$$

where T is the total measure time, i is the total number of correlation groups, λ_i is the counting rate (events per second) of the corresponding group and $\Delta t_{i,i+1}$ is the corresponding correlation time window between i and $i+1$ group. The counting rate also reflects the correlation position window.

Error determination for small numbers

Countrate uncertainties - Poisson distribution The probability of observing n events while μ is the mean value of the number of events is described by the Poisson distribution:

$$p(n|\mu) = \frac{\mu^n}{n!} e^{-\mu} \quad (3.3)$$

For the confidence level $(1 - \varepsilon)$ (ε is an error probability) and observed events n_m , the confidence lower (μ_l) and upper (μ_u) limits are given as the solutions of the following equations:

$$\begin{aligned} \sum_{n=n_m}^{\infty} p(n|\mu_l) &= 1 - \sum_{n=0}^{n_m-1} \frac{\mu_l^n}{n!} e^{-\mu_l} = \frac{\varepsilon}{2} \\ \sum_{n=0}^{n_m} p(n|\mu_u) &= \sum_{n=0}^{n_m} \frac{\mu_u^n}{n!} e^{-\mu_u} = \frac{\varepsilon}{2} \end{aligned} \quad (3.4)$$

An accurate approximation of the lower and upper confidence limits for small numbers and $n_m \geq 2$ is

$$\begin{aligned}\mu_l &\approx n_m - z\sqrt{n_m} \\ \mu_u &\approx n_m + z(1 + \sqrt{n_m})\end{aligned}\tag{3.5}$$

Parameter z is related to the chosen confidence level $(1 - \varepsilon)$ through

$$\frac{\varepsilon}{2} = \int_z^\infty \frac{1}{\sqrt{2\pi}} e^{-x^2/2} dx\tag{3.6}$$

and for the standard error $z = 1$ (confidence level $(1 - \varepsilon) = 0.68$). This approximation for small numbers is much more accurate than the conventionally used symmetric errors

$$n_m - \mu_l = \mu_u - n_m = z\sqrt{n_m}\tag{3.7}$$

Comparison of the exact confidence limits given by the equation 3.4, the approximation by the equation 3.5 and the symmetric errors (Eq. 3.7) is in Fig. 3.9a. Standard errors for $n_m \leq 2$ are summarized in Tab. 3.1.

Lifetime uncertainties - exponential distribution The arithmetic mean \bar{t}_m of the lifetimes $(t_m)_i$ at which the events were observed gives the maximum likelihood estimate of the lifetime τ :

$$\bar{t}_m = \frac{1}{n} \sum_{i=1}^n (t_m)_i\tag{3.8}$$

The confidence lower (τ_l) and upper (τ_u) limits of the lifetime determination of n observed events can be expressed as the solution of the following equations

$$\int_0^{\bar{t}_m} p_n(t|\tau_u) dt = 1 - \sum_{n=0}^{n-1} \left(\frac{n\bar{t}_m}{\tau_u} \right)^n \frac{1}{n!} e^{-n\bar{t}_m/\tau_u} = \frac{\varepsilon}{2}\tag{3.9}$$

where \bar{t}_m is the observed value for \bar{t} and \bar{t} is the mean observed value. An accurate approximation for these confidence limits for small numbers and $n \geq 2$ is

$$\begin{aligned}\tau_l &\approx \frac{\bar{t}_m}{1 + z/\sqrt{n}} \\ \tau_u &\approx \frac{\bar{t}_m}{1 - z/\sqrt{n}}\end{aligned}\quad (3.10)$$

Parameter z is expressed by the equation 3.6. This approximation is much more accurate than the conventionally used symmetric errors

$$\bar{t}_m - \tau_l = \tau_u - \bar{t}_m = z \frac{\bar{t}_m}{\sqrt{n}} \quad (3.11)$$

Comparison of the exact confidence limits given by the equation 3.5.3, the approximation by the equation 3.10 and the symmetric errors (Eq. 3.11) is in Fig. 3.9b. Standard errors (confidence level $(1 - \varepsilon) = 0.68$) for $n_m \leq 2$ are summarized in Tab. 3.1.

Table 3.1: Standard errors (confidence level $(1 - \varepsilon) = 0.68$) for number of observed events $n \leq 2$, calculated from the equations 3.4 (Countrate column) and 3.5.3 (Lifetime column). Cases where the approximations by the equations 3.5 and 3.10 are within 10% from the exact values are given in parentheses.

Number of observed counts n	Countrate		Lifetime	
	μ_l	μ_u	τ_l/\bar{t}_m	τ_u/\bar{t}_m
0	0	1.84	-	-
1	0.173	(3.3)	(0.543)	5.79
2	(0.708)	(4.64)	(0.606)	(2.82)

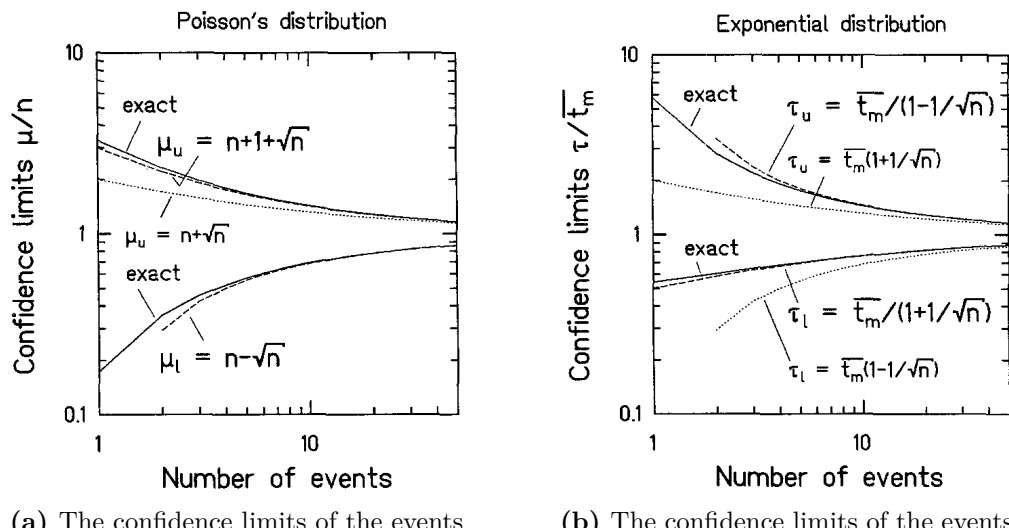


Figure 3.9: Confidence limits for a confidence level $(1 - \varepsilon) = 0.68$ ($z = 1$) as the functions of observed events. Solid lines denote exact values derived from the equations 3.4 and 3.5.3, dashed lines are approximations from the equations 3.5 and 3.10, in figs. 3.9a and 3.9b, respectively. Dotted lines denote conventional symmetric errors. Figure reprinted from [Sch84a].

Chapter 4

Results and discussion

This chapter presents and discusses the results from two independent analyses. The first part focuses on the study of production systematics of fusion-evaporation reactions leading to compound nuclei around radon ($Z=86$). The results from the analysis of experimental data from three fusion-evaporation reactions leading to $^{199,201,202}\text{Rn}^*$ measured at SHIP during run R243 are presented and discussed. The recent results from the experimental measurements aimed at synthesizing new astatine neutron-deficient isotopes are also presented. Additional cross section data for the reactions leading to radon and astatine compound nuclei were extracted from the literature. From the comparison of experimental and theoretical excitation functions by the statistical model code HIVAP , a fission-barrier scaling parameter was determined for each reaction, and a function of the barrier-scaling with respect to the mass number of the compound nucleus was derived for radon and astatine isotopes.

The second part revolves around the decay spectroscopy of ^{186}Bi based on data measured at two experiments (runs R206 and R224) at SHIP. The new results derived from the α - γ coincidence analysis are presented and an improved decay scheme of both isomers in ^{186}Bi is proposed. An extensive discussion of the situation in even- A light bismuth isotopes, regarding the level configurations and recent results is presented as well. The main results from this analysis will be submitted in the journal Physical Review C—draft of the article is ready **ADD A REFERENCE (TO BE SUBMITTED)**.

4.1 Production of isotopes from radon region

4.1.1 Reactions leading to radon compound nuclei

New data for $^{199,201,202}\text{Rn}^*$

The experimental data from three fusion-evaporation reactions $^{52}\text{Cr} + ^{147,149,150}\text{Sm} \rightarrow ^{199,201,202}\text{Rn}^*$ measured at SHIP were analysed. The data were acquired by an experimental campaign during run R243. The experimental details are summarized in Table 4.1. Each studied reaction was measured at several beam energies, allowing a reliable determination of the excitation functions.

Table 4.1: Experimental details of the reactions leading to radon compound nuclei measured at SHIP separator during run R243.

Beam	Target	CN	Beam energy* [MeV]	Beam intensity [pnA]	Target thickness † [$\mu\text{g}/\text{cm}^2$]
$^{52}\text{Cr}^{13+}$	$^{147}\text{SmF}_3$	$^{199}\text{Rn}^*$	222–261	540 – 670	496
	$^{149}\text{SmF}_3$	$^{201}\text{Rn}^*$	219–251	670 – 930	464
	$^{150}\text{SmF}_3$	$^{202}\text{Rn}^*$	220–236	790	338

* Beam energy in the middle of the target

† The thickness of the compound target

We identified evaporation residues $^{195–200}\text{Rn}$ in the studied reactions. The α -decay properties of the produced ERs and their corresponding α -decay products are summarized in Table 4.2.

The relatively short half-lives of both mother and daughter isotopes produced in the studied reactions allowed the use of Recoil- α - α correlation search, for more details see Section 3.5.2. In all cases, a correction for the real number of events was used to compensate for the loss of statistics due to half-lives $T_{1/2}$ and correlation time windows ΔT :

$$N_{real} = N_{det} \times \left(1 - e^{-\ln 2 \frac{\Delta T}{T_{1/2}}}\right) \quad (4.1)$$

This correction is especially significant in the case of heavier evaporation residues produced in the analyzed reactions, such as $^{199,200}\text{Rn}$, where the correlation time windows were comparable or shorter than the half-lives. The SHIP transmission

Table 4.2: The α -decay properties of radon isotopes produced in the reactions $^{52}\text{Cr} + ^{147,149,150}\text{Sm} \rightarrow ^{199,201,202}\text{Rn}^*$ at SHIP separator. The reported uncertainties of $T_{1/2}$ and b_α from the literature were significantly lower than the statistical and/or other systematic uncertainties, therefore, they are not stated in this table.

Mother	Daughter	E_α [keV]	$T_{1/2}$ [ms]	b_α	Ref.
^{195}Rn		7536	6	1	[Ket01]
	^{191}Po	~ 7335	22	0.909	[And02b]
^{195m}Rn		7555	5	1	[Ket01]
	^{191m}Po	7376	93	0.457	[And02b]
^{196}Rn		7462	4.4	0.998	[ENS24]
	^{192}Po	7167	32.2	0.986	[ENS24]
^{197}Rn		7260	55	1	[Enq96; And08]
	^{193}Po	6948	388	0.993	[ENS24; Van02]
^{197m}Rn		7356	24	1	[And08]
	^{193m}Po	7002	245	0.992	[ENS24; Van02]
^{198}Rn		7196	65	0.99	[ENS24]
	^{194}Po	6843	392	0.927	[ENS24]
^{199}Rn		6989	590	0.94	[ENS24; Tay99; Uus05]
	^{195}Po	6611	4640	0.936	[ENS24]
^{199m}Rn		7060	310	0.97	[ENS24; Tay99; Uus05]
	^{195m}Po	6700	1920	0.9	[ENS24]
^{200}Rn		6902	960	0.98	[Cal84; Wau93]
	^{196}Po	6522	5600	0.94	[ENS24]

of 50(10)% for the $^{52}\text{Cr}-^{147,149,150}\text{Sm}$ projectile-target combination was used in the analyzed reactions, see Sec. 3.2 and Fig. 3.3. The stated uncertainties in Table 4.1 and all figures of excitation functions are statistical only. We estimate the typical absolute uncertainty of the cross section values near the maxima of the excitation functions to be $\pm 40\%$, arising primarily from the uncertainty of the SHIP transmission. The deduced cross section values for the xn evaporation channels are summarized in Table 4.3.

Table 4.3: The cross section values for the three analyzed reactions measured at SHIP by the evaporation channel. Asymmetric uncertainties are reported for datapoints with low statistics and were calculated as described in Sec. 3.5.3. The data with the theoretical calculations by the HIVAP code are visually displayed in Figs. 4.2, 4.3 and 4.4

Reaction	E_{proj} [MeV] [*]	σ [nb]			
		2n	3n	4n	5n
$^{52}\text{Cr} + ^{147}\text{Sm} \rightarrow ^{199}\text{Rn}^*$ (Fig. 4.2)	221.8	6.0(11)			
	224.9	$4.1^{+1.6}_{-1.2}$	$0.2^{+0.5}_{-0.2}$		
	232.6	$0.7^{+0.3}_{-0.2}$	0.5(2)		
	235.8	1.2(2)	1.3(2)		
	252.1	0.2(1)	0.09(4)	0.4(1)	
	260.5		$0.1^{+0.2}_{-0.1}$	$0.2^{+0.5}_{-0.2}$	
$^{52}\text{Cr} + ^{149}\text{Sm} \rightarrow ^{201}\text{Rn}^*$ (Fig. 4.3)	218.9	36(2)	28(1)		
	222.1	30(3)	41(2)		
	229.4	18(1)	55(1)	1.4(1)	
	233.6	12(3)	47(4)	7.0(12)	
	236.2		8.6(12)	16(2)	
	244.5		2.1(5)	14(1)	$0.08^{+0.19}_{-0.07}$
	251.3		1.2(4)	6.2(8)	$0.2^{+0.2}_{-0.1}$
$^{52}\text{Cr} + ^{150}\text{Sm} \rightarrow ^{202}\text{Rn}^*$ (Fig. 4.4)	220.4	130(16)	430(24)	$1.0^{+0.9}_{-0.6}$	
	228.3	120(4)	640(8)	6.1(4)	
	236.1	170(22)	170(17)	91(6)	

* Beam energy in the center of the target. Energy losses were calculated with the LISE++ software [Tar08]

An interesting feature of reactions employing samarium targets is the unusual shape and width of the excitation functions. The element samarium has seven naturally abundant isotopes— ^{144}Sm , $^{147-150}\text{Sm}$, ^{152}Sm , and ^{154}Sm . The isotopic enrichment of the targets does not eliminate undesired isotopes of the target material entirely, which are therefore present in the enriched targets as admixtures **FIND AND ADD CITATION**. Especially heavier isotopes of the target material may influence the production of isotopes significantly since the production cross section

rises significantly with the mass number of the target isotope. Additionally, the non-zero thickness of the target leads to the spread of the projectile energies due to the energy losses in the target material. As a result, the experimental excitation functions are often wider than the theoretical ones, which can be seen also in our data, for example in $2n$ (^{197}Rn) channel in the $^{52}\text{Cr} + ^{147}\text{Sm}$ reaction.

Reaction $^{52}\text{Cr} + ^{147}\text{Sm} \rightarrow ^{199}\text{Rn}^*$ The reaction leading to the lightest studied radon compound nucleus, $^{199}\text{Rn}^*$, was measured at four beam energies above and two below the Bass interaction barrier. The $(2 - 4)n$ evaporation channels were observed, corresponding to the $^{197-195}\text{Rn}$ ERs, respectively. These produced radon isotopes have well-defined α -decay energies as well as relatively short half-lives, see Tab. 4.2, allowing the use of the ER- α - α correlation search with narrow time windows, see Fig. 4.1. The groups of $^{195}\text{Rn}-^{191}\text{Po}$, $^{196}\text{Rn}-^{192}\text{Po}$ and $^{197}\text{Rn}-^{193}\text{Po}$ mother-daughter pairs are distinguishable from the rest of the events, mainly caused by the random correlations of the most intense α decays of other produced isotopes.

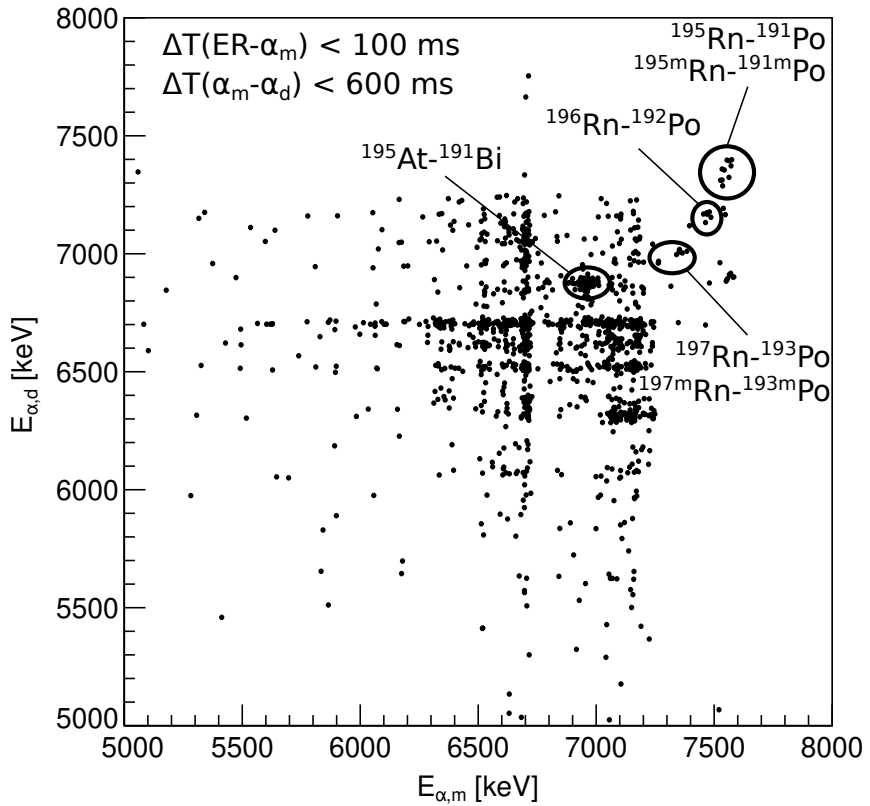


Figure 4.1: An example of the 2D spectrum of events from the ER- α_m - α_d correlation search in the reaction $^{52}\text{Cr} + ^{147}\text{Sm} \rightarrow ^{199}\text{Rn}^*$ measured at the 252.1 MeV beam energy. The time windows used were $\Delta T(\text{ER}-\alpha_m) < 100$ ms and $\Delta T(\alpha_m-\alpha_d) < 600$ ms. The α_m - α_d groups corresponding to the $2n - 4n$ evaporation channels are labeled.

The evaluated cross sections are summarized in Table 4.3 and the resulting excitation functions, together with the HIVAP calculations, are displayed in Fig. 4.2. The isotope ^{195}Rn was also produced at much higher energy than the HIVAP calculations predict. We attribute this observation to the widening of the excitation functions caused by the heavier samarium admixtures in the target material and by the projectile-energy spread, see above for the explanation.

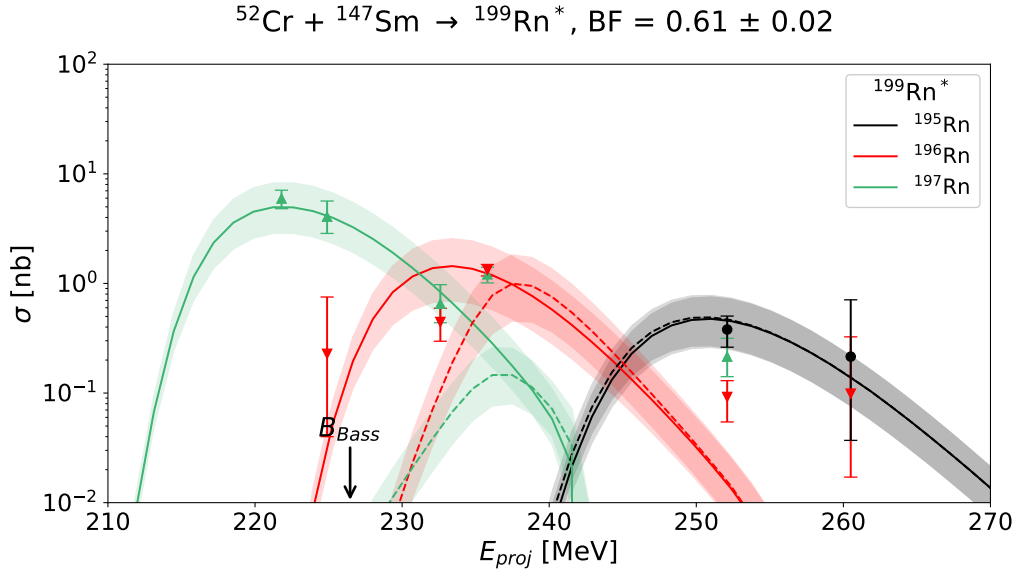


Figure 4.2: The experimental (points) and theoretical (lines) excitation functions for the reaction $^{52}\text{Cr} + ^{147}\text{Sm} \rightarrow ^{199}\text{Rn}^*$. The solid lines denote the HIVAP calculations according to the barrier-fluctuations approach, the dashed lines are for the inverted-parabola parametrization, see Sec. 2.1.2. The matching semi-transparent shadow around the lines denotes the calculation with the $\text{BF} \pm 0.02$ parameter. The Bass interaction barrier calculated by Eq. 2.6 is denoted by the black arrow.

The best reproduction of the experimental data from the $^{52}\text{Cr} + ^{147}\text{Sm} \rightarrow ^{199}\text{Rn}^*$ reaction was achieved by the HIVAP with the barrier-scaling parameter of $\text{BF}=0.62$, deduced primarily from the maxima of $3n$ (^{196}Rn) and $4n$ (^{195}Rn) evaporation channels, located near/above the fusion barrier. The maximum of the $2n$ channel (^{197}Rn) lies below the Bass barrier, where the reliability of the HIVAP is rather uncertain. However, in this case, this excitation function is well reproduced by the barrier-fluctuations approach of the HIVAP calculations.

Reaction $^{52}\text{Cr} + ^{149}\text{Sm} \rightarrow ^{201}\text{Rn}^*$ The reaction leading to the $^{201}\text{Rn}^*$ was measured at seven beam energies, of which two were below the Bass interaction barrier. Four evaporation channels were observed, $(2 - 5)n$, corresponding to the ERs of

$^{199-196}\text{Rn}$, respectively. The resulting excitation functions are shown in Figure 4.3.

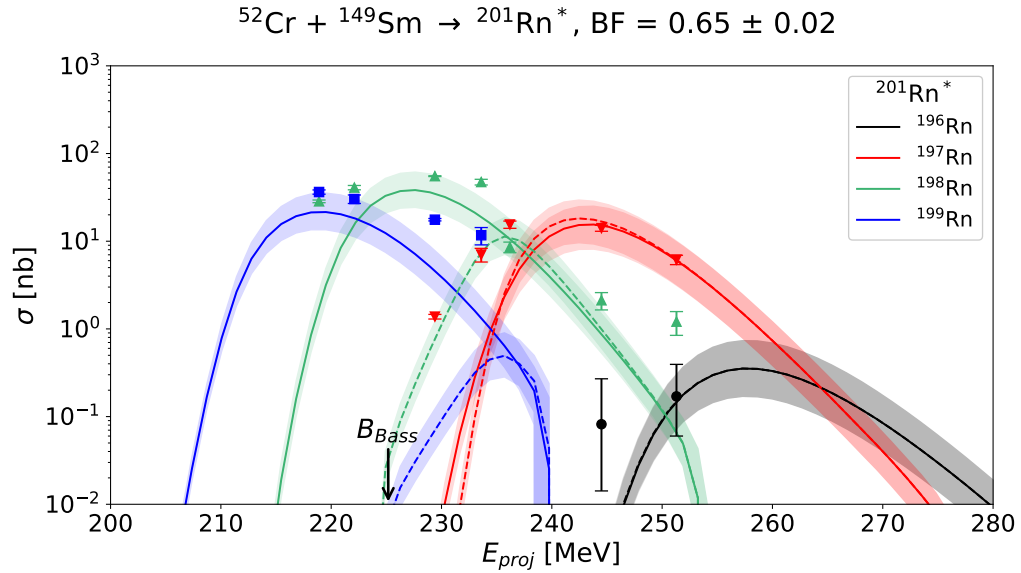


Figure 4.3: The same as in Fig. 4.2, but for the reaction $^{52}\text{Cr} + ^{149}\text{Sm} \rightarrow ^{201}\text{Rn}^*$.

A good agreement between the experimental data and theoretical calculations was achieved by using the $\text{BF}=0.65$ value in the HIVAP calculations. Maxima and overall shapes of all observed excitation functions were reproduced satisfactorily by the barrier-fluctuations approach both above and below the Bass interaction barrier.

Reaction $^{52}\text{Cr} + ^{150}\text{Sm} \rightarrow ^{202}\text{Rn}^*$ The reaction $^{52}\text{Cr} + ^{150}\text{Sm} \rightarrow ^{202}\text{Rn}^*$ was measured at three beam energies. Evaporation residues $^{200-198}\text{Rn}$ corresponding to the $(2-4)n$ evaporation channels were identified, respectively. The maxima of the corresponding excitation functions were satisfactorily reproduced by the calculations with the $\text{BF}=0.70$ value, see Fig. 4.4. The barrier-fluctuations variant of the HIVAP calculations provided the best agreement, even below the Bass interaction barrier. The $2n$ (^{200}Rn) evaporation channel was most likely influenced by the heavier samarium admixtures in the target, see the beginning of this section.

Literature data

The experimental data from nine additional fusion evaporation reactions leading to radon compound nuclei were obtained from the available literature, see Table 4.4. The corresponding plots of the excitation functions together with the HIVAP calculations are in Sec. A in figures A.1–A.12. The following paragraphs will briefly describe the literature data and the corresponding determination of the barrier-scaling

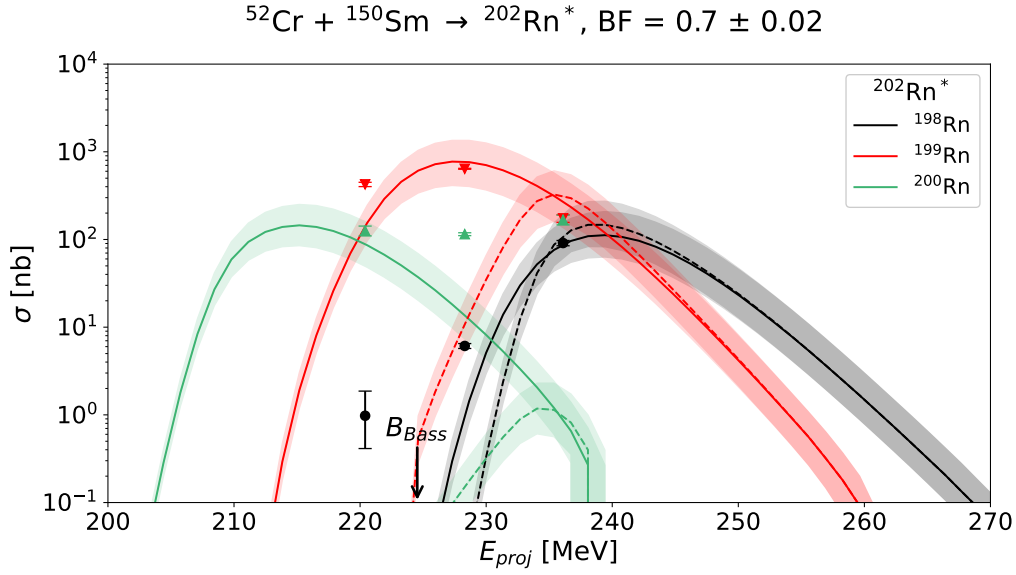


Figure 4.4: The same as in Fig. 4.2, but for the reaction $^{52}\text{Cr} + ^{150}\text{Sm} \rightarrow ^{202}\text{Rn}^*$.

factor for each reaction and compound nucleus. The reactions and the deduced barrier-scaling values are summarized in Table 4.4.

$^{196}\text{Rn}^*$ Two datapoints for the $^{52}\text{Cr} + ^{144}\text{Sm}$ reaction were published in the α -decay spectroscopy study of $^{193,194}\text{Rn}$ [And06a]. The reported cross section values for these isotopes have relatively large uncertainties, however, they are well-reproduced by the HIVAP with the BF=0.52 value (Fig. A.1).

$^{198}\text{Rn}^*$ In the α -decay studies of $^{195,196}\text{Rn}$, the peak cross section values for these ERs were reported [Ket01]. The maximum of the $2n$ (^{196}Rn) channel is near the Bass interaction barrier, therefore the BF=0.61 parameter for the HIVAP calculation was deduced only from the $3n$ (^{195}Rn) evaporation channel, (Fig. A.2).

$^{200}\text{Rn}^*$ One value for the cross section of ^{197}Rn was reported in the study of $^{197,199,201}\text{Rn}$ [And08]. The value of BF=0.65 was deduced for this datapoint, (Fig. A.4).

$^{202}\text{Rn}^*$ Besides the data obtained in the present study for the $^{202}\text{Rn}^*$ compound nucleus, one datapoint for the ^{198}Rn isotope from the reaction $^{36}\text{Ar} + ^{166}\text{Er}$ was reported in the γ -decay study of ^{198}Rn [Tay99]. The HIVAP calculations best reproduced this data with the BF=0.74 value A.7. Albeit just one datapoint available

for this reaction, this barrier-scaling value is in agreement with the value of 0.70 deduced for the $^{52}\text{Cr}+^{150}\text{Sm}$ reaction in this work.

$^{204}\text{Rn}^*$ Data for two reactions leading to the $^{204}\text{Rn}^*$ are available—two datapoints for the $^{197,198}\text{Rn}$ ERs studied in the $^{35}\text{Cl}+^{169}\text{Tm}$ reaction in the discovery of the ^{197}Rn isotope [Enq96]; one datapoint for the ^{200}Rn ER measured in the $^{28}\text{Si}+^{176}\text{Hf}$ reaction in its γ -decay study [Tay96]. The value of $\text{BF}=0.75$ was deduced for the $^{35}\text{Cl}+^{169}\text{Rm}$ reaction, see Fig. A.8 (Fig. A.8). Slightly lower value of 0.70 was deduced for the $^{28}\text{Si}+^{176}\text{Hf}$ reaction (Fig. A.9). However, both values are within the uncertainty of each other.

$^{206}\text{Rn}^*$ In the study of ^{44}Ca -induced reactions, cross section data for the $^{44}\text{Ca}+^{162}\text{Dy}$ reaction were reported at several beam energies [Wer15a]. The data for $(3-5)n$ ($^{203-201}\text{Rn}$) evaporation channels were reproduced satisfactorily by the HIVAP calculations with the barrier-scaling value of 0.73 (Fig. A.10).

$^{210}\text{Rn}^*$ In the study of the $^{48}\text{Ca}+^{162}\text{Dy}$, cross section data for $3n$ and $6n$ evaporation channels were presented [May15]. The partial excitation function of the $6n$ channel is shifted towards lower beam energies. However, the maxima of the two excitation functions were reproduced by the HIVAP calculations with the barrier scaling of 0.74 (Fig. A.11).

$^{212}\text{Rn}^*$ In the work reporting about the upgrade of the kinematic separator VAS-SILISSA [Yer03], cross section data for the reaction $^{22}\text{Ne}+^{190}\text{Os}$ were presented as the maximum values for $(7-12)n$ evaporation channels, corresponding to $^{205-200}\text{Rn}$. We reached the best agreement between the experimental data and the HIVAP predictions with the $\text{BF}=0.84$ value (Fig. A.12).

4.1.2 Reactions leading to astatine compound nuclei

Reactions leading to $^{192,193}\text{At}^*$

The experimental measurements focused on the study of the lightest astatine isotopes $^{189,190}\text{At}$ were measured in Argonne National Laboratory (Chicago, USA) (see proposal number 2013 in Ref. [ANL22]). Isotopes of interest were intended to be synthesized in two fusion-evaporation reactions:

- $^{90}\text{Zr}+^{103}\text{Rh} \rightarrow ^{193}\text{At}^* \rightarrow ^{190}\text{At} + 3n$

- Measured in the summer of 2022.
- The energy of ^{90}Zr beam was 410 MeV.
- Expected total yield of ^{190}At was 300 nuclei at 2 nb peak cross section.
- $^{93}\text{Nb} + ^{99}\text{Ru} \rightarrow ^{192}\text{At}^* \rightarrow ^{189}\text{At} + 3n$
 - Measured in the spring of 2023.
 - The energy of ^{93}Nb beam was 422 MeV.
 - Expected total yield of ^{189}At was 160 nuclei at 0.5 nb peak cross section.

The reaction products were separated by the gas-filled AGFA separator. The results from the first reaction were published in an α -decay study of ^{190}At [And23]. Only four full-energy events attributed to ^{190}At were observed and the cross section for the production of ^{190}At was reported to be 0.13 nb. which is more than one order of magnitude lower than the predicted 2 nb.

Literature data

In total, cross section data from 18 additional fusion-evaporation reactions leading to 9 astatine compound nuclei were studied. The corresponding excitation functions are shown in Figs. B.1–B.18. The upcoming paragraphs will shortly discuss the literature data and the deduced barrier-scaling values. The reaction and the corresponding BF values are summarized in Table 4.4.

$^{195}\text{At}^*$ Data from two reactions leading to this compound nucleus were . Only one datapoint for each reaction was stated in the literature. The first reaction $^{51}\text{V} + ^{144}\text{Sm}$ was measured at SHIP and the data were reported in the α -decay study of ^{192}At Ref. [And06b]. The second reaction $^{54}\text{Fe} + ^{141}\text{Pr}$ was measured at RITU separator at the University of Jyväskylä (Finland), where new isotopes $^{191,193}\text{At}$ were first observed [Ket03a]. The HIVAP calculations for these two reactions reproduced the experimental data the best with the BF=0.63 and 0.58 values (Figs. B.2 and B.3), respectively. Both values are within the uncertainty of each other.

$^{197}\text{At}^*$ The reaction $^{56}\text{Fe} + ^{141}\text{Pr}$ was measured at SHIP and RITU separators and the respective cross section data were reported in Refs. [And16] and [Ket03a; Ket03b]. The data from SHIP included the full excitation functions of $3n$ and

$4n$ evaporation channels, while the data reported from RITU contained one datapoint for each of the $(2-4)n$ evaporation channels. Both datasets were satisfactorily reproduced by the HIVAP calculations with the BF=0.67 parameter (Fig. B.4).

$^{198}\text{At}^*$ The cross section data for $(2-4)n$ evaporation channels in the reaction $^{51}\text{V} + ^{147}\text{Sm}$ were reported in the spectroscopy study of $^{194-196}\text{At}$ [Nym13]. The data were measured at one beam energy, corresponding to the peak production of the $3n$ (^{195}At) evaporation channel. Therefore, the other two reported values could not be reliably used for the determination of the barrier-scaling parameter, due to the broadening of the excitation functions caused by the admixtures in the target (especially in the samarium targets) and the projectile energy losses. A good agreement between the cross section of the $3n$ channel and HIVAP calculation was achieved with the barrier-scaling of 0.65.

$^{199}\text{At}^*$ In the cross-section studies of astatine and polonium reactions, the experimental data from the $^{40}\text{Ca} + ^{159}\text{Tb}$ reaction corresponding to partial excitation functions of $p(2,3)n$ evaporation channels were presented [And90].

$^{201}\text{At}^*$

$^{202}\text{At}^*$

$^{203}\text{At}^*$

$^{205}\text{At}^*$

$^{207}\text{At}^*$

4.1.3 Barrier-scaling systematics

All analyzed reactions with the deduced barrier-scaling factors are summarized in Table 4.4. The BF values in italics denote the reactions, for which only one datapoint was available. Both radon and astatine compound nuclei show a similar linear trend of the barrier-scaling factor. The

Table 4.4: Reactions used in this work to deduce the barrier-scaling parameter. The BF values deduced from one datapoint are denoted by *italics*. Reaction denoted by * was recently measured at the Argonne National Laboratory and the data are not published yet. The results from the reactions denoted by † symbol are from unpublished data from SHIP separator analyzed in this work, see Sec. 4.1.1 and 4.1.2. The presented barrier-scaling data are visualized in Fig. 4.5. The numbers in the first column refer to the labeled datapoints in Fig. 4.6. **ADD REF TO QUASI-FISSION SECTION**

Reaction number	Reaction	CN	Ref.	X_{mean}	BF
1	$^{93}\text{Nb} + ^{99}\text{Ru}$	^{192}At	*	0.757	
2	$^{90}\text{Zr} + ^{103}\text{Rh}$	^{193}At	[And23]	0.754	0.44
3	$^{51}\text{V} + ^{144}\text{Sm}$	^{195}At	[And06b]	0.685	0.64
4	$^{54}\text{Fe} + ^{141}\text{Pr}$	^{195}At	[Ket03a]	0.715	0.64
5	$^{56}\text{Fe} + ^{141}\text{Pr}$	^{197}At	[And16]	0.707	0.67
	$^{56}\text{Fe} + ^{141}\text{Pr}$		[Ket03a], [Ket03b]		0.67
6	$^{51}\text{V} + ^{147}\text{Sm}$	^{198}At	[Nym13]	0.682	0.67
7	$^{40}\text{Ca} + ^{159}\text{Tb}$	^{199}At	[Yer03]	0.672	0.76
8	$^{45}\text{Sc} + ^{156}\text{Gd}$	^{201}At	[Wer15c]	0.668	0.65
9	$^{45}\text{Sc} + ^{157}\text{Gd}$	^{202}At	[Wer15c]	0.667	0.67
10	$^{45}\text{Sc} + ^{158}\text{Gd}$	^{203}At	[Wer15c]	0.666	0.68
11	$^{44}\text{Ca} + ^{159}\text{Tb}$	^{203}At	[Wer15b]	0.654	0.69
12	$^{45}\text{Sc} + ^{160}\text{Gd}$	^{205}At	[Wer15c]	0.664	0.68
13	$^{24}\text{Mg} + ^{181}\text{Ta}$	^{205}At	[And90]	0.574	0.79
14	$^{40}\text{Ar} + ^{165}\text{Ho}$	^{205}At	[Ver84]	0.632	0.80
	$^{40}\text{Ar} + ^{165}\text{Ho}$		[And90]		0.79
	$^{40}\text{Ar} + ^{165}\text{Ho}$		[Jak10]		0.73

Table continues on the next page.

Table 4.4: (*continued*)

Reaction number	Reaction	CN	Ref.	X_{mean}	BF
	$^{40}\text{Ar} + ^{165}\text{Ho}$		[Fol12]	0.79	
15	$^{26}\text{Mg} + ^{181}\text{Ta}$	^{207}At	[Yer03]	0.561	0.81
16	$^{48}\text{Ca} + ^{159}\text{Tb}$	^{207}At	[May14]	0.638	0.83
17	$^{52}\text{Cr} + ^{144}\text{Sm}$	^{196}Rn	[And06a]	0.704	0.51
18	$^{56}\text{Fe} + ^{142}\text{Nd}$	^{198}Rn	[Ket01]	0.715	0.61
19	$^{52}\text{Cr} + ^{147}\text{Sm}$	^{199}Rn	†	0.700	0.61
20	$^{82}\text{Kr} + ^{118}\text{Sn}$	^{200}Rn	[And08]	0.746	0.65
21	$^{52}\text{Cr} + ^{149}\text{Sm}$	^{201}Rn	†	0.697	0.65
22	$^{52}\text{Cr} + ^{150}\text{Sm}$	^{202}Rn	†	0.696	0.70
23	$^{36}\text{Ar} + ^{166}\text{Er}$	^{202}Rn	[Tay99]	0.658	0.74
24	$^{35}\text{Cl} + ^{169}\text{Tm}$	^{204}Rn	[Enq96]	0.641	0.75
25	$^{28}\text{Si} + ^{176}\text{Hf}$	^{204}Rn	[Tay96]	0.609	0.70
26	$^{44}\text{Ca} + ^{162}\text{Dy}$	^{206}Rn	[Wer15a]	0.659	0.73
27	$^{48}\text{Ca} + ^{162}\text{Dy}$	^{210}Rn	[May15]	0.643	0.74
28	$^{22}\text{Ne} + ^{190}\text{Os}$	^{212}Rn	[Yer03]	0.530	0.84

* Reaction was recently measured at the Argonne National Laboratory - data not published yet

† Reactions analysed in this work

4.2 Decay spectroscopy of ^{186}Bi

4.2.1 Experimental details

The experiment from Ref. [And03a], employing ^{95}Mo beam, will be denoted as Exp1 [*Note for co-authors: Run 206*], and the measurement from Ref. [Lan13], using ^{46}Ti

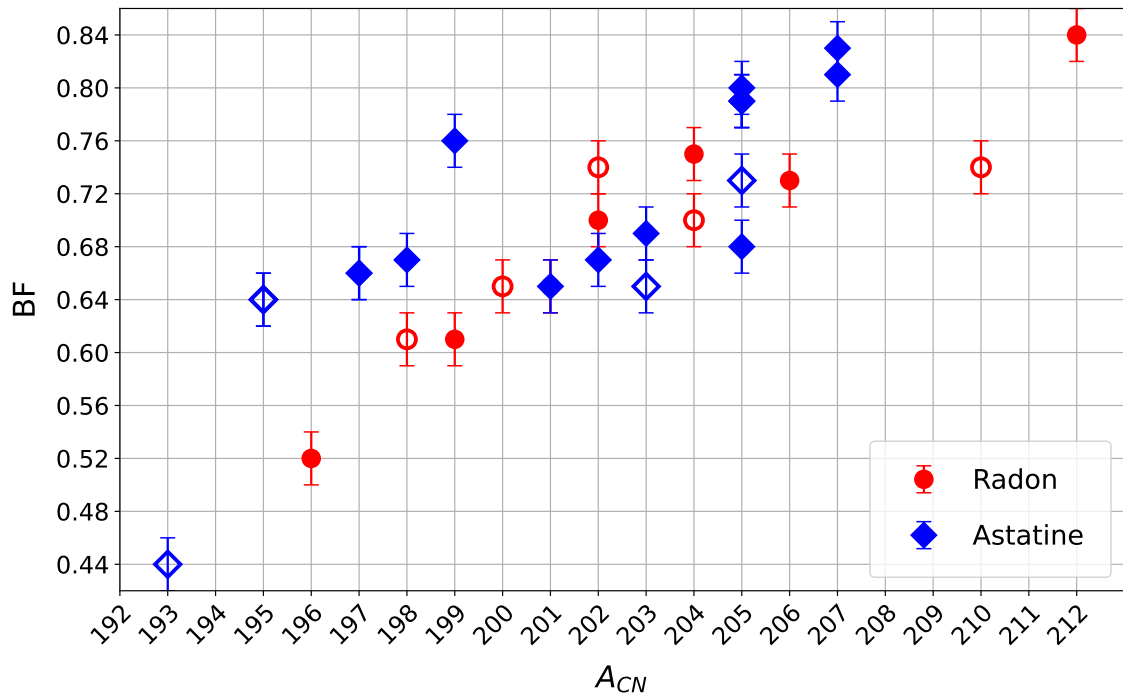


Figure 4.5: Systematics of the liquid-drop model fission barrier scaling for radon (red circles) and astatine (blue diamonds) compound nuclei. The BF values deduced from one datapoint are shown with the empty symbols. The uncertainties represent the BF value intervals (± 0.02), for which the experimental data were satisfactorily reproduced by the statistical model code HIVAP .

beam, will be denoted as Exp2 [*Note for co-authors: Run 224*]. Experimental conditions of both measurements are summarised in Table 4.5.

Table 4.5: Details of the experimental measurements at SHIP, where ^{186}Bi was produced.

Beam	Target	CN	Beam energy [MeV]	Beam intensity [pnA]	Target thickness [$\mu\text{g}/\text{cm}^2$]	Irradiation [h]
Exp1 [And03a]	^{95}Mo	^{93}Nb †	419, 438	10	900	36
Exp2 [Lan13]	$^{46}\text{Ti}^{12+}$	$^{144}\text{SmF}_3$	239	150	300 ‡	70

* Beam energy in front of the target

† Metallic target used

‡ The thickness of the compound target

In both experiments, the beam was provided by the UNILAC heavy-ion accel-

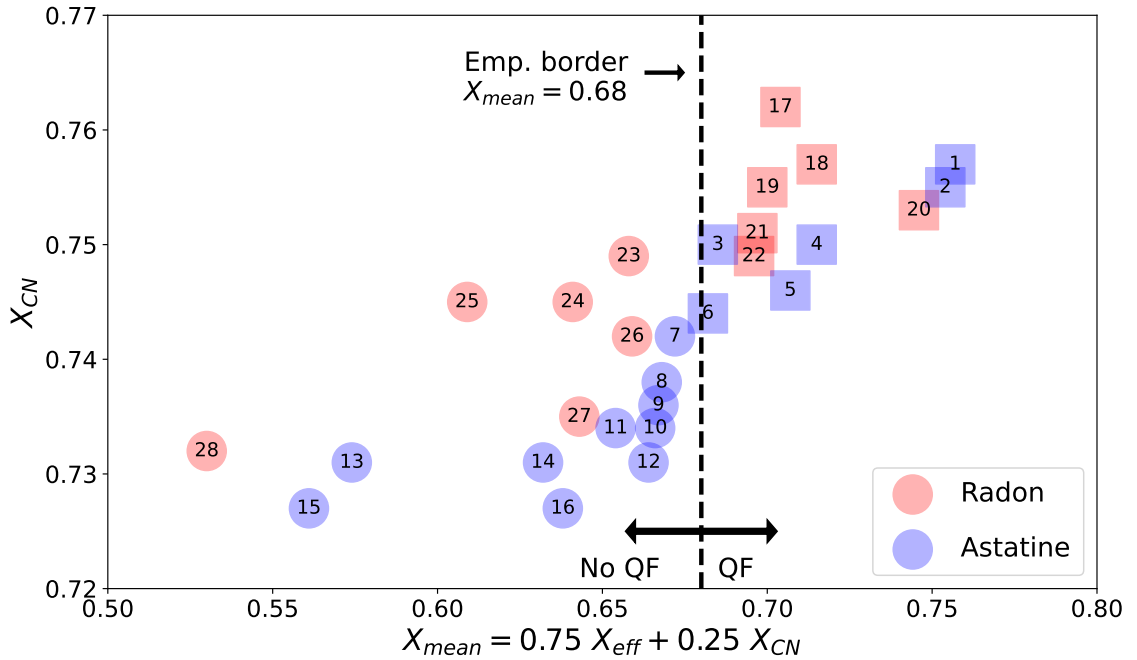


Figure 4.6: Fissility systematics for fusion-evaporation reactions studied in this work, with the fissility parameters calculated according to Ref. [Rie13]. For more details, see Sec. ?? ADD REF. TO QUASI FISSION SECTION. The numbers within the datapoints refer to the first column in Table 4.4, where all studied reactions are summarized.

erator working in the pulse mode (5 ms on/15 ms off) and the target wheel rotated synchronously with the beam macro-pulse structure. The reaction products were separated by the velocity filter SHIP [Mün79; Hof00] and subsequently implanted into the $300\ \mu\text{m}$ thick 16-strip position-sensitive silicon detector (PSSD), with a total area of $35\times80\ \text{mm}^2$. The energy resolution of the PSSD was around 25 and 31 keV (FWHM) for the 6331 keV (^{186}Pb) α -decay peak in Exp1 and Exp2, respectively. The energy calibration of the PSSD in Exp1 was performed by using α -decay energies of isotopes ^{182}Hg (5867(5) keV [Hag79]), ^{183}Hg (5905(5) keV [Hag79]), ^{186}Pb (6331(6) keV [Wan12]) and ^{185}Pb (6408(5) keV [And02a]) produced abundantly in the reaction. In Exp2, the α -decay energies of isotopes ^{200}Po (5861.9(18) keV), ^{200m}At (6411.8(13) keV), ^{200}At (6464.6(13) keV), ^{196}Po (6521.9(21) keV), ^{199}At (6643(3) keV), ^{194}Po (6843(3) keV) and ^{192}Po (7167(3) keV) [ENS24] produced in the reaction $^{51}\text{V}+^{144}\text{Sm}$ measured directly after Exp2 were used for the calibration of the PSSD.

Note on the PSSD calibration We verified the calibration of Exp2 by comparing it to data acquired shortly after Exp2 ended in the reaction $^{51}\text{V}+^{144}\text{Sm}$. We used the 7167(3)-keV α decay of ^{192}Po [ENS24] as a reference point, because of its

comparable energy to the studied ^{186}Bi . Moreover, the calibrations between Exp1 and Exp2 were compared based on the α decay of $^{187g,m}\text{Bi}$ produced abundantly in both experiments with reference energy of $E_\alpha=7000(5)$ keV [ENS24]. We observed a systematic shift of the α -decay energies of about 16 keV towards higher energies in Exp1 for the decay of ^{187}Bi as well as for α particles in coincidence with the 108-keV γ rays from ^{186}Bi . We attribute this discrepancy to the fact that in Exp1 the highest calibration point was at 6408 keV (^{185}Pb). Thus, the extrapolation of the calibration to energies at 7000–7300 keV led to this shift. To account for this effect, the calibration of Exp1 was shifted by 16 keV towards the lower energies. As a result, the strongest α -decay peak of ^{186}Bi has an energy of 7247 keV in both experiments. This value will be used from now on for the most intense α -decay transition from the $^{186m1}\text{Bi}$ isomer instead of the previously reported 7263 keV in Ref. [And03a].

In Exp1, a single coaxial high-purity germanium (HPGe) detector was installed behind the PSSD detector, for X- and γ -ray measurements. In Exp2, a so-called VEGA type clover detector was used instead, consisting of four HPGe crystals (each with a diameter of 70 mm and a length of 140 mm) with a total volume of $(124 \times 124 \times 140)$ mm³ [Kas98]. The energy and relative efficiency calibrations of the HPGe detectors were performed with an external ^{152}Eu source.

A time-of-flight (TOF) detector system [Šár96] was installed upstream from the PSSD, to distinguish between evaporation residues (ER) and scattered projectiles. An anticoincidence condition between one of the TOF detectors and the PSSD provided discrimination between implantation and decay events.

4.2.2 Results and discussion

The ^{186}Bi isotope was produced in Exp1 and Exp2 via $2n$ and $p3n$ evaporation channels, respectively. The obtained statistics of ^{186}Bi in the two experiments are summarised in Table 4.6. A combination of the two datasets increased the total amount of collected ^{186}Bi by a factor of about 2.5, in comparison with the Exp1 [And03a].

The spectra of α particle energies registered within 90 ms after ER implantation and up to 0.8 mm from the implantation position from Exp1 and Exp2 are shown in Fig. 4.7. A relatively broad energy distribution with $E_\alpha\approx7050$ –7400 keV originates from the α decay of $^{186m1,m2}\text{Bi}$ [And03a]. The main peak at 7247(10) keV is dominantly caused by a single α -decay transition from $^{186m1}\text{Bi}$ feeding the 108-keV level in ^{182}Tl assigned in Ref. [And03a], which is also confirmed by the present analysis. The rest of the broad distribution with $E_\alpha\approx7165$ keV is a combination of α -decay

Table 4.6: Summary of ^{186}Bi statistics and half-lives determined from Exp1, Exp2 and the combined dataset. The numbers of events are background-subtracted.

		Exp1	Exp2	Combined data	Lit. Exp1
$^{186m1}\text{Bi}$	$T_{1/2}$ ($E_\alpha=7247\text{ keV}$)	8.6(5) ms	7.2(3) ms	7.8(2) ms	9.8(4) ms
	Number of ER- α events	~2330	~4300	~6630	[And03a]
$^{186m2}\text{Bi}$	$T_{1/2}$ ($E_\alpha=7120 - 7200\text{ keV}$)	14.8(19) ms	9.4(5) ms	9.9(4) ms	14.8(8) ms
	Number of ER- α events	~810	~2100	~2910	[And03a]

fine-structure transitions from both $^{186m1}\text{Bi}$ or $^{186m2}\text{Bi}$ isomers, as will be discussed below.

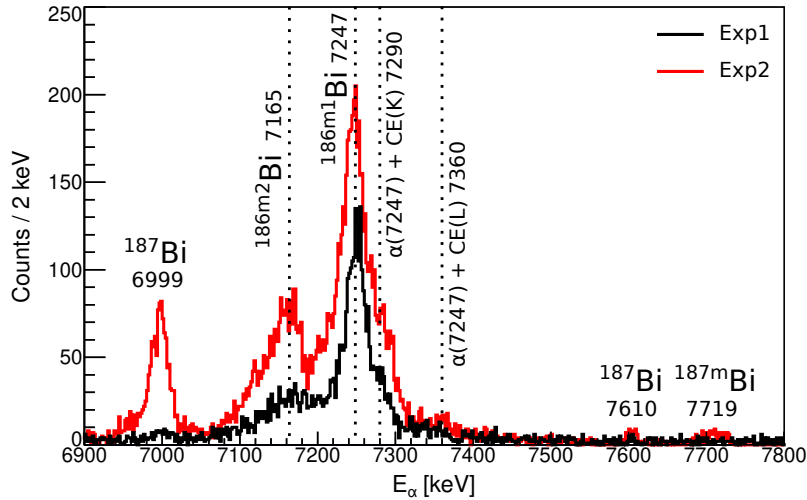


Figure 4.7: Energy spectra from ER- α correlation search with a time condition of $\Delta T(\text{ER} - \alpha) \leq 90\text{ ms}$ from Exp1 (black line) and Exp2 (red line). Dotted vertical lines denote the energies relevant for discussion, see text. The labels $\alpha + CE(K \text{ or } L)$ denote the summed energies of the 7247-keV α -decay peak and conversion electrons from the most intense 108-keV γ transition (see text for details).

The half-lives of both isomers were deduced from the time difference between ER implantations and subsequent α decays. The decay curves were fitted by the maximum-likelihood method. Two decay curves were created for $^{186m1}\text{Bi}$ using two methods: one approach used gating only on the α decays with $E_\alpha=7247\text{ keV}$; the second method required the events with $E_\alpha=7247\text{ keV}$ to be in coincidence with the 108-keV γ rays. Albeit the statistics in the second method are reduced by roughly

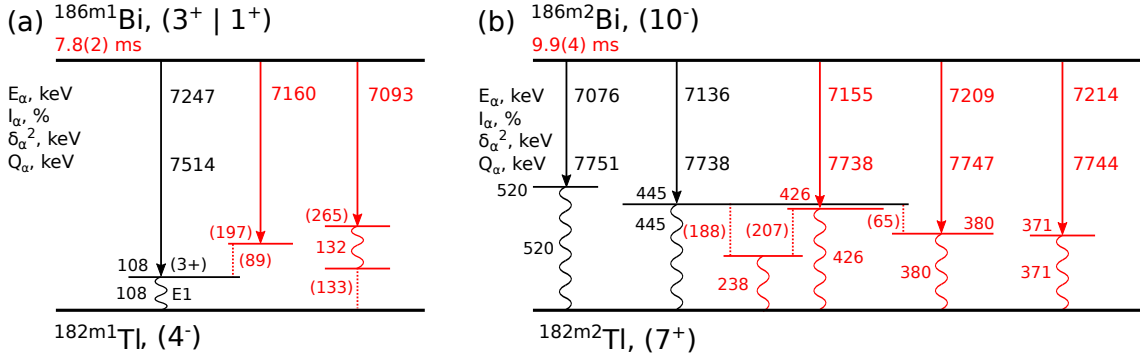


Figure 4.8: Alpha-decay schemes deduced in this work for (a) $^{186m1}\text{Bi}$ and (b) $^{186m2}\text{Bi}$. New/improved data, e.g. γ rays, levels and half-lives are highlighted in red, while known data from [And03a] are in black. The unobserved transitions deduced from the energy differences are shown by dotted lines and the corresponding energies are given in parentheses. All energy values are in keV. The spin-parity value $1^{(+)}$ of $^{186m1}\text{Bi}$ is based on an analogy with the recent assignment of ^{188}Bi [Bar21]. The 3^+ value was tentatively assigned based on the systematics in the heavier bismuth isotopes in Ref. [Bat97]. The thallium low-spin isomer was recently assigned with an $I^\pi=4^-$ [Bar17; Van16]. The contradiction of these newly assigned values and the $E1$ multipolarity of the transition deexciting level fed by the unhindered α decay of $^{186m1}\text{Bi}$ is discussed in Sec. 4.2.2.

one order of magnitude, the E_γ condition allows to avoid any possible contribution from $^{186m2}\text{Bi}$. In the case of $^{186m2}\text{Bi}$, only the α -decay energy condition can be applied, because of the low statistics of the α - γ coincidences attributed to this isomer, see discussion below.

In the re-analysis of data from Exp1, we deduced the same half-lives of both isomers, within the uncertainty, as were reported in the previous study in Ref. [And03a], see the third and the last column in Table 4.6. On the contrary, the half-life values deduced from the Exp2 dataset are significantly lower in both isomers than the literature values, see column 4 in Table 4.6. The reason for this discrepancy remains unclear. The half-life values of $7.8(2)$ ms ($^{186m1}\text{Bi}$) and $9.9(4)$ ms ($^{186m2}\text{Bi}$) deduced from the combined dataset, shown in column 5 in Table 4.6, will be used in this work.

Figure 4.9(a) shows a 2D matrix of α - γ prompt coincidences with a time window of $5\ \mu\text{s}$. An additional condition of $Q_{\alpha,tot}=Q(\alpha)+E_\gamma \leq 7800$ keV, based on the $Q_{\alpha,tot}^{m2}=7745$ keV value discussed below, was applied to construct a spectrum shown in Fig. 4.9(b) as a projection from the α - γ coincidence matrix into the γ -ray energy axis. Several α - γ groups can be clearly distinguished. The most intense group at $7247(10)-108(1)$ keV has the $Q_{\alpha,tot}=Q_\alpha(7247)+E_\gamma(108)=7514(10)$ keV value instead of the previously reported 7530 keV [And03a]. Besides the main peak with

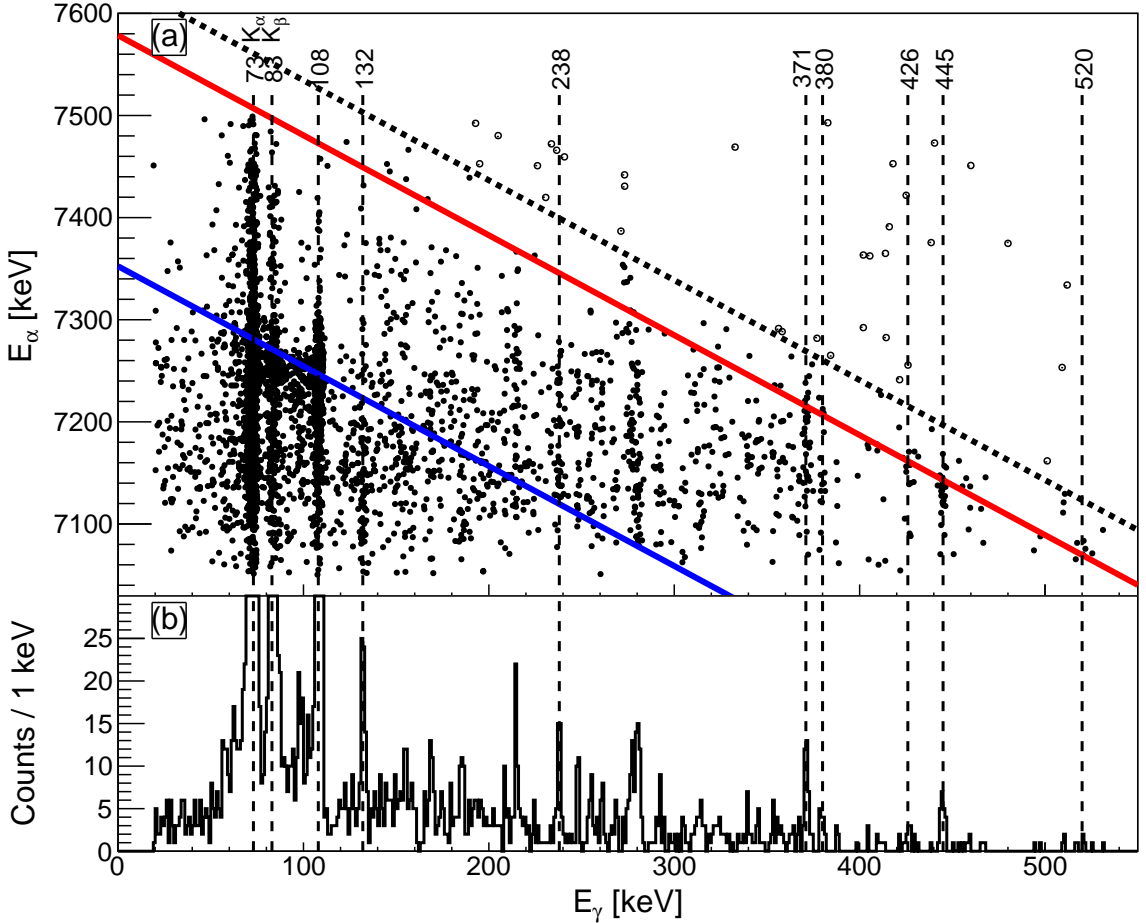


Figure 4.9: (a) α - γ coincidence matrix of events with $\Delta T(\alpha - \gamma) \leq 5 \mu\text{s}$, combined from the Exp1 and Exp2. The blue and red lines denote the total $Q_{\alpha,tot} = Q(\alpha) + E_\gamma$ values of $^{186m^1}\text{Bi}$ ($Q_{\alpha,tot}^{m^1} = 7514(10)$ keV) and $^{186m^2}\text{Bi}$ ($Q_{\alpha,tot}^{m^2} = 7745(11)$ keV), respectively. A black diagonal dashed line denotes $Q_{\alpha,tot} = 7800$ keV value used as a condition in the projection onto the γ -energy axis. (b) The projection into the γ -energy axis for events satisfying the condition $Q_{\alpha,tot} \leq 7800$ keV. The γ lines discussed in the text are denoted with their corresponding energies in keV. We note that the Y-axis scale of the projection was chosen to better show a relevant part with $E_\gamma \gtrsim 120$ keV and does not show the full height of the X-rays and the 108-keV peak.

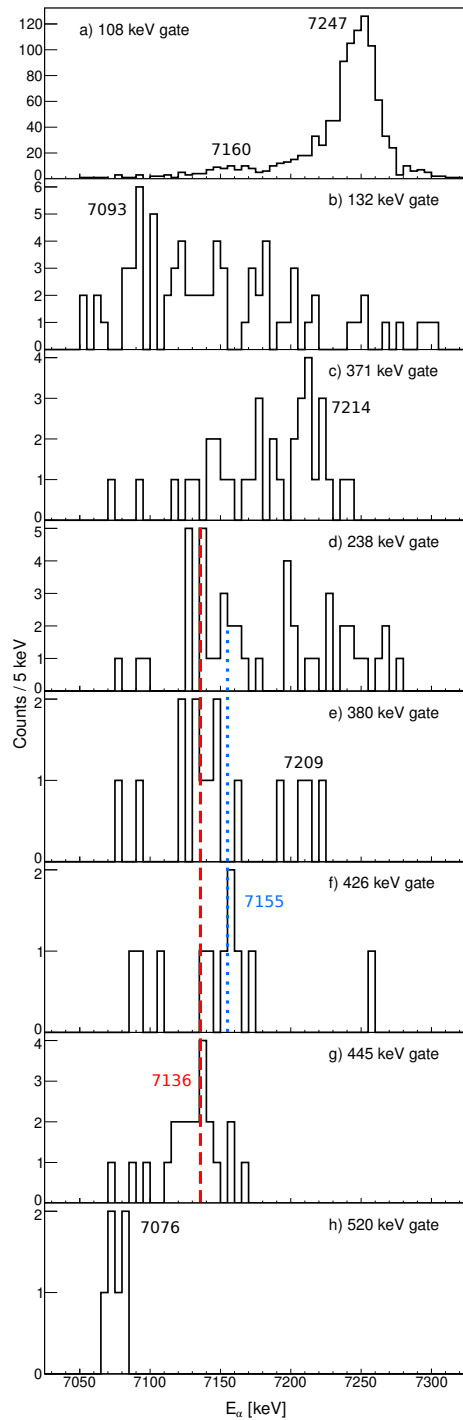


Figure 4.10: Projections of α - γ matrix from Fig. 4.9(a) using the indicated gates on γ -ray energies. The red dashed and blue dotted lines denote 7136- and 7155-keV α -decay energies, respectively.

$E_\alpha=7247\text{ keV}$ a secondary peak at $7160(10)\text{ keV}$ was observed in the α -decay energy projection gated by the 108-keV γ transition, see Fig. 4.10(a). We assign it as an α -decay feeding into a new level at $197(10)\text{ keV}$, deduced from the $Q_{\alpha,tot}^{m1}-Q(7160\text{ keV})$ difference, which should decay via an $89(10)$ -108 keV cascade, to explain the appearance of the $7160\text{-keV } \alpha$ energy in coincidence with the 108-keV transition. However, no such $89(10)$ -keV transition is seen in Fig. 4.9(a), which could be explained by the low intensity of the 7160-keV peak and possibly strong conversion of the low-energy 89-keV transition. Due to this, the $89(10)$ -keV transition is shown as tentative in the decay scheme in Fig. 4.8(a). No evidence for $7160(10)$ - $197(10)\text{ keV } \alpha\text{-}\gamma$ coincidences was observed, either.

The α -decay energy projection gated by the second most intense peak at $E_\gamma=132\text{ keV}$ is shown in Fig. 4.10. A peak with an energy of $7093(11)\text{ keV}$ is apparent in the projection. A tail towards the higher energies is an indication of a large $\alpha+\text{conversion electron (CE)}$ summing in the PSSD, originating from a transition or transitions in a cascade with the 132-keV one. The range of the $\alpha+\text{CE}$ tail corresponds to the $Q_{\alpha,tot}^{m1}$ value, therefore, we tentatively assign this cascade to the $^{186m1}\text{Bi}$ isomer. The difference of the Q_α values of the $^{186m1}\text{Bi}$ isomer and 7093 - 132-keV group indicates a $265(11)\text{-keV}$ level fed by this $7093\text{-keV } \alpha$ decay and deexcited by the transition or transitions in a cascade with the 132-keV γ rays. However, no good candidate for the cascade $133(11)\text{-keV}$ transition was observed in our data, as well as for the direct 265-keV transition, which could be explained by the strong internal conversion of these transitions.

Two one-step $\alpha\text{-}\gamma$ transitions were reported in Ref. [And03a] with γ -ray energies of 445 and 520 keV . The α decays of $^{186m2}\text{Bi}$ feeding these 445 - and 520-keV levels, see Figs. 4.10(g) and 4.10(h), have energies of $7136(11)$ and $7076(11)\text{ keV}$, yielding similar values, within the uncertainty, of $Q_{\alpha,tot}=7744(11)$ and $7751(11)\text{ keV}$, respectively. A weighted average of these values determines the new $Q_{\alpha,tot}^{m2}=7745(11)\text{ keV}$ value of the $^{186m2}\text{Bi}$, in comparison to $7756(15)\text{ keV}$ determined in Ref. [And03a].

Two additional $\alpha\text{-}\gamma$ groups can be attributed to ^{186}Bi based on their $Q_{\alpha,tot}$ values similar to the $Q_{\alpha,tot}^{m2}$. The $\alpha\text{-}\gamma$ groups at $7214(11)$ - $371(1)$ and $7155(11)$ - $426(1)\text{ keV}$, see Figs. 4.10(c), and 4.10(f), have the $Q_{\alpha,tot}$ values of $7744(11)$ and $7738(11)\text{ keV}$, respectively. These values are similar, within uncertainty, to the $Q_{\alpha,tot}^{m2}=7745(11)\text{ keV}$ and thus we interpret these groups as one-step $\alpha\text{-}\gamma$ transitions from the $^{186m2}\text{Bi}$ isomer.

In the α -energy projection gated by the $380\text{-keV } \gamma$ rays in Fig. 4.10(e), two dis-

tinct groups of events are seen—one at 7136(11) keV and the other at 7209(11) keV. The $Q_{\alpha,tot}$ value of the 7209–380-keV α - γ coincidences is 7747(11) keV, which is consistent with the $Q_{\alpha,tot}^{m2}$ value. Furthermore, the lower-energy peak has the same energy as the α decay feeding 445-keV state, which we explain as the feeding of 380-keV level via an unobserved \sim 65-keV transition.

The 238-keV gated projection in Fig. 4.10(d) displays two structures at 7136(11) and 7155(11) keV. Since the 445- and 426-keV levels are populated by the α decays with the same energies, respectively, we tentatively suggest the 238-keV level to be fed by unobserved transitions from both 445- and 426-keV levels.

Decay of the low-spin $^{186m1}\text{Bi}$ isomer

The 3^+ isomers have been systematically observed in the even- A bismuth isotopes with $A \geq 190$ [ENS24]. Analogously to this trend, the low-spin isomer in ^{186}Bi was tentatively assigned as 3^+ in the past [Bat97]. However, as mentioned in Sec. ??, the recent laser spectroscopic study re-interpreted the g.s. of ^{188}Bi as a prolate $1^{(+)}$ state caused by the presumed $\pi 1/2[530] \times \nu 1/2[521]$ configuration [Bar21]. *Not sure about the next part. A structural change was predicted to occur around $N \sim 100$. For example, the intruder $1/2^+$ state in ^{185}Bi decreases in energy and becomes a ground state with $\pi 1h_{9/2} \times s_{1/2}^{-1}$ configuration and prolate deformation [And04]. Naturally, we could expect $^{186m1}\text{Bi}$ to follow this newly-established $I^\pi=1^{(+)}$ value.*

In the case of odd-odd thallium isotopes with $A=184$ –204, a similar trend is established with a systematically occurring low-spin 2^- state understood as being due to $\pi 3s_{1/2} \times \nu 3p_{3/2}$ configuration [Bar17; Rap17; Van91; ENS24]. A change in the structure of lighter thallium isotopes was expected to occur at $N=100$ due to the depletion of the $\nu 1i_{13/2}$ and $\nu 3p_{3/2}$ orbitals. Indeed, recent laser-spectroscopy study at ISOLDE (CERN) established the configuration of $[\pi 3s_{1/2} \times \nu 1h_{9/2}]_{4^-}$ for ^{180}Tl , based on the comparison of experimental and calculated magnetic moments (see Table III in [Bar17] and discussion therein). Due to similar hyperfine structure patterns of ^{180}Tl and a low-spin isomer in ^{182}Tl , the same configuration was suggested for the latter [Bar17].

Another typical feature of the odd-odd bismuth neutron deficient isotopes is the occurrence of unhindered, intense α decay to an excited state in thallium daughter nucleus [Van91; And03b]. In $^{186m1}\text{Bi}$, the 7247-keV α decay feeding the 108-keV level is the most intense transition in the low-spin isomer. Its reduced α decay width calculated using the Rasmussen formalism [Ras59] (assuming $\Delta L=0$ transitions) is

$\delta_\alpha^2=56(4)$ keV. This value is equal to the reduced widths of 54(3) and 55_{-7}^{+20} keV of unhindered $3^+ \rightarrow 3^+$ α -decay transitions in ^{188}Bi and ^{190}Bi [And03b], respectively. Such analogous values suggest a very similar, unhindered nature of these transitions, connecting levels with the same spin-parity. Consequently, the $E1$ multipolarity of the 108-keV transition deduced in the Ref. [And03a] and the $I^\pi=(4^-)$ assignment of $^{182m1}\text{Tl}$ discussed earlier allows either 3^+ or 5^+ spin-parity of the 108-keV level. Both options are in conflict with the assumption that $^{186m1}\text{Bi}$ analogously follows the $I^\pi=1^{(+)}$ value deduced for ^{188}Bi [Bar21], see above. Since the $I^\pi=1^{(+)}$ value for $^{186m1}\text{Bi}$ is deduced only as an analogy with heavier ^{188}Bi , we prefer to suggest (3^+) spin-parity value of the low-spin isomer, based on its systematic occurrence in $A=190\text{--}204$ bismuth even- A isotopes.

In the case of the α decay with $E_\alpha=7255$ keV feeding the 97-keV level the calculated reduced width is 2.8(6) keV, yielding a hindrance factor of around 20 in comparison to the strongest 7247-keV transition. The reduced width of the 7120-keV α decay feeding the suggested 229-keV level (which is deexcited by the cascade of 132-97 keV γ transitions) is 8.7(20) keV, with a hindrance factor of around 7. Such relatively high hindrance factors could suggest a different nature of these transitions, such as connecting states with different spins or configurations.

Decay of the high-spin $^{186m2}\text{Bi}$ isomer

In the heavier $^{188m2}\text{Bi}$ and $^{190m2}\text{Bi}$ isomers the unhindered $10^- \rightarrow 10^-$ α decay leads to an isomeric 10^- state in the daughter thallium nucleus, 500 and 374 keV above the g.s. [And03b], respectively. Such unhindered α -decay transition in both cases was roughly by two orders of magnitude more intense than any other transition from the high-spin isomer and comparable to the intensity of the most intense unhindered transition in the low-spin isomers. In the case of $^{186m2}\text{Bi}$, the difference in intensity between its most intense α -decay transition with $E_\alpha=7142$ keV and the most intense 7247-keV transition in the low-spin isomer is about two orders of magnitude. We did not observe any higher-intensity α -decay transition with a well-defined peak in either single α spectra or in the α - γ coincident matrix. For the latter case, an α - γ group could be invisible either because the γ transition is heavily converted or has a half-life larger than the $\Delta T(\alpha - \gamma) \leq 5\ \mu\text{s}$ condition. For example, the energies of $E3$ transitions between the $10^- \rightarrow 7^+$ states in thallium daughter isotopes follow a parabolic dependence on the mass number (cf. Fig. 7(b) in Ref. [And03a]). An extrapolation to $^{182m2}\text{Tl}$ predicts an analogous transition with an energy of about

680 keV in $^{182m^2}\text{Tl}$. However, such transition with $E3$ multipolarity would be difficult to observe in the α - γ coincidence spectra, due to the $\Delta T(\alpha - \gamma) \leq 5 \mu\text{s}$ condition and its estimated half-life in order of tens of microseconds. On top of that, an α -decay transition feeding such 10^- level with predicted energy of about 6900 keV was not observed in our data either. The non-observation of an intense α -decay transition from $^{186m^2}\text{Bi}$ may indicate a change in its structure, however, we can not draw a solid conclusion based on the present data.

Chapter 5

Summary

5. SUMMARY

Appendices

Appendix A

Excitation functions for radon compound nuclei

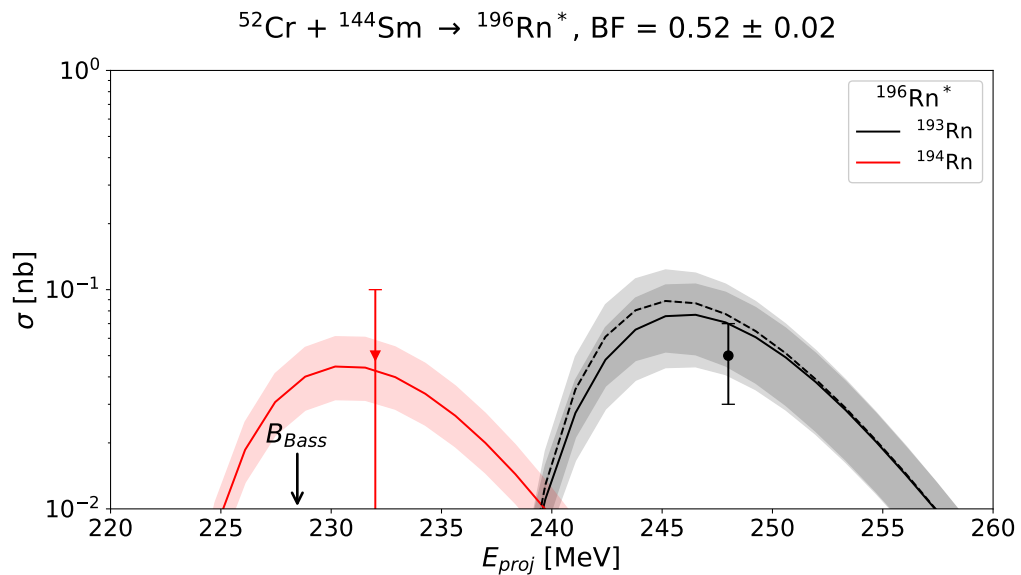


Figure A.1: The experimental (points) and theoretical (lines) excitation functions for the reaction $^{52}\text{Cr} + ^{144}\text{Sm} \rightarrow ^{196}\text{Rn}^*$. The solid lines denote the HIVAP calculations according to the barrier-fluctuations approach, the dashed lines are for the inverted-parabola parametrization, see Sec. 2.1.2. The matching semi-transparent shadow around the lines denotes the calculation with the $\text{BF} \pm 0.02$ parameter. The Bass interaction barrier calculated by Eq. 2.6 is denoted by the black arrow. Experimental cross section data are from Ref. [And06a].

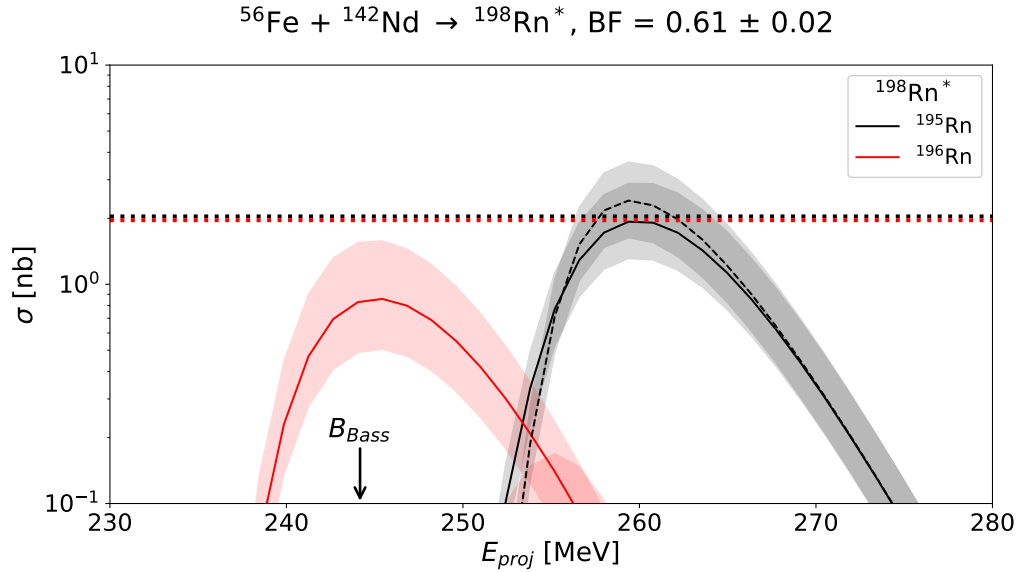


Figure A.2: The same as in Fig. A.1, but for the reaction $^{56}\text{Fe} + ^{142}\text{Nd} \rightarrow ^{198}\text{Rn}^*$. Experimental cross section data are from Ref. [Ket01] and only the maximum cross section values were reported.

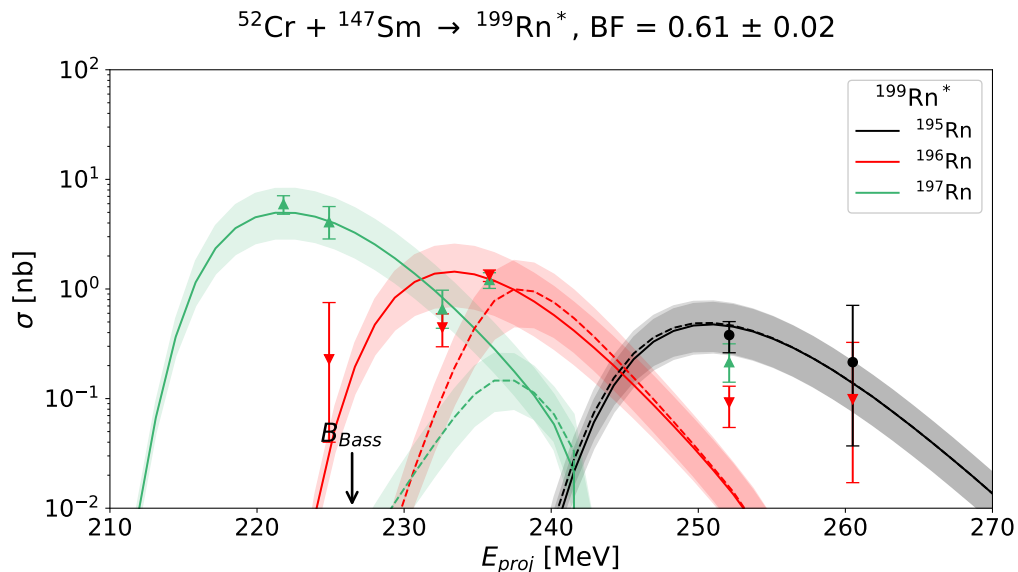


Figure A.3: The same as in Fig. A.1, but for the reaction $^{52}\text{Cr} + ^{147}\text{Sm} \rightarrow ^{199}\text{Rn}^*$. Experimental cross section data were obtained in this work.

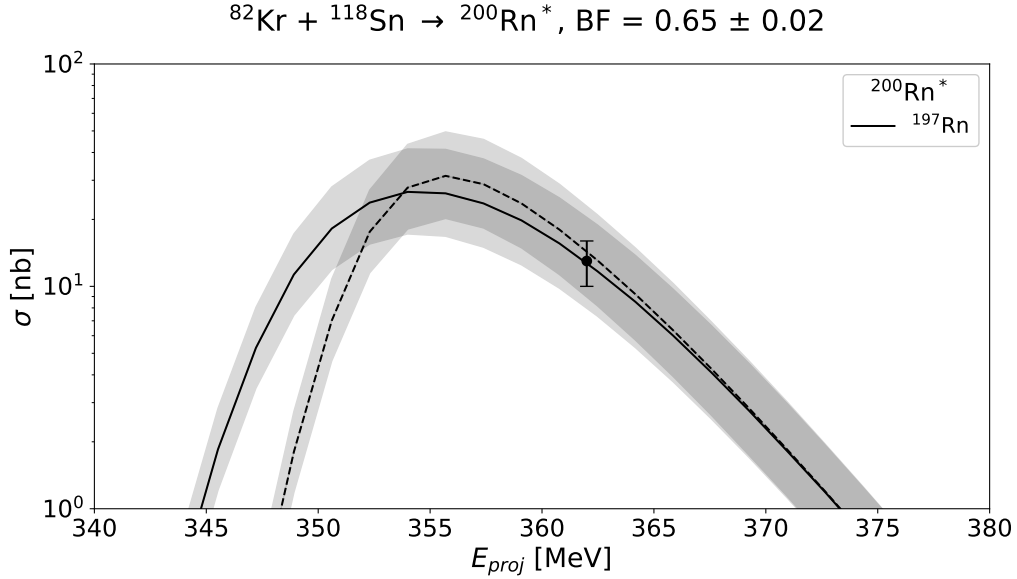


Figure A.4: The same as in Fig. A.1, but for the reaction $^{82}\text{Kr} + ^{118}\text{Sn} \rightarrow ^{200}\text{Rn}^*$. Experimental cross section data are from Ref. [And08].

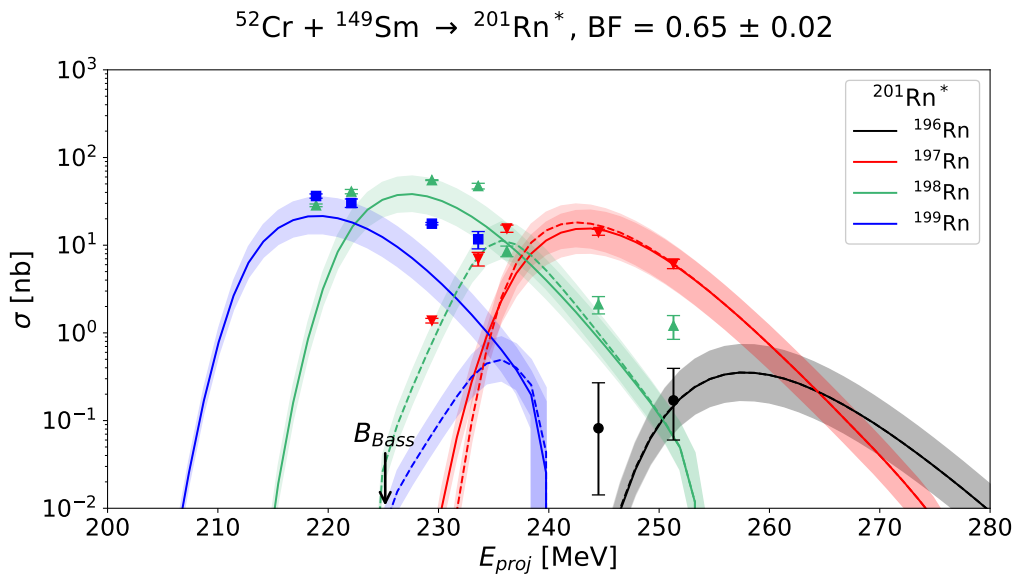


Figure A.5: The same as in Fig. A.1, but for the reaction $^{52}\text{Cr} + ^{149}\text{Sm} \rightarrow ^{201}\text{Rn}^*$. Experimental cross section data were obtained in this work.

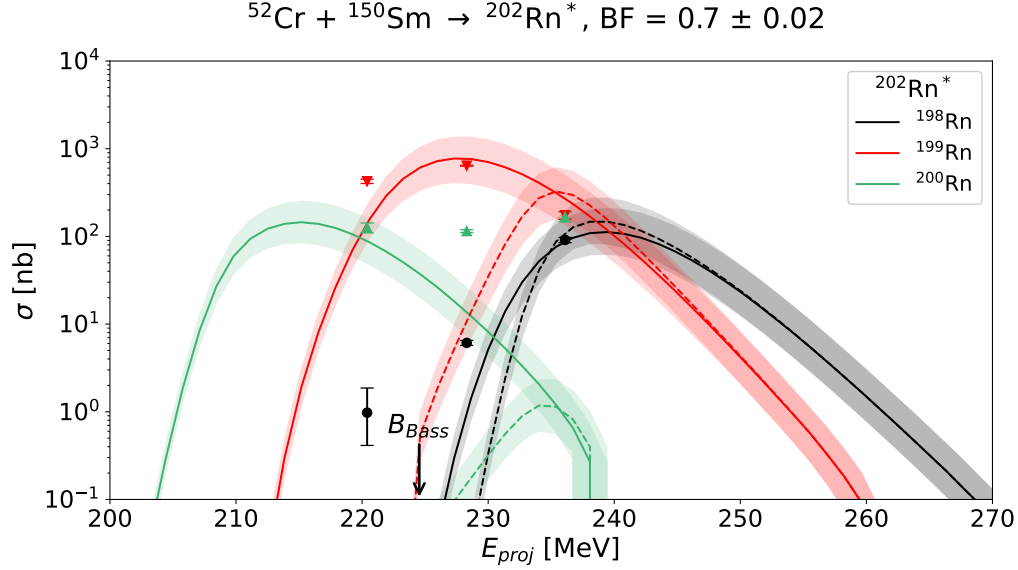


Figure A.6: The same as in Fig. A.1, but for the reaction $^{52}\text{Cr} + ^{150}\text{Sm} \rightarrow ^{202}\text{Rn}^*$. Experimental cross section data were obtained in this work.

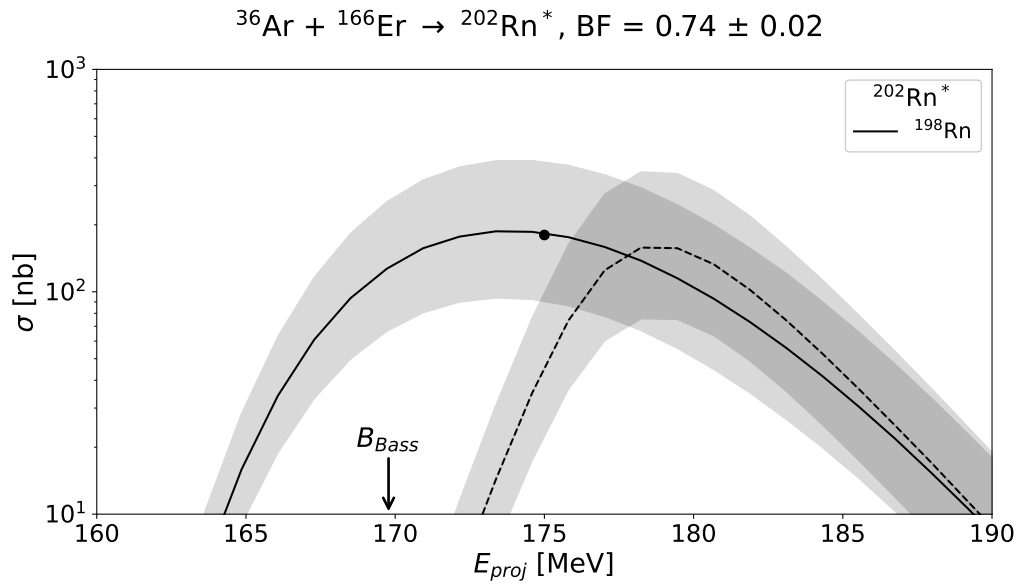


Figure A.7: The same as in Fig. A.1, but for the reaction $^{36}\text{Ar} + ^{166}\text{Er} \rightarrow ^{202}\text{Rn}^*$. Experimental cross section data are from Ref. [Tay99].

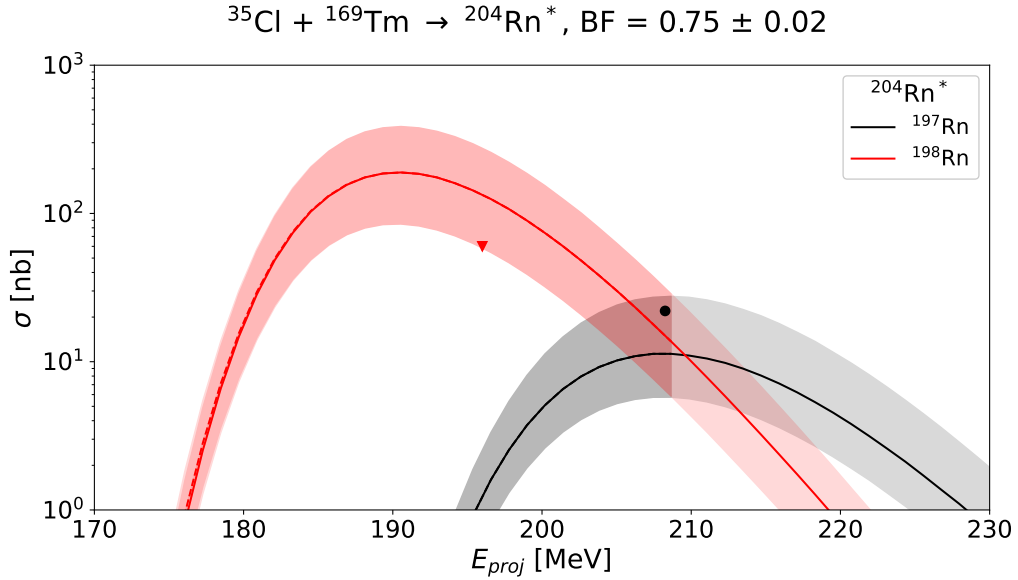


Figure A.8: The same as in Fig. A.1, but for the reaction $^{35}\text{Cl}+^{169}\text{Tm}\rightarrow^{204}\text{Rn}^*$. Experimental cross section data are from Ref. [Enq96].

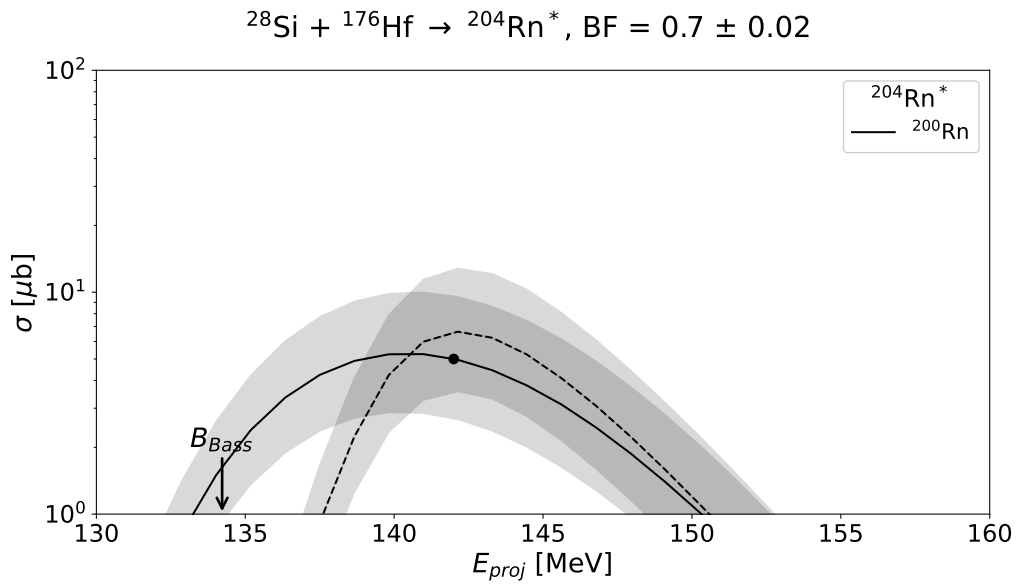


Figure A.9: The same as in Fig. A.1, but for the reaction $^{28}\text{Si}+^{176}\text{Hf}\rightarrow^{204}\text{Rn}^*$. Experimental cross section data are from Ref. [Tay96].

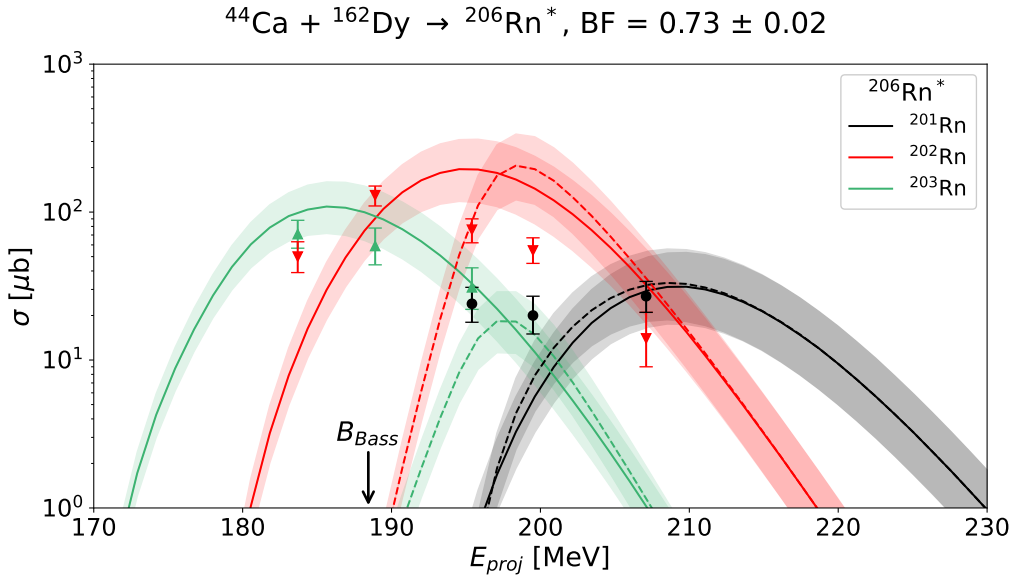


Figure A.10: The same as in Fig. A.1, but for the reaction $^{44}\text{Ca} + ^{162}\text{Dy} \rightarrow ^{206}\text{Rn}^*$. Experimental cross section data are from Ref. [Wer15a].

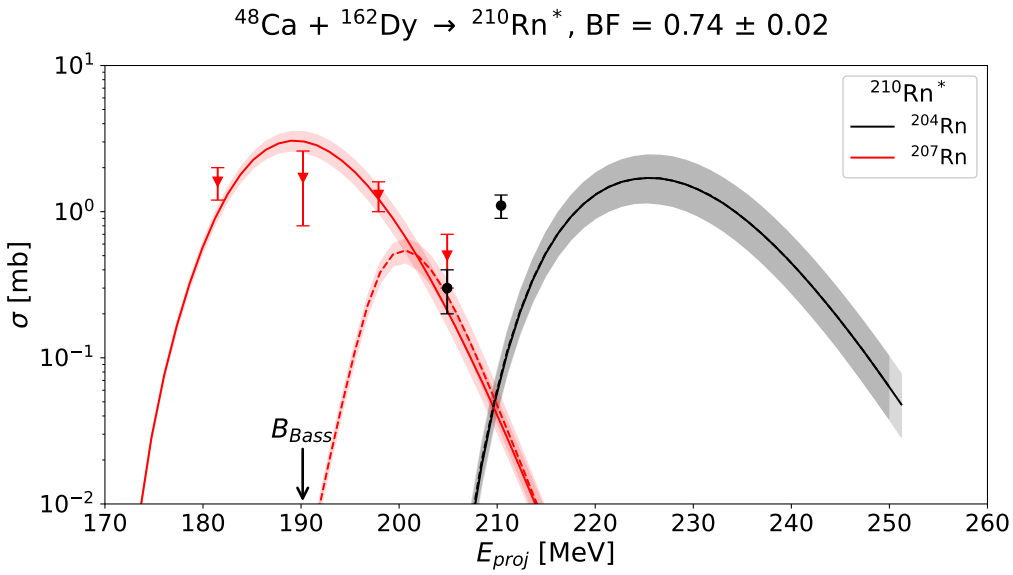


Figure A.11: The same as in Fig. A.1, but for the reaction $^{48}\text{Ca} + ^{162}\text{Dy} \rightarrow ^{210}\text{Rn}^*$. Experimental cross section data are from Ref. [May15].

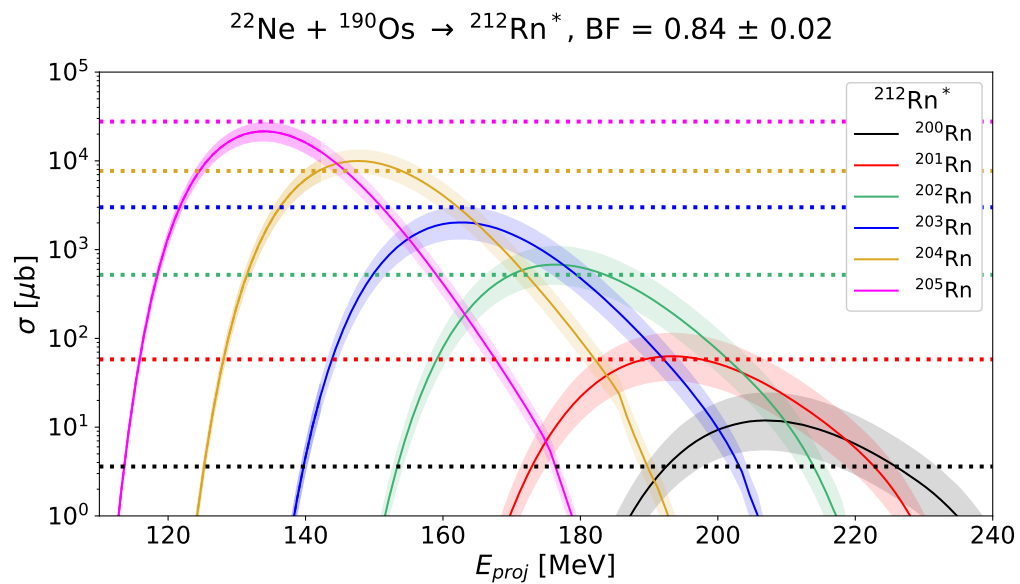


Figure A.12: The same as in Fig. A.1, but for the reaction $^{22}\text{Ne} + ^{190}\text{Os} \rightarrow ^{212}\text{Rn}^*$. Experimental cross section data are from Ref. [Yer03], only the maximum ER cross section values were reported.

A. EXCITATION FUNCTIONS FOR RADON COMPOUND NUCLEI

Appendix B

Excitation functions for astatine compound nuclei

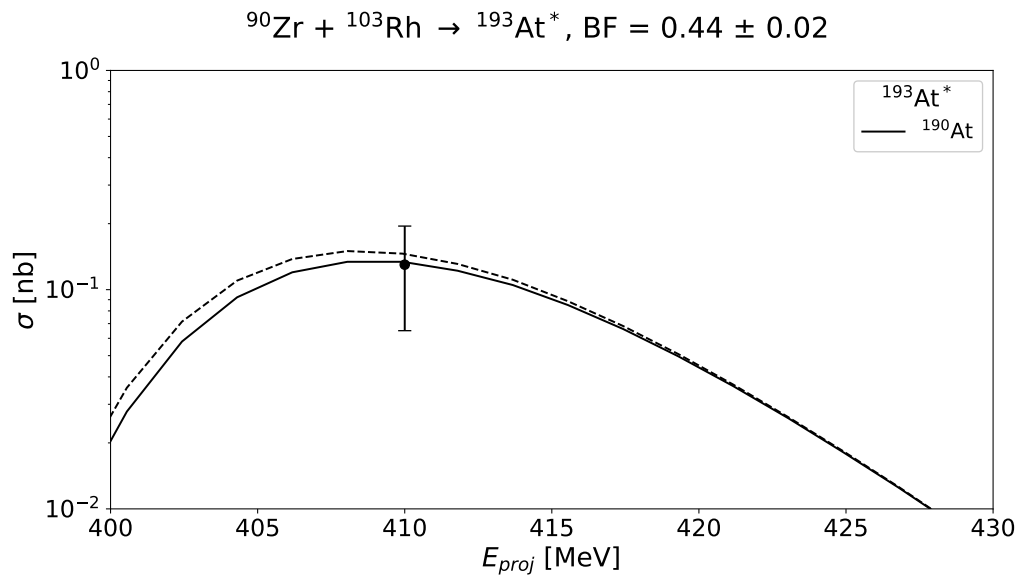


Figure B.1: The same as in Fig. A.1, but for the reaction $^{90}\text{Zr} + ^{103}\text{Rh} \rightarrow ^{193}\text{At}^*$. Experimental cross section data are from Ref. [And23].

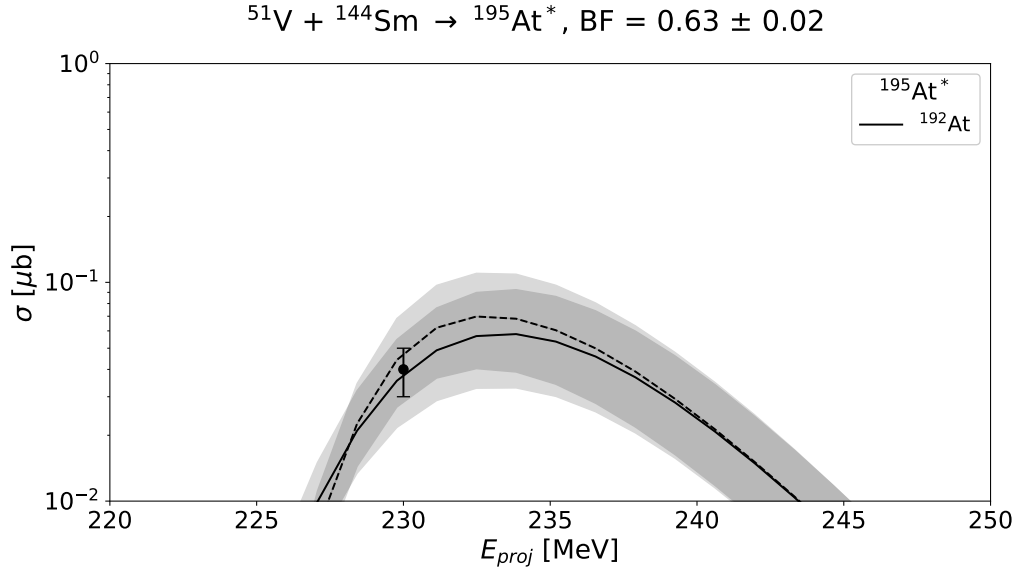


Figure B.2: The same as in Fig. A.1, but for the reaction $^{51}\text{V} + ^{144}\text{Sm} \rightarrow ^{195}\text{At}^*$. Experimental cross section data are from Ref. [And06b].

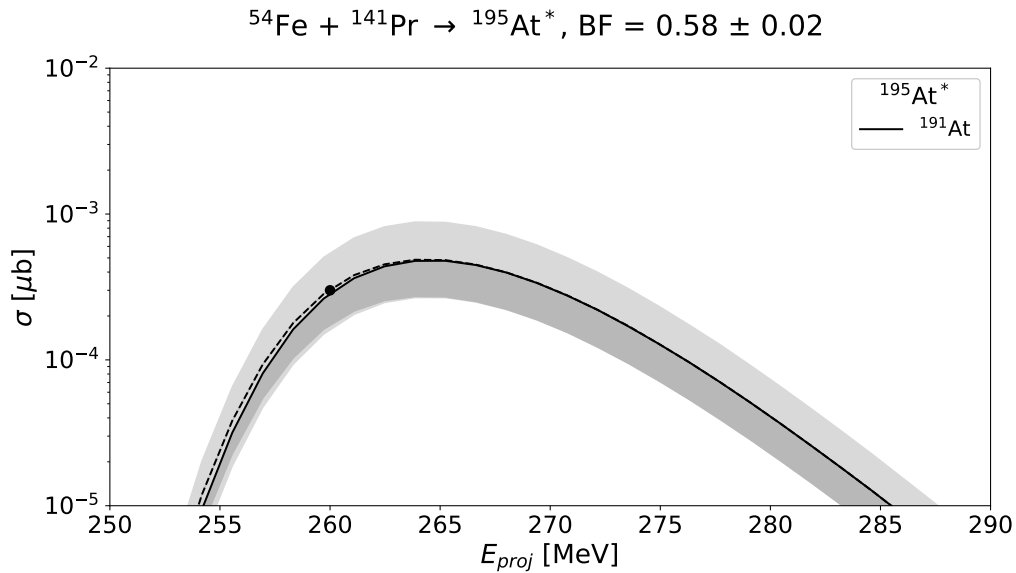


Figure B.3: The same as in Fig. A.1, but for the reaction $^{54}\text{Fe} + ^{141}\text{Pr} \rightarrow ^{195}\text{At}^*$. Experimental cross section data are from Ref. [Ket03a].

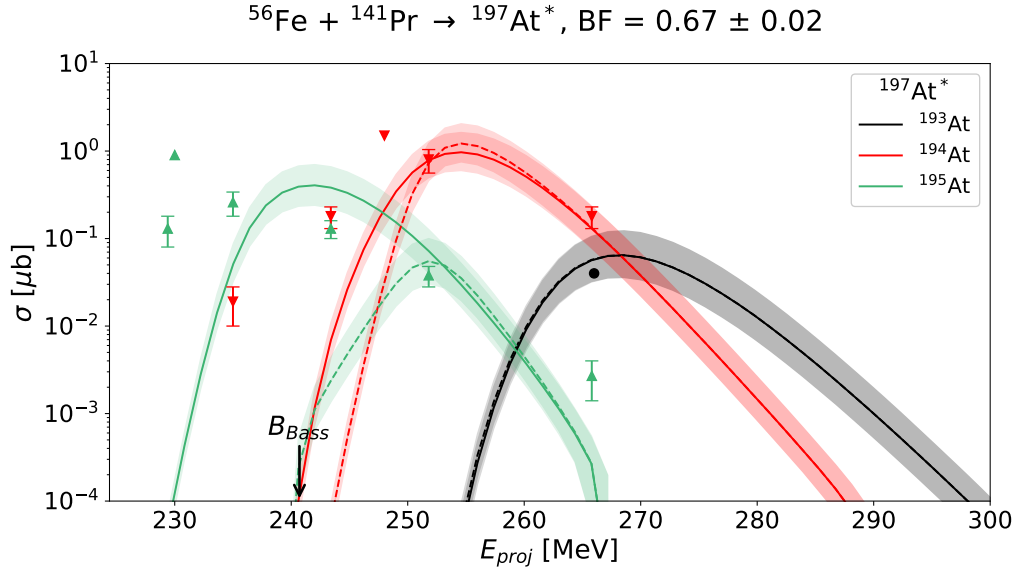


Figure B.4: The same as in Fig. A.1, but for the reaction $^{56}\text{Fe} + ^{141}\text{Pr} \rightarrow ^{197}\text{At}^*$. Experimental cross section data are from Refs. [Ket03b; Ket03a] (without uncertainties) and from Ref. [And16] (with uncertainties).

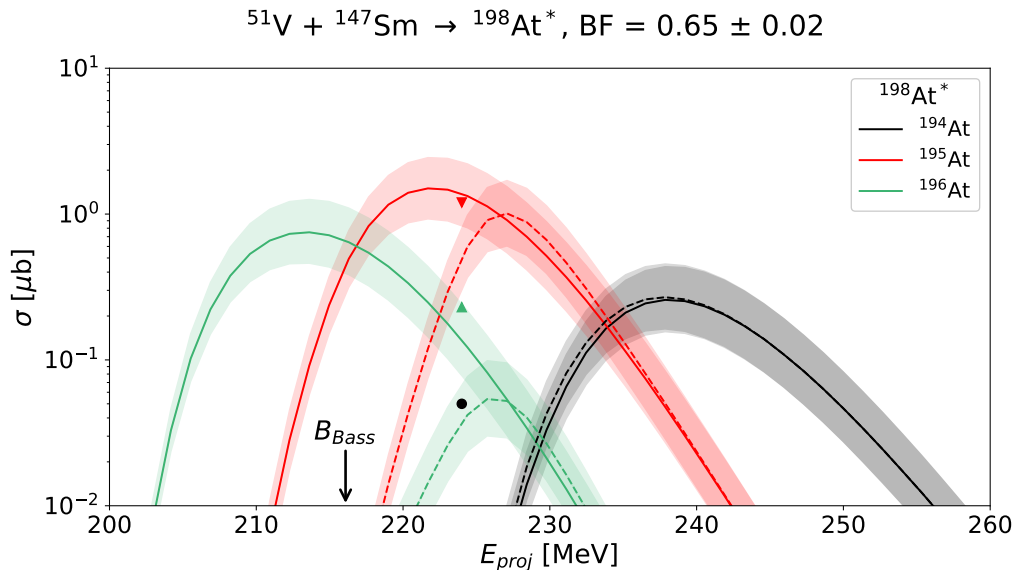


Figure B.5: The same as in Fig. A.1, but for the reaction $^{51}\text{V} + ^{147}\text{Sm} \rightarrow ^{198}\text{At}^*$. Experimental cross section data are from Ref. [Nym13].

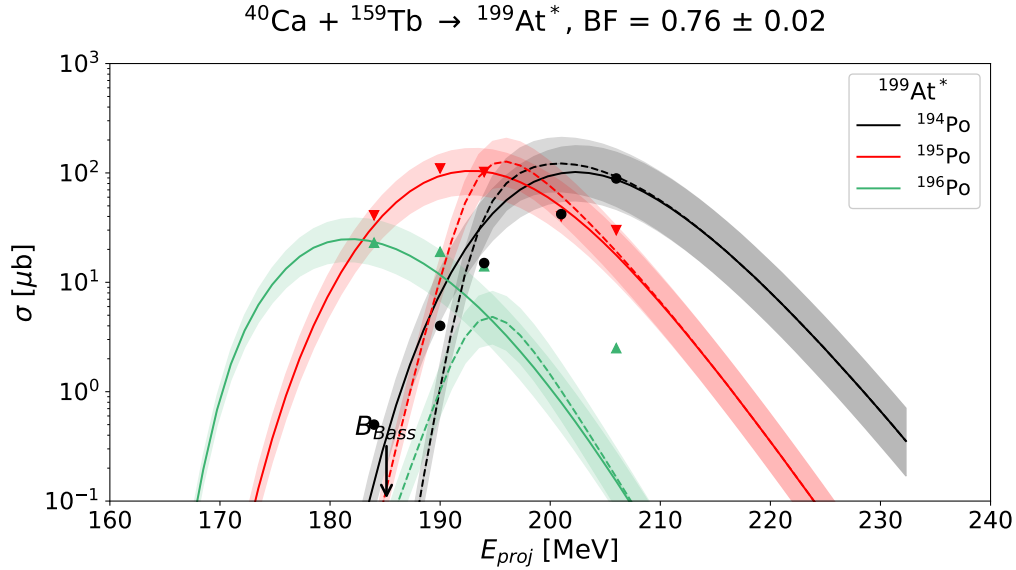


Figure B.6: The same as in Fig. A.1, but for the reaction $^{40}\text{Ca} + ^{159}\text{Tb} \rightarrow ^{199}\text{At}^*$. Experimental cross section data are from Ref. [And90], only cross section values for $p(3-5)n$ evaporation channels were reported.

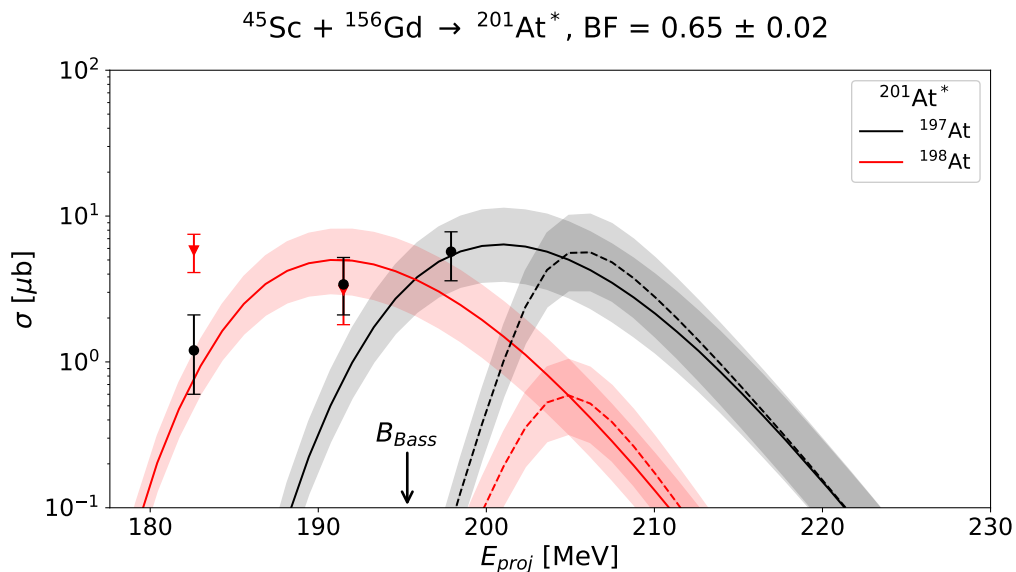


Figure B.7: The same as in Fig. A.1, but for the reaction $^{45}\text{Sc} + ^{156}\text{Gd} \rightarrow ^{201}\text{At}^*$. Experimental cross section data are from Ref. [Wer15c].

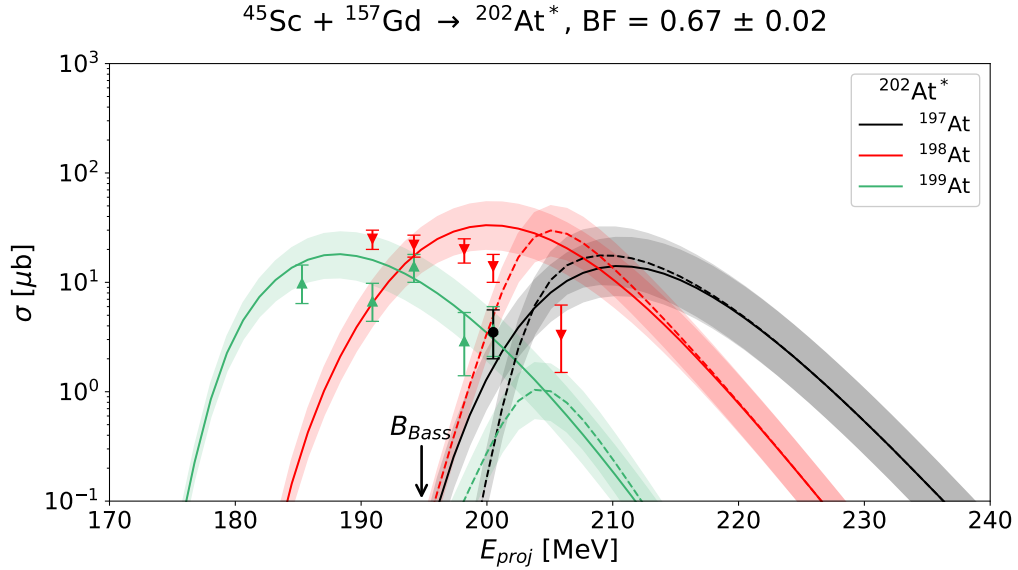


Figure B.8: The same as in Fig. A.1, but for the reaction $^{45}\text{Sc} + ^{157}\text{Gd} \rightarrow ^{202}\text{At}^*$. Experimental cross section data are from Ref. [Wer15c].

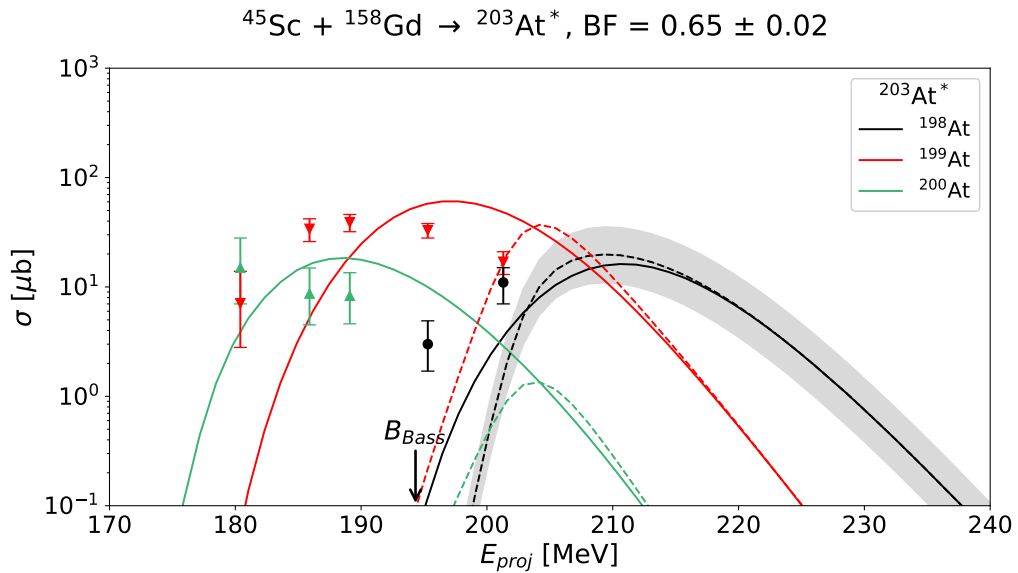


Figure B.9: The same as in Fig. A.1, but for the reaction $^{45}\text{Sc} + ^{158}\text{Gd} \rightarrow ^{203}\text{At}^*$. Experimental cross section data are from Ref. [Wer15c].

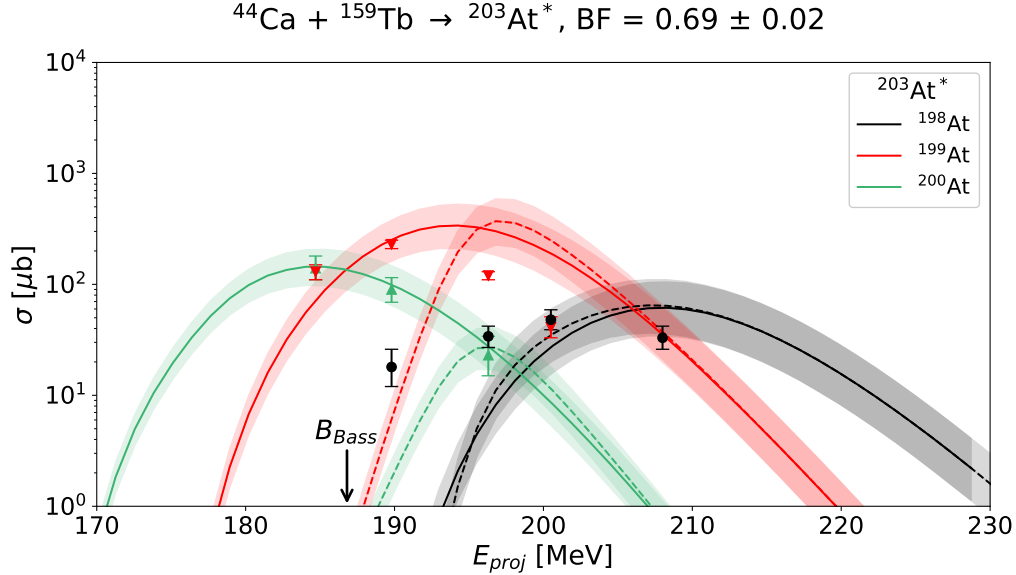


Figure B.10: The same as in Fig. A.1, but for the reaction $^{44}\text{Ca} + ^{159}\text{Tb} \rightarrow ^{203}\text{At}^*$. Experimental cross section data are from Ref. [Wer15b].

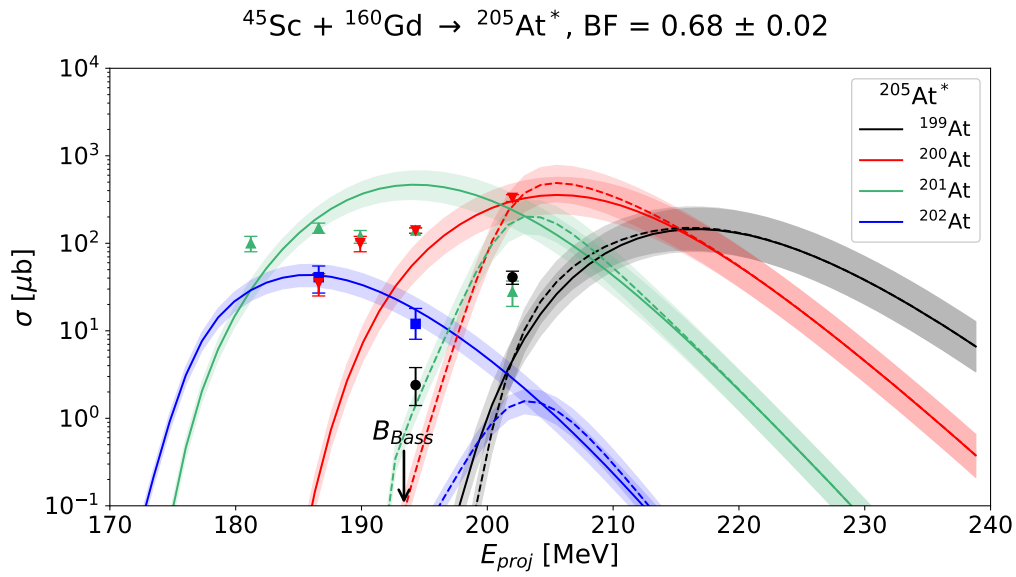


Figure B.11: The same as in Fig. A.1, but for the reaction $^{45}\text{Sc} + ^{160}\text{Gd} \rightarrow ^{205}\text{At}^*$. Experimental cross section data are from Ref. [Wer15c].

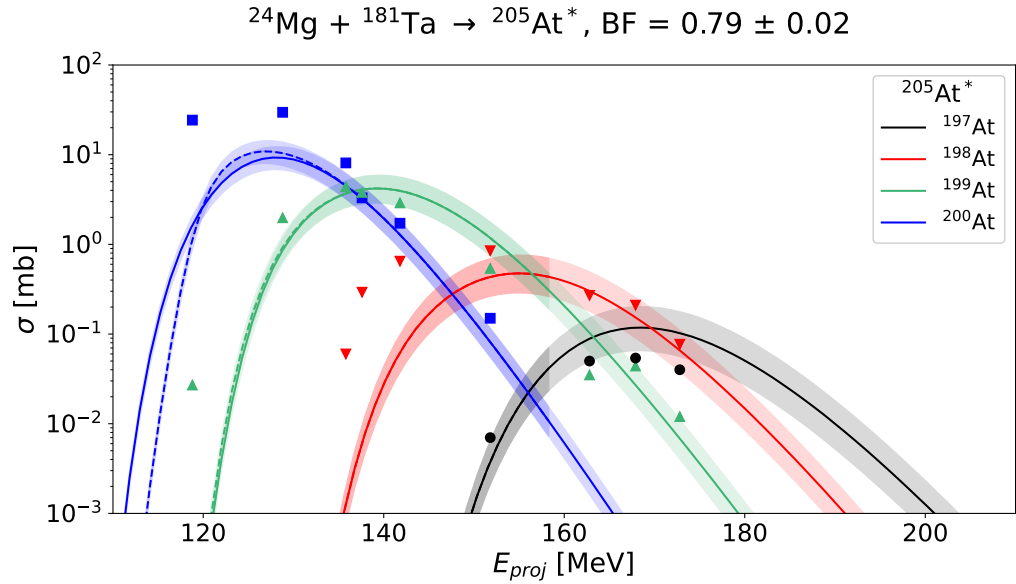


Figure B.12: The same as in Fig. A.1, but for the reaction $^{24}\text{Mg} + ^{181}\text{Ta} \rightarrow ^{205}\text{At}^*$. Experimental cross section data are from Ref. [And90].

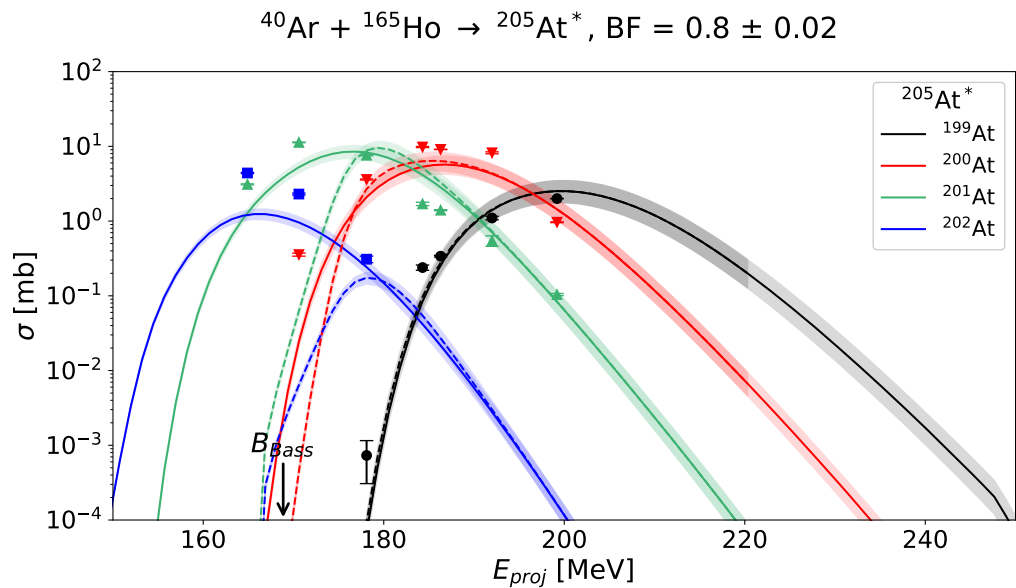


Figure B.13: The same as in Fig. A.1, but for the reaction $^{40}\text{Ar} + ^{165}\text{Ho} \rightarrow ^{205}\text{At}^*$. Experimental cross section data are from Ref. [Ver84].

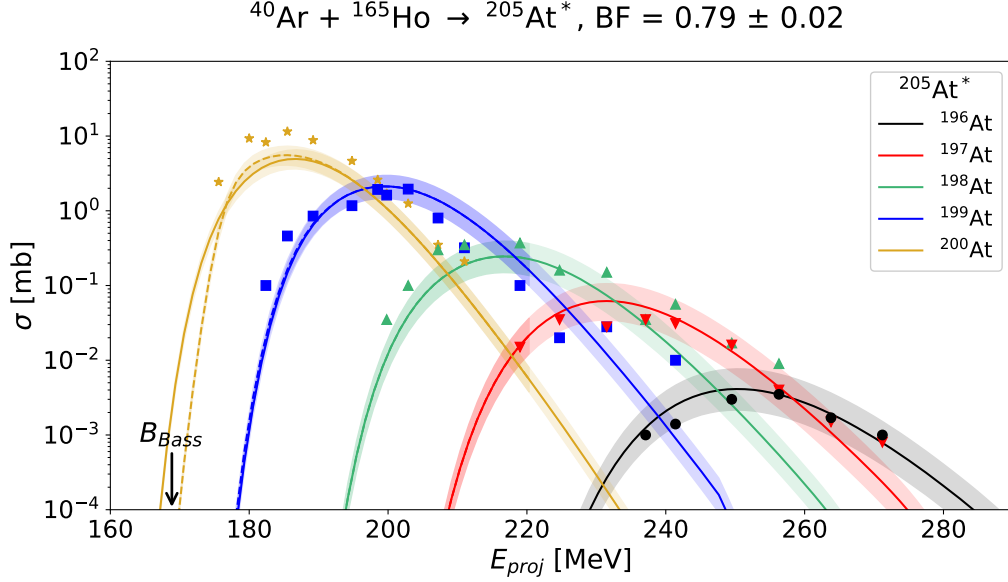


Figure B.14: The same as in Fig. A.1, but for the reaction $^{40}\text{Ar} + ^{165}\text{Ho} \rightarrow ^{205}\text{At}^*$. Experimental cross section data are from Ref. [And90].

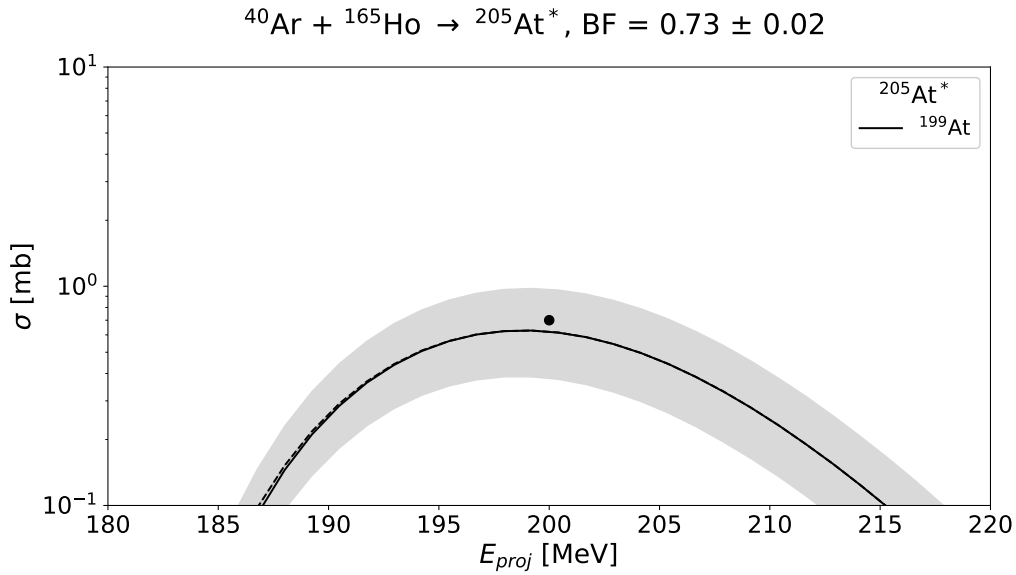


Figure B.15: The same as in Fig. A.1, but for the reaction $^{40}\text{Ar} + ^{165}\text{Ho} \rightarrow ^{205}\text{At}^*$. Experimental cross section data are from Ref. [Jak10].

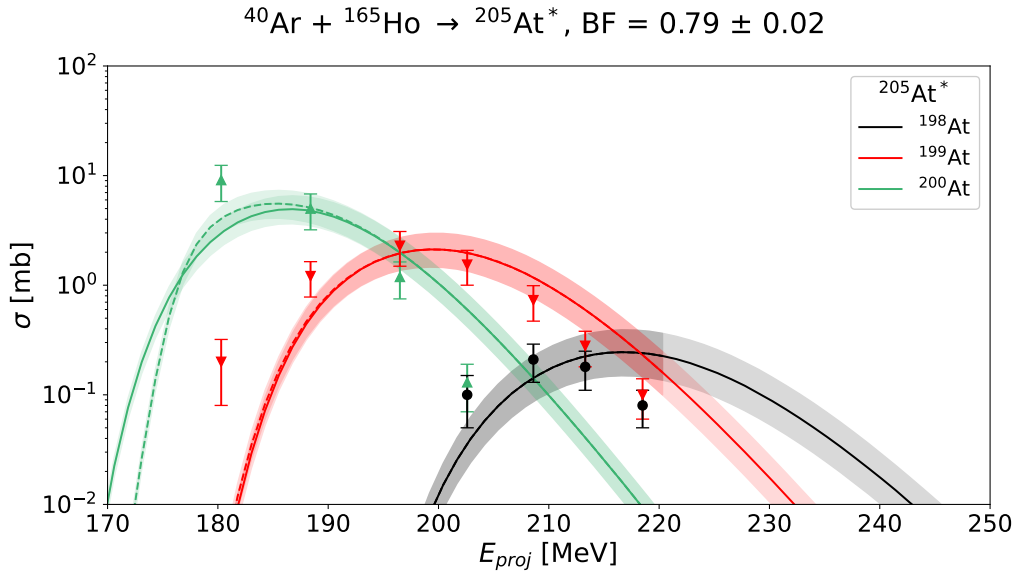


Figure B.16: The same as in Fig. A.1, but for the reaction $^{40}\text{Ar} + ^{165}\text{Ho} \rightarrow ^{205}\text{At}^*$. Experimental cross section data are from Ref. [Fol12].

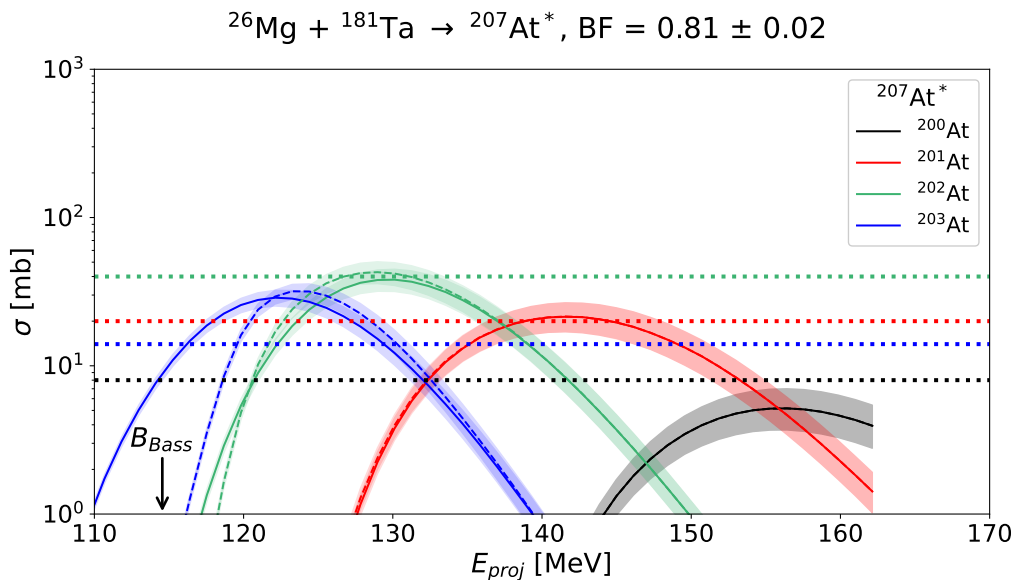


Figure B.17: The same as in Fig. A.1, but for the reaction $^{26}\text{Mg} + ^{181}\text{Ta} \rightarrow ^{207}\text{At}^*$. Experimental cross section data are from Ref. [Yer03], only the maximum ER cross section values were reported.

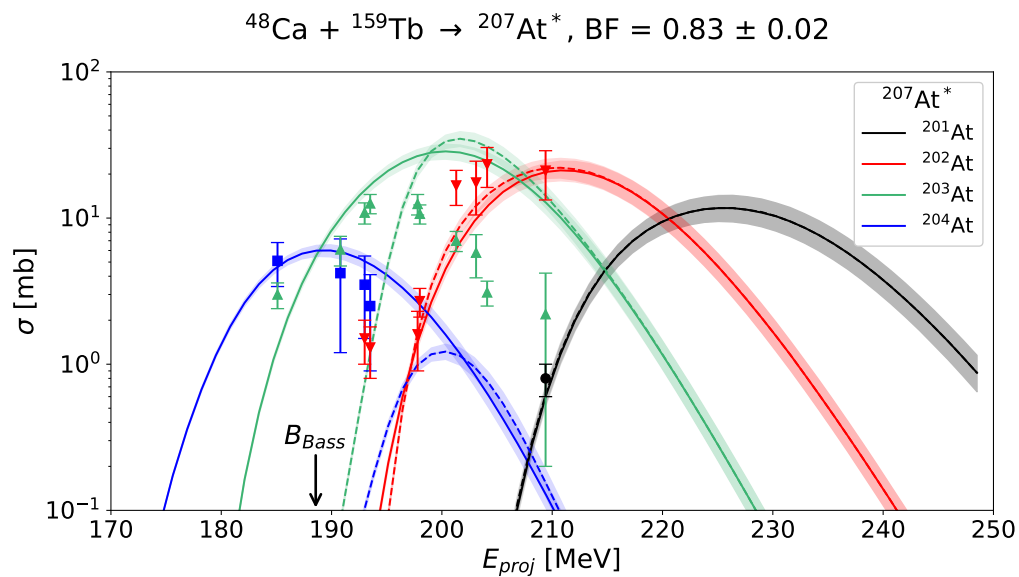


Figure B.18: The same as in Fig. A.1, but for the reaction $^{48}\text{Ca} + ^{159}\text{Tb} \rightarrow ^{207}\text{At}^*$. Experimental cross section data are from Ref. [May14].

Bibliography

- [Ada08] J. Adamczewski-Musch, H. G. Essel, and S. Linev. Tech. rep. GSI Scientific Report, (2008).
- [Ala55] G. Alaga et al. In: *Mat. Fys. Medd. Dan. Vid. Selsk.* 29. (1955).
- [And00] A. N. Andreyev et al. In: *Nature* 405. (2000), p. 430.
DOI: 10.1038/35013012.
- [And02a] A. N. Andreyev et al. In: *Eur. Phys. J. A* 14 (2002), p. 63.
DOI: 10.1140/epja/iepja1387.
- [And02b] A. Andreyev et al. In: *Phys. Rev. C* 66. (2002), p. 014313.
DOI: 10.1103/PhysRevC.66.014313.
- [And03a] A. N. Andreyev et al. In: *Eur. Phys. J. A* 18. (2003), p. 55.
DOI: 10.1140/epja/i2003-10051-1.
- [And03b] A. N. Andreyev et al. In: *Eur. Phys. J. A* 18. (2003), p. 39.
DOI: 10.1140/epja/i2003-10050-2.
- [And04] A. N. Andreyev et al. In: *Phys. Rev. C* 69. (2004), p. 054308.
DOI: 10.1103/PhysRevC.69.054308.
- [And05] A. N. Andreyev et al. In: *Phys. Rev. C* 72. (2005), p. 014612.
DOI: 10.1103/PhysRevC.72.014612.
- [And06a] A. N. Andreyev et al. In: *Phys. Rev. C* 74. (2006), p. 064303.
DOI: 10.1103/PhysRevC.74.064303.
- [And06b] A. N. Andreyev et al. In: *Phys. Rev. C* 73. (2006), p. 024317.
DOI: 10.1103/PhysRevC.73.024317.
- [And08] K. Andgren et al. In: *Phys. Rev. C* 77. (2008), p. 054303.
DOI: 10.1103/PhysRevC.77.054303.

- [And16] B. Andel. "Study of neutron-deficient polonium isotopes". PhD thesis. Comenius University in Bratislava, (2016).
URL: <https://alis.uniba.sk/storage/dpg/dostupne/FM/2016/2016-FM-43897/46176v1.pdf>.
- [And23] A. N. Andreyev et al. In: *Phys. Rev. C* 108. (2023), p. 034303.
DOI: 10.1103/PhysRevC.108.034303.
- [And90] A. N. Andreyev et al. In: *Yadernaya Fizika* 52. (1990).
URL: <https://www.osti.gov/etdeweb/biblio/5443016>.
- [ANL22] ANL. Argonne National Laboratory proposals and LOIs. 2022.
URL: <https://www.phy.anl.gov/atlas/pac/exp10May22.html>.
- [Ant11] S. Antalic et al. In: *Eur. Phys. J. A* 47. (2011), p. 1.
DOI: 10.1140/epja/i2011-11062-y.
- [Bar17] A. E. Barzakh et al. In: *Phys. Rev. C* 95. (2017), p. 014324.
DOI: 10.1103/PhysRevC.95.014324.
- [Bar21] A. Barzakh et al. In: *Phys. Rev. Lett.* 127. (2021), p. 192501.
DOI: 10.1103/PhysRevLett.127.192501.
- [Bas74] R. Bass. In: *Nucl. Phys. A* 231. (1974), p. 45.
DOI: 10.1016/0375-9474(74)90292-9.
- [Bas77] R. Bass. In: *Phys. Rev. Lett.* 39. (1977), p. 265.
DOI: 10.1103/PhysRevLett.39.265.
- [Bas80] R. Bass. In: *Deep-Inelastic and Fusion Reactions with Heavy Ions*. Springer, 1980, p. 281.
DOI: 10.1007/3-540-09965-4_23.
- [Bat97] J. C. Batchelder et al. In: *Z. Phys. A* 357. (1997), p. 121.
DOI: 10.1007/s002180050223.
- [Boh36] N. Bohr. In: *Nature* 137. (1936), p. 344.
DOI: 10.3367/UFNr.0016.193604a.0425.
- [Bru97] R. Brun and F. Rademakers. In: *Nucl. Instrum. Methods A* 389. (1997), p. 81.
DOI: 10.1016/S0168-9002(97)00048-X.
- [Bur51] S. B. Burson et al. In: *Phys. Rev.* 83. (1951), p. 62.
DOI: 10.1103/PhysRev.83.62.

- [Cal84] F. Calaprice et al. In: *Phys. Rev. C* 30. (1984).
DOI: 10.1103/PhysRevC.30.1671.
- [Chu50] T. C. Chu. In: *Phys. Rev.* 79. (1950), p. 582.
DOI: 10.1103/PhysRev.79.582.
- [Coh74] S. Cohen, F. Plasil, and W. J. Swiatecki. In: *Annals of Physics* 82. (1974), p. 557.
DOI: 10.1016/0003-4916(74)90126-2.
- [Dra16] G. D. Dracoulis, P. M. Walker, and F. G. Kondev. In: *Rep. Prog. Phys.* 79. (2016), p. 076301.
DOI: 10.1088/0034-4885/79/7/076301.
- [Enq96] T. Enqvist et al. In: *Z. Phys. A* 354 (1996), p. 9.
DOI: 10.1007/s002180050005.
- [ENS24] ENSDF. Evaluated Nucelar Structure Data File. Accessed on April, 2024.
URL: <https://www.nndc.bnl.gov/ensdf/>.
- [Fir96] R. B. Firestone and V. S. Shirley. “Table of Isotopes, 8th edition”. Wiley, New York, (1996).
- [Fol12] C. M. Folden III et al. In: *Nucl. Instrum. Methods A* 678 (2012), p. 1.
DOI: 10.1016/j.nima.2012.02.035.
- [Fol95] H. Folger et al. In: *Nucl. Instrum. Methods A* 362. (1995), p. 64.
DOI: 10.1016/0168-9002(95)00527-7.
- [Gam28] G. Gamow. In: *Z. Phys.* 51. (1928), p. 204.
DOI: 10.1007/BF01343196.
- [Gei11] H. Geiger and J. M. Nuttall. In: *The London, Edinburgh, and Dublin Philosophical Magazine and Journal of Science* 22. (1911), p. 613.
DOI: 10.1080/14786441008637156.
- [Ghi73] A. Ghiorso et al. In: *Phys. Rev. C* 7. (1973), p. 2032.
DOI: 10.1103/PhysRevC.7.2032.
- [Gho50] S. N. Ghoshal. In: *Phys. Rev.* 80. (1950), p. 939.
DOI: 10.1103/PhysRev.80.939.
- [Gro67] J. R. Grover and J. Gilat. In: *Phys. Rev.* 157. (1967), p. 802.
DOI: 10.1103/PhysRev.157.802.

- [Gur28] R. W. Gurney and E. U. Condon. In: *Nature* 122. (1928), p. 439.
DOI: 10.1038/122439a0.
- [Hag79] E. Hagberg et al. In: *Nucl. Phys. A* 318. (1979), p. 29.
DOI: 10.1016/0375-9474(79)90467-6.
- [Hah21] O. Hahn. In: *Die Naturwissenschaften* 9. (1921), p. 84.
DOI: 10.1007/BF0149132.
- [Heß10] F. P. Heßberger et al. In: *Eur. Phys. J. A* 43. (2010), p. 55.
DOI: 10.1140/epja/i2009-10899-9.
- [Hey83] K. Heyde et al. In: *Phys. Rep.* 102. (1983), p. 291.
DOI: 10.1016/0370-1573(83)90085-6.
- [Hey87] K. Heyde et al. In: *Nucl. Phys. A* 466. (1987), p. 189.
DOI: 10.1016/0375-9474(87)90439-8.
- [Hey88] K. Heyde et al. In: *Nucl. Phys. A* 484. (1988), p. 275.
DOI: 10.1016/0375-9474(88)90073-5.
- [Hil53] D. L. Hill and J. A. Wheeler. In: *Phys. Rev.* 89. (1953), p. 1102.
DOI: 10.1103/PhysRev.89.1102.
- [Hof00] S. Hofmann and G. Münzenberg. In: *Rev. Mod. Phys.* 72. (2000), p. 733.
DOI: 10.1103/RevModPhys.72.733.
- [Hof79] S. Hofmann et al. In: *Z. Phys. A* 291. (1979), p. 53.
DOI: 10.1016/0029-554X(79)90362-8.
- [Hul09] M. Hult et al. In: *Applied Radiation and Isotopes* 67. (2009), p. 918.
DOI: 10.1016/j.apradiso.2009.01.057.
- [Ign75] A. V. Ignatyuk et al. In: *Yad. Fiz.* 21. (1975), p. 1185.
- [Jak10] U. Jakobsson et al. In: *Phys. Rev. C* 82. (2010), p. 044302.
DOI: 10.1103/PhysRevC.82.044302.
- [Kar17] A. V. Karpov et al. In: *Nucl. Instrum. Methods A* 859 (2017), p. 112.
DOI: 10.1016/j.nima.2017.01.069.
- [Kas98] M. Kaspar, J. Gerl, et al. Tech. rep. GSI-98-1, 195, (1998).
URL: <https://repository.gsi.de/record/53534>.
- [Ket01] H. Kettunen et al. In: *Phys. Rev. C* 63. (2001), p. 044315.
DOI: 10.1103/PhysRevC.63.044315.

- [Ket03a] H. Kettunen et al. In: *Eur. Phys. J. A* 17 (2003), p. 537.
DOI: 10.1140/epja/i2002-10162-1.
- [Ket03b] H. Kettunen et al. In: *Eur. Phys. J. A* 16 (2003), p. 457.
DOI: 10.1140/epja/i2002-10130-9.
- [Kib08] T. Kibedi et al. In: *Nucl. Instrum. Methods A* 589. (2008), p. 202.
DOI: 10.1016/j.nima.2008.02.051.
- [Kin03] B. Kindler et al. In: *AIP Conf. Proc.* 680. American Institute of Physics. 2003, p. 781.
DOI: 10.1063/1.1619828.
- [Kin06] B. Kindler et al. In: *Nucl. Instrum. Methods A* 561. (2006), p. 107.
DOI: 10.1016/j.nima.2005.12.232.
- [Kra88] K. S. Krane. “Introductory nuclear physics”. John Wiley & Sons, (1988).
- [Kug00] E. Kugler. In: *Hyperfine interactions* 129. (2000), p. 23.
DOI: 10.1023/A:1012603025802.
- [Kuz67a] V. I. Kuznetsov, N. K. Skobelev, and G. N. Flerov. In: *Sov. J. Nucl. Phys* 4. (1967), p. 202.
- [Kuz67b] V. I. Kuznetsov, N. K. Skobelev, and G. N. Flerov. In: *Sov. J. Nucl. Phys* 5 (1967), p. 191.
- [Lan13] J. Lane et al. In: *Phys. Rev. C* 87. (2013), p. 014318.
DOI: 10.1103/PhysRevC.87.014318.
- [Lom02] B. Lommel et al. In: *Nucl. Instrum. Methods A* 480. (2002), p. 16.
DOI: 10.1016/S0168-9002(01)02041-1.
- [Lov06] W. D. Loveland, D. J. Morrissey, and G. T. Seaborg. “Modern Nuclear Chemistry.” John Wiley & Sons, (2006).
- [Mar79] D. Marx et al. In: *Nucl. Instrum. Methods* 163. (1979), p. 15.
DOI: 10.1016/0029-554X(79)90028-4.
- [May14] D. A. Mayorov et al. In: *Phys. Rev. C* 90. (2014), p. 024602.
DOI: 10.1103/PhysRevC.90.024602.
- [May15] D. A. Mayorov et al. In: *Phys. Rev. C* 92. (2015), p. 054601.
DOI: 10.1103/PhysRevC.92.054601.
- [Maz08] M. Mazzocco et al. In: *Nucl. Instrum. Methods B* 266. (2008), p. 3467.
DOI: 10.1016/j.nimb.2008.04.017.

- [Möl16] P. Möller et al. In: *At. Data. Nucl. Data Tables* 109 (2016), p. 1.
DOI: 10.1016/j.adt.2015.10.002.
- [Mor56] H. Morinaga. In: *Phys. Rev.* 101. (1956), p. 254.
DOI: 10.1103/PhysRev.101.254.
- [Mos20] P. Mosat et al. In: *Phys. Rev. C* 101. (2020), p. 034310.
DOI: 10.1103/PhysRevC.101.034310.
- [Mün79] G. Münzenberg et al. In: *Nucl. Instrum. Methods* 161. (1979), p. 65.
DOI: 10.1016/0029-554X(79)90362-8.
- [Nym13] M. Nyman et al. In: *Phys. Rev. C* 88. (2013), p. 054320.
DOI: 10.1103/PhysRevC.88.054320.
- [Poe06] D. N. Poenaru, I.-H. Plonski, and W. Greiner. In: *Phys. Rev. C* 74. (2006).
DOI: 10.1103/PhysRevC.74.014312.
- [Poe80] D. N. Poenaru, M. Ivascu, and D. Mazilu. In: *Journal de Physique Lettres* 41. (1980), p. 589.
DOI: 10.1051/jphyslet:019800041024058900.
- [Pol62] S. M. Polikanov et al. In: *Sov. Phys. – JETP* 15. (1962), p. 1016.
- [Pop97] A. G. Popeko et al. In: *Nucl. Instrum. Methods B* 126. (1997), p. 294.
DOI: 10.1016/S0168-583X(96)01094-4.
- [Pop99] A. G. Popeko et al. In: *Nucl. Instrum. Methods A* 427. (1999), p. 166.
DOI: 10.1016/S0168-9002(98)01561-7.
- [Qi09] C. Qi et al. In: *Phys. Rev. C* 80. (2009).
DOI: 10.1103/PhysRevC.80.044326.
- [Qui93] A. B. Quint et al. In: *Z. Phys. A* 346. (1993), p. 119.
DOI: 10.1007/BF01294627.
- [Rac43] G. Racah. In: *Phys. Rev.* 63. (1943), p. 367.
DOI: 10.1103/PhysRev.63.367.
- [Rap17] E. Rapisarda et al. In: *J. Phys. G* 44. (2017), p. 074001.
DOI: 10.1088/1361-6471/aa6bb6.
- [Ras59] J. O. Rasmussen. In: *Phys. Rev.* 113. (1959), p. 1593.
DOI: 10.1103/PhysRev.113.1593.

- [Rei81] W. Reisdorf. In: *Z. Phys. A* 300. (1981), p. 227.
DOI: 10.1007/BF01412298.
- [Rei85] W. Reisdorf et al. In: *Nucl. Phys. A* 438. (1985), p. 212.
DOI: 10.1016/0375-9474(85)90125-3.
- [Rei90] W. Reisdorf. HIVAP manual. Unpublished, (1990).
- [Rei92] W. Reisdorf and M. Schädel. In: *Z. Phys. A* 343. (1992), p. 47.
DOI: 10.1007/BF01291597.
- [Rie13] R. du Rietz et al. In: *Phys. Rev. C* 88. (2013), p. 054618.
DOI: 10.1103/PhysRevC.88.054618.
- [Rut11] E. Rutherford. In: *The London, Edinburgh, and Dublin Philosophical Magazine and Journal of Science* 21. (1911), p. 669.
DOI: 10.1080/14786440508637080.
- [Šár96] Š. Šáro et al. In: *Nucl. Instrum. Methods A* 381. (1996), p. 520.
DOI: 10.1016/S0168-9002(96)00651-1.
- [Sch84a] K.-H. Schmidt et al. In: *Z. Phys. A* 316. (1984), p. 19.
DOI: 10.1007/BF01415656.
- [Sch84b] J. R. H. Schneider. Tech. rep. Unpublished, GSI-84-3, (1984).
- [Sie16] M. Siegbahn. In: *Nature* 96. (1916), p. 676.
- [Sod17] F. Soddy. In: *Nature* 99. (1917), p. 244.
DOI: 10.1038/099244c0.
- [Štr06] B. Štreicher. “Synthesis and spectroscopic properties of transfermium isotopes with $Z = 105, 106$ and 107 ”. PhD thesis. FMFI UK, (2006).
- [Tan23] I. Tanihata, H. Toki, and T. Kajino. “Handbook of Nuclear Physics”. Springer Singapore, (2023).
- [Tar08] O. B. Tarasov and D. Bazin. In: *Nucl. Instrum. Methods B* 266. (2008), p. 4657.
DOI: 10.1016/j.nimb.2008.05.110.
- [Tay96] R. B. E. Taylor et al. In: *Phys. Rev. C* 54. (1996), p. 2926.
DOI: 10.1103/PhysRevC.54.2926.
- [Tay99] R. B. E. Taylor et al. In: *Phys. Rev. C* 59. (1999), p. 673.
DOI: 10.1103/PhysRevC.59.673.

- [Uus05] J. Uusitalo et al. In: *Phys. Rev. C* 71. (2005), p. 024306.
DOI: 10.1103/PhysRevC.71.024306.
- [Van02] K. Van de Vel et al. In: *Phys. Rev. C* 65. (2002), p. 064301.
DOI: 10.1103/PhysRevC.65.064301.
- [Van16] C. Van Beveren et al. In: *J. Phys. G* 43. (2016), p. 025102.
DOI: 10.1088/0954-3899/43/2/025102.
- [Van91] P. Van Duppen et al. In: *Nucl. Phys. A* 529. (1991), p. 268.
DOI: 10.1016/0375-9474(91)90796-9.
- [Vaz81] L. C. Vaz, J. M. Alexander, and G. R. Satchler. In: *Phys. Rep.* 69. (1981), p. 373.
DOI: 10.1016/0370-1573(81)90094-6.
- [Ver84] D. Vermeulen et al. In: *Z. Phys. A* 318 (1984), p. 157.
DOI: 10.1007/BF01413464.
- [Wal20] P. Walker and Z. Podolyak. In: *Phys. Scr.* 95. (2020), p. 044004.
DOI: 10.1088/1402-4896/ab635d.
- [Wan12] M. Wang et al. In: *Chinese physics C* 36. (2012), p. 1603.
DOI: 10.1088/1674-1137/36/12/003.
- [Wau93] J. Wauters et al. In: *Physical Review C* 47. (1993), p. 1447.
DOI: 10.1103/PhysRevC.47.1447.
- [Wei36] C. F. Weizsäcker. In: *Naturwissenschaften* 24. (1936), p. 813.
DOI: 10.1007/BF01497732.
- [Wei40] V. F. Weisskopf and D. H. Ewing. In: *Phys. Rev.* 57. (1940), p. 472.
DOI: 10.1103/PhysRev.57.472.
- [Wei51] V. F. Weisskopf. In: *Phys. Rev.* 83. (1951), p. 1073.
DOI: 10.1103/PhysRev.83.1073.
- [Wer15a] T. A. Werke et al. In: *Phys. Rev. C* 92. (2015), p. 054617.
DOI: 10.1103/PhysRevC.92.054617.
- [Wer15b] T. A. Werke et al. In: *Phys. Rev. C* 92. (2015), p. 054617.
DOI: 10.1103/PhysRevC.92.054617.
- [Wer15c] T. A. Werke et al. In: *Phys. Rev. C* 92. (2015), p. 034613.
DOI: 10.1103/PhysRevC.92.034613.

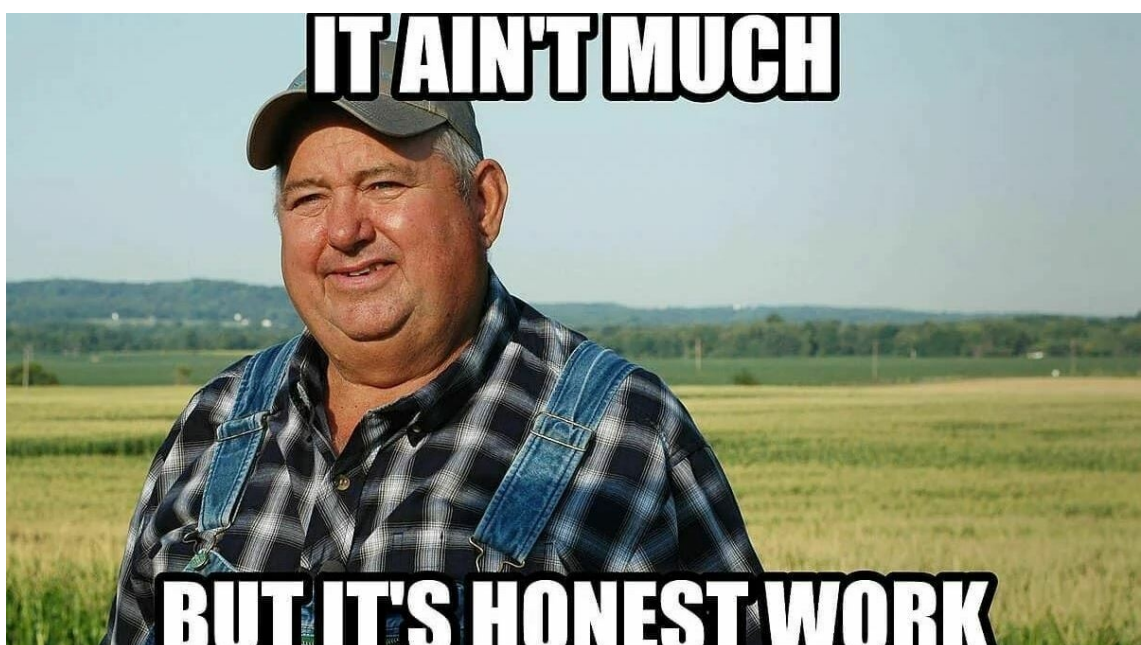
- [Woo92] J. L. Wood et al. In: *Phys. Rep.* 215. (1992), p. 101.
DOI: 10.1016/0370-1573(92)90095-H.
- [Yer03] A. V. Yeremin et al. In: *Physics of Atomic Nuclei* 66 (2003), p. 1042.
DOI: 10.1134/1.1586416.

List of publications

Publications in current contents:

- *α decay of the neutron-deficient isotope ^{190}At*

A. N. Andreyev, D. Seweryniak, B. Andel, S. Antalic, D. T. Doherty, A. Korichi, C. Barton, L. Canete, M. P. Carpenter, R. M. Clark, P. A. Copp, J. G. Cubiss, J. Heery, Y. Hrabar, H. Huang, T. Huang, V. Karayonchev, F. G. Kondev, T. Lauritsen, Z. Liu, G. Lotay, C. Müller-Gatermann, S. Nandi, C. Page, D. H. Potterveld, P. H. Regan, W. Reviol, D. Rudolph, M. Siciliano, R. S. Sidhu, A. Sitarčík, P. J. Woods, Z. Yue, and W. Zhang
Phys. Rev. C 108, 034303
DOI: 10.1103/PhysRevC.108.034303



5.1 TO DO

- Description of experiments at SHIP where Rn* data were collected, with table of exp. details (runtime, intensities, energies etc.)
- Specification of methods used (Re-Al-Al correlations) and their conditions, some challenges (such as close alpha decay energies/half-lives), uncertainties (statistical, SHIP's transmission...), what is the biggest contributor to uncertainty/background etc.
- Afterwards, show the results from SHIP reactions, for each reaction separately, show Re-Al-Al spectra (matrices). Then, show excitation functions with HIVAP calculations and a short discussion, about e.g. problems, accuracy etc. Summarize cross sections in a table. In the table, show also half-lives and α decay energies of the determined ERs, so it will be easier to refer to it (then, maybe put the table earlier in the section, so it is more "accessible"?).
- Description of data from AGFA (192, 193At*), what were the challenges, expectations etc. cite the proposal and the PRC paper. Maybe mention here also Hao's 182,183Bi paper?
- Then proceed with literature data - description of data from the literature for Rn* and At*, where they were measured, what is the "reliability" of data etc.
- HIVAP calculations: the figs with cross section data and corresponding HIVAPs will probably go into APPENDIX, since there are lots of them. Discuss the reliability of HIVAPs here, especially for literature data (analysed radons discussed separately), how were the BARFACs determined, what is the uncertainty, how well they reproduce exp. data etc.
- Afterwards, shortly discuss fission-barriers (compare different models), mention that the scaling is well-known from other experiments (for example, Andrei's cross section paper, or Veselsky's recent one <https://doi.org/10.1103/PhysRevC.109.014618>).
- Proceed to the deduced scaling systematics, how it compares to Bi/Po Andrei's one. Discuss potential effects of quasi fission on the lightest isotopes, show the QF systematics from du Rietz' paper (ofc, for reactions studied here), maybe link to Bi CNs and Hao's "unobservation" of 182,183Bi.

- If done, compare $^{210}\text{Rn}^*$ data from SHIP and deduced BF to Veselsky's values.
- An outlook about the future of production of very neutron-deficient isotopes, (a)symmetric reactions, quasi fission hindering, experimental challenges, new/more precise/reliable models for cross section calculations (NRV, coupled channels etc.) [description, if barrier-scaling can be a factor there as well, complexity, easy-to-use etc.] in comparison to HIVAP - an example could be shown between some reaction. I'll probably move this to Conclusion and Outlook at the end.

5.2 Decay spectroscopy of ^{186}Bi

5.2.1 Experimental details

Describe both experiments, give details in the table (probably the same as in paper), what were some problems (e.g. differences between PSSD calibrations, how they were resolved, Ge calib. in Exp1 etc). Maybe this should be summarized in the previous chapter? Then, I should move also exp. details for cross-section stuff to exp. section?

5.2.2 Results and discussion

In results show spectra, the same as in paper - Re-Al, discuss why there is difference between 7150 and 7250-keV peak ratios (no conclusion), summarize half-life analysis, maybe show decay curves, discuss different results between experiments. Show Al-Ga matrix, maybe summarize Ga peaks in a table with corresponding Al energies. Discuss background between the Ga lines, maybe show all projections gated by gammas. Discuss certain Al-Ga transitions (108, 445, 520, maybe 371, 426 keV) and place them into the decay scheme. Discuss other possible candidates, what are the problems there (strange, wide, uncertain Al distributions). Suggest the placement of these "strange" gamma transitions into the decay scheme, consider Al+CE summing and Geant4 simulations (mention/compare it to Andrei's verification of E1 character of 108 keV transition in ^{186}Bi).

Outlook - consider other possibilities to study ^{186}Bi , maybe via ^{190}At decay (and link it to the cross section studies), in ISOLDE (maybe some limitations etc.), other possible means of production (maybe find some other reaction?). Mention some improvements what could be done, more Ge detectors, higher stats, etc.